

MOLECULAR ENGINEERING OF HIGH-PERFORMANCE LITHIUM SULFUR
BATTERIES

A Dissertation

Presented to the Faculty of the Graduate School
of Cornell University

In Partial Fulfillment of the Requirements for the Degree of
Doctor of Philosophy

by

Lin Ma

August 2016

© 2016 Lin Ma

MOLECULAR ENGINEERING OF HIGH-PERFORMANCE LITHIUM SULFUR BATTERIES

Lin Ma, Ph. D.

Cornell University 2016

The rechargeable Lithium-Sulfur (Li-S) battery is an attractive platform for high-energy, low-cost electrochemical energy storage due to the low cost of sulfur (\$0.02/g) and the high theoretical energy density (2500 Wh/kg or 2800 Wh/L) of the sulfur cathode. Practical Li-S cells are limited by several fundamental issues, which derive from the complex solid-state and solution chemistry of the electrodes and electrolyte, such as the low conductivity of sulfur species, the dissolution and transport of long-chain lithium polysulfides (LiPS) into the electrolyte, and instability of the anode during recharge.

This dissertation focuses on three critical aspect of the lithium sulfur battery aimed towards building high-performance lithium sulfur battery. Firstly, to sequester LiPS by creating species in the cathode that bind specifically with LiPS. Three studies were carried out under this topic. The first study was to find out the ideal polysulfide binding functional groups by both theoretical analysis and experimental tools, and amine group was targeted due to its high binding energy with LiPS, stability in the cell and wide availability. The second study then applied this idea in a more efficient and applicable way, by stabilizing LiPS on amine functionalized carbon nanotube. The third study found that the inorganic materials TiS_2 also has high binding energy for LiPS, thus a hybrid cathode of TiS_2 and sulfur was synthesized, where two species work synergistically to give higher capacity.

The second method is to localize the dissolved LiPS by creating an ionic shielding for LiPS. A high-transference number membrane containing sulfonate groups was designed, in which the negatively charges on the membrane reject sulfur species (S_n^{2-}) due to the repulsive electrostatic interactions. Such unique characteristics are attractive in modifying ion transport within the cell and improving the battery performance.

The last part of the dissertation will talk about the protection of lithium metal anode in lithium sulfur battery. We report on the chemistry and interfacial properties of artificial SEI films created by in-situ reaction of a strong Lewis acid AlI_3 , Li metal, and aprotic liquid electrolytes. We find that these SEI films impart exceptional interfacial stability to the Li metal anode.

BIOGRAPHICAL SKETCH

Lin Ma was born in Fujian, China. She went to Beijing for undergrad study in 2008 at Tsinghua University. She majored in polymer materials in the department of chemical engineering. She then joined the PhD program in the department of materials science and engineering at Cornell University and started working in Professor Lynden A. Archer's group in 2012. Her research focuses on materials design and study in energy storage systems, and specifically using the tool of molecular design for high-performance lithium sulfur batteries.

ACKNOWLEDGMENTS

I would like to express my sincere gratitude to Prof. Lynden A. Archer for his insightful guidance and continuous encouragement. His enthusiasm and dedication always keeps me excited about science and my research. I would like to also thank the suggestions and guidance given by my committee members, Prof. Yong L. Joo and Prof. Jin Suntivich. Three of the projects are done in collaboration with Prof. Richard G. Hennig's group, and I would like to thank Prof. Hennig and his student Dr. Houlong L. Zhuang.

I am also very grateful to my parents and sister for their support and care all the time.

Table of Contents

Biographical Sketch	v
Acknowledgements	vi
List of Figures	ix
List of Tables	xiv
CHAPTER 1	1
1.1 Advantages of lithium sulfur battery	1
1.2 Challenges of lithium sulfur battery	2
1.3 Mechanism and electrochemistry in lithium sulfur battery	10
1.4 Outline of the dissertation	22
References	24
CHAPTER 2	28
2.1 Abstract	28
2.2 Introduction	28
2.3 Results and discussion	32
2.4 Experimental section	54
2.4.1 Synthesis of electrode materials	54
2.4.2 Materials characterization	55
2.4.3 Electrochemical characterization	55
2.5 Conclusion	56
Acknowledgements	57
References	58
Appendix	60
CHAPTER 3	66
3.1 Abstract	66
3.2 Introduction	67
3.3 Results and discussion	72
3.4 Materials and method	91
3.4.1 Preparation of CNT-PEI composite	91
3.4.2 Preparation of CPS-59, CPS-70 and CS-60	91
3.4.3 Preparation of Li_2S_4 and Li_2S_9 for FTIR spectra and kinetic study	91
3.4.4 Characterization of the composite	92
3.4.5 Electrochemical characterization	92
3.4.6 Preparation of LiPS electrode for kinetic study	93
3.4.7 Theoretical section	93
3.5 Conclusion	95
Acknowledgements	96
References	97
Appendix	100

CHAPTER 4	107
4.1 Abstract	107
4.2 Introduction	108
4.3 Results and discussion	113
4.4 Experimental section	132
4.4.1 Preparation of TiS ₂ /S blended system	132
4.4.2 Preparation of sulfur infused TiS ₂ foam	133
4.4.3 Characterization of the hybrid cathode	133
4.4.4 Electrochemical characterization	133
4.4.5 Theoretical section	134
4.5 Conclusion	135
Acknowledgement	136
References	137
Appendix	140
CHAPTER 5	148
5.1 Abstract	148
5.2 Introduction	148
5.3 Results and discussion	151
5.4 Materials and method	169
5.4.1 Preparation of the membranes	169
5.4.2 Characterization of the membranes	170
5.4.3 Electrochemical characterization	170
5.5 Conclusion	171
References	172
Appendix	175
CHAPTER 6	188
6.1 Abstract	188
6.2 Introduction	188
6.3 Results and discussion	195
6.4 Materials and method	209
6.4.1 Pre-treatment of lithium metal with AlI ₃	209
6.4.2 Characterization	209
6.4.3 Electrochemical characterization	210
6.5 Conclusion	211
Acknowledgements	211
References	212
Appendix	215

LIST OF FIGURES

- Figure 1.1 Comparison of the theoretical energy density and discharge voltages of different battery storage platforms. 3
- Figure 1.2 Gravimetric energy densities (a) and volumetric energy densities (b) of lithium-sulfur cells with different sulfur loading percentages and their comparison to a $\text{LiC}_6/\text{LiCoO}_2$ cell. 4
- Figure 1.3 Illustration of polysulfides dissolution and shuttling process in a Li-S battery during the recharge process. 7
- Figure 1.4 Discharge and charge profiles for Li-S cells: (a) Cell in which LiPS shuttling is dominant; inset is the drawing that shows the idea of ‘polysulfide shuttling’ (b) Cell in which sulfur is sequestered in carbon nanocapsules in which shuttling is eliminated over a wide range of current densities (0.1 – 3C). 9
- Figure 1.5 (a) Schematic of the critical reactions in a Li-S Cell. (b) A typical discharge and charge voltage profile of the first cycle of Li/S cell. 11
- Figure 1.6 XAS data for a lithium sulfur battery with a gel polymer electrolyte. (a) Waterfall plot of dataset for a full galvanostatic cycle. (b) Spectra selected from specific points during the cycle. (c) Variation of fluorescence signal and cell voltage as a function of charge. Data points correspond to the intensity of the first derivative of each spectrum at 2471.1 eV (pre-peak, black), 2472.6 eV (main peak, red), and 2473.9 eV (Li_2S , green) 17
- Figure 1.7 AFM topography and conductivity images of sulfur composite electrodes that underwent different numbers of cycles as indicated. Top row: Topography images; bottom row: conductivity mapping superimposed on the topography images. 20
- Figure 2.1 Proposed approach for sequestering lithium polysulfides in a sulfur-carbon composite cathode via lithium-nitrile interactions. 34
- Figure 2.2 Density-functional theoretical results for the equilibrated structures and binding energies E_b for a representative long-chain lithium polysulfide (Li-S) with four nitrile-containing molecules: (3-trimethoxysilylpropyl) diethylenetriamine (TMS-PDTA); 1-methy-3-trimethoxysilane imidazolium chloride (IM-Cl); polyacrylonitrile (PAN); polyvinyl pyrrolidone (PVP). 35
- Figure 2.3 DFT calculation of IR on (a) TMS-PDTA and the mixture of TMS-PDTA and Lithium polysulfide; (b) IM-Cl and the mixture of IM-Cl and lithium polysulfide. 38

- Figure 2.4 (a): FTIR spectra of electrodes comprised of pure TMS-PDTA (i) and a mixture of polysulfides and TMS-PDTA (ii); (b): pure IM-Cl (i) and mixture of polysulfides and IM-Cl (ii). 39
- Figure 2.5 ICP-AES characterization of time-dependent Li_2S_4 dissolution in tetraglyme. (a) Raw data for elemental Li: (i) $t = 60\text{mins}$; (ii) $t = 10\text{mins}$; (iii) = blank (baseline). (b) Raw data for elemental sulfur: (i) $t = 60\text{mins}$; (ii) $t = 10\text{mins}$; (iii)=blank (baseline). (c) Sulfur content in tetraglyme for three different cases (squares represent the case of no sorbent; circles with TMS-PDTA; triangles with IM-Cl). 41
- Figure 2.6 Galvanostatic voltage profile for Li-S cells: (a) without the molecular sorbent in the cathode; (b) with TMS-PDTA (c) IM-Cl. 43
- Figure 2.7 Voltage vs. capacity profiles for Li-S cells with: (a) 6w% TMS-PDTA and (b) 6w% IM-Cl sorbents in the cathode. 44
- Figure 2.8 Long-term cycling performance of Li-S batteries without additives (black triangle), with TMS-PDTA (black square) and the corresponding Coulombic efficiency represented as black cycle, with IM-Cl (red square) and the corresponding Coulombic efficiency represented as red cycle at 0.2C 46
- Figure 2.9 Comparison of Li-S battery performance with different weight fractions of PMS-PDTA in the cathode: without additives (black triangle), with 6w% TMS-PDTA (red square), with 2w% IM-Cl (a) Cells cycled at 0.2 C; (b) Cycled at 1C. 49
- Figure 2.10 SEM images of the L-S battery cathode before and after galvanostatic cycling at a fixed rate of 335 mA/g (0.2C). (a) Cathode with 6w% TMS-PDTA before charge/discharge; (b) Same as (a) except without sorbent; (c) Same as (a), but after 100 charge-discharge cycles; (d) Same as (b) but after 100 cycles. 52
- Figure 2.11 TEM images of the L-S battery cathode after galvanostatic cycling at a fixed rate of 335 mA/g (0.2C). (a) Cathode with 6w% TMS-PDTA after 100 charge-discharge cycles; (d) Same as (a) except with 6w% IM-Cl; (b and c) EDX carbon and sulfur maps based on the area shown in (a); (e and f) EDX carbon and sulfur maps based on the area shown in (d). 53
- Figure 3.1 Procedure of preparation of CNT-PEIS composite. 71
- Figure 3.2 XPS survey scanning spectra for: (a) unmodified CNTs; and (b) PEI modified CNTs. (c) High-resolution N 1s spectrum of PEI modified CNTs. (d) Comparison of the C 1s signal of CNTs before and after attachment of PEI. (e) High-resolution C 1s XPS spectrum

of unmodified CNTs. (f) High-resolution C 1s XPS spectrum of PEI modified CNTs. (f) High-resolution C 1s XPS spectrum of PEI modified CNTs.	74
Figure 3.3 (a) Structure of PEI deduced from DFT analysis of the binding energy between PEI and the Li-S ⁻ species. (b) DFT calculation of IR spectra of the mixture of Li-S ⁻ species and PEI (red) and pure PEI (black). (c) Experimental FTIR spectra of pure PEI. (d) Experimental FTIR spectra of mixture of Li ₂ S ₉ and PEI.	75
Figure 3.4 High resolution XPS spectra for: (a) Li 1s of discharge product of CNT-PEIS composite; (b) N 1s before and after discharge; (c) S 2p before and after discharge; (d) N 1s of CNT-PEI composite before sulfur loading; and(e) N 1s of sulfur loaded CNT-PEI composite.	78
Figure 3.5 Raman spectra of CNT, CNT-PEI and sulfur loaded CNT-PEI composite.	79
Figure 3.6 XRD analysis of CNT-PEI and CNT-PEI/S composite at different sulfur loadings.	83
Figure 3.7 (a) Galvanostatic voltage profile for Li-S cell with CPS-70 as cathode at scanning rate of 0.1mV/s. (b) Voltage vs capacity profile at different cycles for Li-S cell with CPS-70 as cathode cycled at 0.5C (838 mA/g) (c) Long-term cycling performance of Li-S cells with CPS-70, CPS-59 and CNTS-60 as cathodes respectively cycled at 0.5C (838 mA/g) (d) Deep cycling of CPS-70 at 0.5C (838mA/g) (e) Long-term cycling performance of Li-S cells with CPS-70 cycled at 0.5C (838mA/g), 1C(1675mA/g) and 2C (3350 mA/g) respectively, with filled circles representing capacity and blank circles representing Coulombic efficiency. (f) Voltage vs capacity profile for Li-S cell with CPS-70 as cathode cycled at at 0.5C (838mA/g), 1C(1675mA/g) and 2C (3350 mA/g) respectively. (g) Rate capabilities of CPS-70 at various current densities.	87
Figure 3.8 SEM images for: (a) Pristine CNT; (b) CNT-PEI hybrid; (c) CPS-59; (d)CPS-70; (e) Li-S cell cathode applying CNT/S-60 after discharge; (f) Li-S cell cathode applying CPS-59 after discharge; (g) Li-S cell cathode applying CPS-70 after discharge.	89
Figure 4.1 (a) One-step method to prepare sulfur infused TiS ₂ foam. (b) Diagram of the cross section of the foam during discharge.	112
Figure 4.2 Voltage profile of electrodes containing TiS ₂ , Sulfur, and TiS ₂ -sulfur mixture.	116
Figure 4.3 (a) Top and (b) side views of Li ₂ S adsorption on TiS ₂ .	118
Figure 4.4 Sulfur content in tetraglyme for two different cases (black represents the case of carbon matrix without TiS ₂); red with TiS ₂ .	120

Figure 4.5 (a) Comparison of Impedance spectra of Sulfur, TiS_2 and TiS_2/S blended system. Impedance before (black) and after (red) cycling of (b) sulfur electrode, (c) TiS_2 electrode. (d) TiS_2/S_8 hybrid cathode.	122
Figure 4.6 SEM images of sulfur electrode before cycling (a), after cycling (b); TiS_2/S_8 hybrid cathode before cycling, (c); after cycling, (d).	123
Figure 4.7 Thermogravimetric analysis of 1. Pure Ti metal; 2. Pure TiS_2 powder; 3. TSF-5; 4. TSF-10; 5. TSF-15 burned in air.	127
Figure 4.8 XRD analysis of 1. Pure TiS_2 powder. 2. TSF5. 3. TSF10. 4. TSF15.	128
Figure 4.9 (a) Voltage profiles (b) Cycling performance of TSF5, TSF10, and TSF15 cycled at $2\text{mA}/\text{cm}^2$. (c) Comparison of voltage profile of TSF15 at $2\text{mA}/\text{cm}^2$, $5\text{mA}/\text{cm}^2$ and $10\text{mA}/\text{cm}^2$ respectively. (d) Cycling performance of TSF15 cycled at $10\text{mA}/\text{cm}^2$. (e) Comparison of sulfur loading, the specific capacity, the areal capacity in this work with those in the references at the 20 th cycle.	131
Figure 5.1 Different membrane systems interact with ions in the electrolyte.	153
Figure 5.2 Preparation process of sulfonate group containing membrane.	156
Figure 5.3 Morphology of the membranes. (a) photographic image of the pure PEGDMA membrane; (b) photographic image of the sulfonate group containing membrane; (c) SEM image of the pure PEGDMA membrane; (d) SEM image of the the sulfonate group containing membrane.	157
Figure 5.4 Confirmation of the incorporation of sulfonate group by FTIR and EDX.	159
Figure 5.5 Conductivity of the membranes with different contents of sulfonate group.	162
Figure 5.6 Visualization of the LiPS diffusion through different membrane systems.	165
Figure 5.7 Electrochemical characterization and cycling performance: (a) and (b) show impedance and current change before and after polarization for transference number measurement for (a) Celgard (b) PV6 membranes respectively; (c) and (d) show cycling performance of the Li-S cells with the prepared membranes cycled at 0.5C with additive-free electrolyte.	167
Figure 6.1 Proposed formation mechanism for a multi-functional artificial solid electrolyte interfaces (SEI) at a Li anode produced by AlI_3 .	194
Figure 6.2 Chemical stability of AlI_3 -DOL-treated lithium metal in a LiPS-rich electrolyte. a, Optical images recorded at a 3-hour interval of a LiPS-rich liquid electrolyte exposed to Li	

metal without (upper row) and with (lower row) pretreatment by AlI_3 -DOL. b, Uv-vis spectra of a LiPS-rich electrolyte after exposure to lithium metal for 12 hours. c, XRD of the pristine lithium metal (red) and AlI_3 -DOL-treated lithium metal foil (black) after immersion in a LiPS-rich electrolyte for 12 hours. d, Nyquist plot for a lithium symmetric cell containing a LiPS rich electrolyte recorded in 8 hour increments. 199

Figure 6.3 Lithium dendrite resistance and Coulombic efficiency of AlI_3 -DOL-treated lithium metal. a, Short circuit time for symmetric Li/Li cells deduced from galvanostatic polarization measurements at different current densities. The dark grey column represents the control case in which pristine lithium is used; the light grey column shows the short circuit time for cells based on AlI_3 -DOL-treated lithium metal. b and c, Lithium deposition efficiency in Li/electrolyte/stainless steel cells comprised of pristine lithium and AlI_3 -DOL-treated lithium metal electrodes, respectively. In these experiments, the cell is discharged for 30 min at a constant current density then recharged to 0.5V at the same current density. b, Current density = 0.2 mA/cm². c, Current density = 2 mA/cm². 201

Figure 6.4 Characterization of the AlI_3 -DOL-treated lithium metal by XPS and NMR. a, b and c, High resolution XPS spectra for AlI_3 -DOL-treated lithium metal. a, I 3d spectra; b, Li 1s spectra; c, Al 2s spectra. d and e, NMR of the polymeric gel. d, ¹³C NMR spectrum. e, ¹H NMR spectrum. 205

Figure 6.5 Electrochemical measurements employing Li-S cells containing AlI_3 -DOL-treated lithium metal as anode and at a current rate of 0.5C. These cells do not contain LiNO_3 electrolyte additives typically used in Li-S battery studies. a, Comparison of cycling performance of Li-S cells based on AlI_3 -DOL-treated and untreated Li metal anodes. The black filled symbols denote the specific capacity of cells based on pristine lithium metal anodes with additive free electrolyte; the green filled symbols are specific capacities of cells based on AlI_3 -DOL-treated Li anodes with additive-free electrolyte; the red filled symbols denote specific capacities of cells based on AlI_3 -DOL-treated Li anodes and DOL/DME-based electrolytes containing AlI_3 as additive. The open symbols are the respective Coulombic efficiency. b, The corresponding voltage profiles for Li-S cells in each of the configurations reported in Figure 6.5a. 208

LIST OF TABLES

Table 1.1 Summarization of the most commonly used methods in the Li-S battery.	13
Table 2.1 The percentage of discharge capacity retained of each cathode with or without additives after 100 cycles in comparison to the tenth cycle capacity.	47
Table 3.1 I_D/I_G ratio in different composites.	80
Table 3.2 Rate constant for dissolution k , percentage of loss of sulfur into the electrolyte, and equilibrium concentration c_s in each case.	94
Table 4.1 $S_8/TiS_2/Ti$ content in TSF5, TSF10, and TSF15. Percentage of sulfur, TiS_2 and Ti metal, the mass ratio of Ti:S, the molar ratio of Ti:S is calculated from TGA. The last column shows the mass ratio of Ti:S originally added to quartz tube.	126

CHAPTER 1

INTRODUCTION

Partly adapted with permission from
L. Ma, K. E. Hendrickson, S. Wei, L. A. Archer, Nanomaterials: Science and applications in the
lithium-sulfur battery. Nano Today, 2015, 10, 315-338.

1.1 Advantages of lithium sulfur battery

Among solid-state cathode materials under consideration for rechargeable lithium batteries, elemental sulfur offers the greatest promise for reversibly storing large amounts of electrical energy at moderate cost. As a cathode, sulfur hosts as many as two lithium ions non-topotactically via the following redox reaction: $16\text{Li} + \text{S}_8 \rightarrow 8\text{Li}_2\text{S}$. This reaction is attractive for electrochemical storage for a number of reasons. It can be used to reversibly store large amounts of electrical energy – up to 2500Wh/kg or 2800Wh/L of sulfur – a factor of ten or more higher than other electrochemical storage technologies (e.g. Ni-H (80Wh/kg, 120Wh/L), Li-ion (150Wh/kg, 250Wh/L), and Li-ion polymer batteries (180Wh/kg, 300Wh/L)) of contemporary interest (**Figure 1.1**).¹⁻⁵ The reaction also occurs spontaneously, is fully reversible, and does not require intervention using catalysts or other means. Finally, the reaction can in principle occur entirely in the solid state and generates lithium-sulfur compounds as its only products. This can be contrasted with competing energy storage solutions based on combustion of fossil fuels, which irreversibly generate even larger amounts of energy on a gravimetric or volumetric basis (e.g. commercial coal: 6.7kW·h/kg, and a commercial-grade gasoline: 12kW·h/kg, 9kW·h/L), but with the added burden of managing harmful CO₂ and other gaseous emissions. The low cost of sulfur (\$0.02 per g) and its availability in regions all over the world provides an additional

incentive for development of Lithium-Sulfur (Li-S) electrochemical storage technology^{6,7}.

1.2 Challenges of lithium sulfur battery

Despite the considerable advantages offered by Li-S storage technology, commercial development of a practical Li-S rechargeable battery has been limited by multiple transport and thermodynamics-related challenges. In spite of the significant advances made over the last decade in improving Li-S battery performance, the actual storage delivered by even the best Li-S cells reported in the literature is still quite far away from the theoretical capacity upon which much of the promise of the Li-S battery lies. The best performing Li-S cells rarely deliver storage capacities above 60% of the theoretical value for this chemistry. This situation can be contrasted with the state of affairs in more traditional lithium ion batteries, where cell-level performance approaching 90% of theoretical capacities are common. A Li-S battery that delivers 50% of its theoretical capacity over hundreds of cycles of charge and discharge already offers superior energy storage to the most energy-dense LIBs on a gravimetric storage basis, but substantially better performance is needed from Li-S cells to compete with LIBs for storage on a volumetric basis. The study carried out by Jie⁹ (**Figure 1.2**) nicely illustrates this point. The study also underscores the need for Li-S cell designs in which high sulfur loadings in the cathode is achieved. Specifically, at low sulfur loadings, the volumetric energy density for the Li-S battery is noticeably lower than that of commercial lithium ion cells, even if one could realize the theoretical capacity of sulfur. Rechargeable Li-S cells that approach the theoretical capacity of the electrodes at high sulfur loadings are obviously desired.

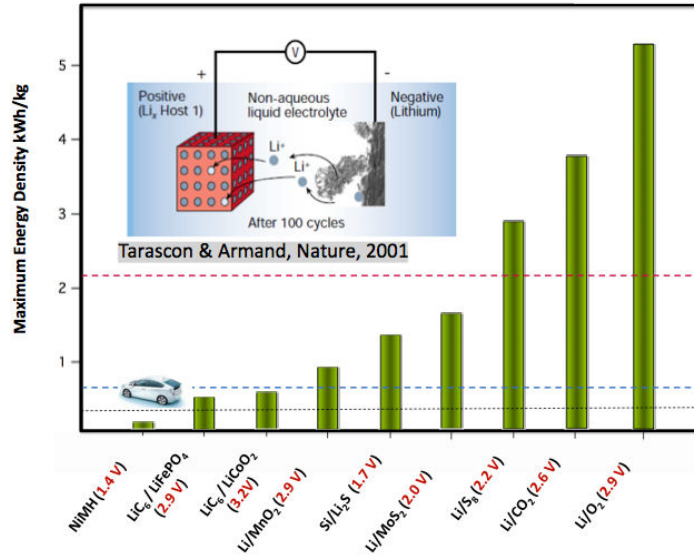
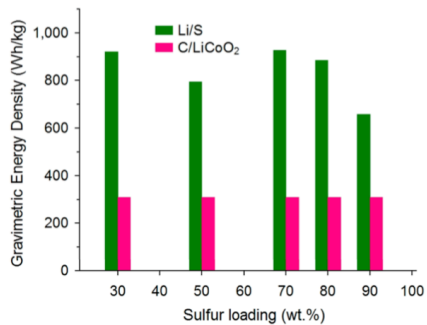
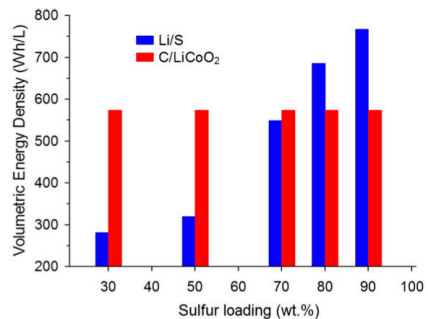


Figure 1.1 Comparison of the theoretical energy density and discharge voltages of different battery storage platforms.

(The inset illustrates the challenge with lithium dendrite growth and proliferation that limits adoption of storage technologies to the right of the plot that use metallic lithium as anodes for high overall cell energy densities. The red horizontal line represents the useful energy density of gasoline for transportation (i.e. the energy density of gasoline taking into account the 18% efficiency of the internal combustion engine). The dashed blue and black lines correspond to the US Advanced battery Consortium (USABC) long-term (2020) and short-term energy density targets, respectively⁸.)



(a)



(b)

Figure 1.2 Gravimetric energy densities (a) and volumetric energy densities (b) of lithium-sulfur cells with different sulfur loading percentages and their comparison to a LiC₆/LiCoO₂ cell. Reprinted with permission from ⁹. Copyrights 2014 American Chemical Society.

In-depth understanding of the working mechanism, transport and other barriers that limit performance of Li-S cells are needed for further progress in the field. Such understanding is also essential to guide emerging efforts aimed at rationally designing each of the components in the Li-S cell towards the goal of full materials utilization. Sulfur is infamous for its poor electrical conductivity (5×10^{-30} S/cm at 25°C) and ease with which it is able to form solid allotropes (over 30 are known)¹⁰. The first of these traits means that a pure sulfur cathode is intrinsically insulating in nature, which limits the utilization of the active electrode material. High-surface area carbons are typically used as conductive additives within the cathode, but better charge transport in the cell often comes at the expense of storage capacity. Additionally, the volume of sulfur increases by around 80 % (density changes from 2.03 g/cm³ for sulfur to 1.66 g/cm³ for Li₂S) when it is fully lithiated. This means that synergistic cathode designs that can accommodate the volume change without compromising electronic connections with conductive additives, which do not expand, are critical for stable, long-term cell performance. A consequence of the second trait is that the preferred redox reaction product, Li₂S, is almost always accompanied by formation of various intermediate lithium polysulfides (LiPS = Li₂S_n, 2 ≤ n ≤ 8) products (see **Figure 1.3**). Depending on the value of *n*, these intermediates can be either insoluble or soluble in the electrolyte, which leads to multiple challenges in managing active materials utilization and reuse. For example, the fully reduced product, Li₂S is insoluble in most electrolytes and is both electronically and ionically insulating. Thus, once Li₂S begins to form in the sulfur cathode, it can only grow by spreading outwards to cover the exposed surface of the conductive carbon particles in the electrode. Ultimately, this growth produces an insulating film on the carbon, which prevents further electronic and ionic access to the active material in the cathode, and the cell discharge voltage drops rapidly (**Figure 1.4**). Especially troublesome, are

the soluble (Li_2S_n , $2 < n < 8$) polysulfide discharge products, which establish an internal shuttling pathway between the lithium anode and sulfur cathode that, if unchecked, will continuously consume the active material in both electrodes. Specifically, during the first discharge, the higher order LiPS ($n > 2$) dissolve into the electrolyte, depleting sulfur from the cathode. Once in the electrolyte, polysulfides diffuse freely and ultimately reach the metallic lithium anode where they undergo chemical reaction to form lower order polysulfides, including $\text{Li}_2\text{S}_{n-1}$ and Li_2S , which may either deposit on the Li anode or diffuse back to the sulfur cathode, where they react with sulfur to reform higher-order polysulfides.

The parasitic loop or ‘shuttle’ illustrated in **Figure 1.3** is free to take place repeatedly and continuously during the cell recharge and not only depletes the active electrode materials, but continuously consumes electrical energy from an external circuit. It is easily visualized by the telltale asymmetry in the discharge and charge profiles (**Figure 1.4a**) of a Li-S cell and, lowers the Coulombic efficiency of the cell. Shuttling can also occur during cell storage and leads to self-discharge, which limits the shelf life of Li-S batteries. Sequestering the sulfur in carbon nanocapsules¹²⁻¹⁴ is one of a handful of nanomaterials approaches that have been shown to completely remove this asymmetry (**Figure 1.4a**), underscoring its fundamental connection to LiPS dissolution. As illustrated in **Figure 1.4b**, without any other intervention strategies, this method completely eliminates the shuttle during the first cycle of charge and discharge for a range of Li-S cell discharge/charge current densities.

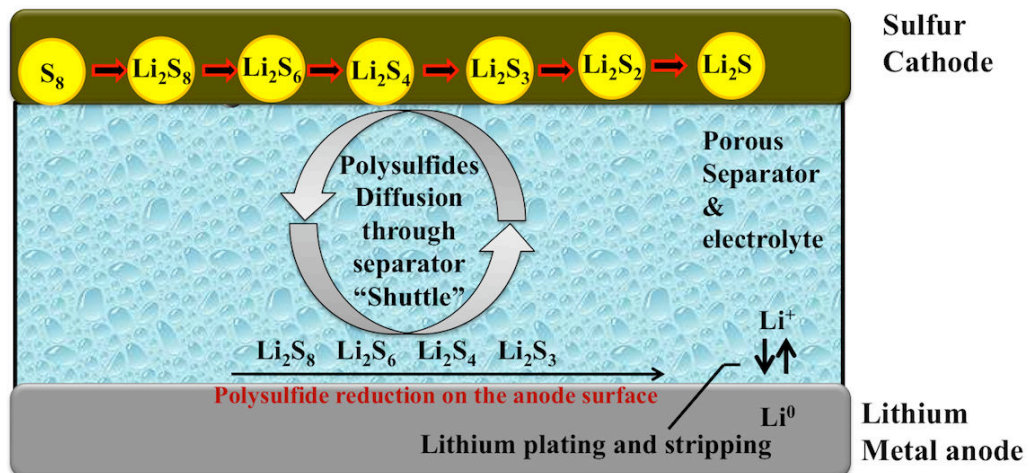
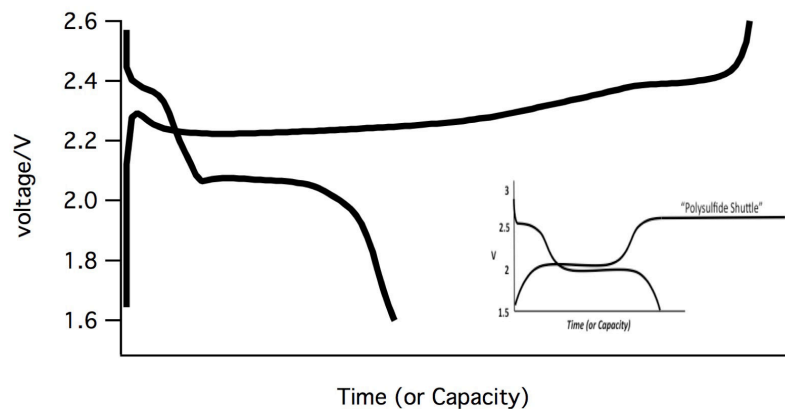
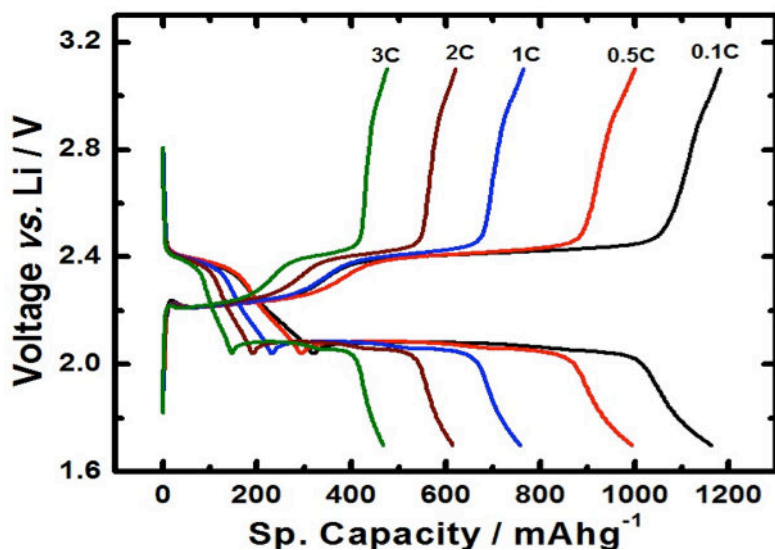


Figure 1.3 Illustration of polysulfides dissolution and shuttling process in a Li-S battery during the recharge process. Reprinted with permission from ¹¹. Copyrights 2004 Elsevier.

In addition to the intrinsically high storage capacity of sulfur, the high overall energy storage capacity of the Li-S cell stems from the use of metallic lithium as the anode. Li is readily ionized in a variety of aprotic liquids and as such provides an efficient complement to sulfur in an electrochemical cell designed to store large amounts of electrical energy. Unfortunately, even at low current densities, Li electrodeposition is sensitive to defects at the electrode surface and is prone to various transport and morphological instabilities^{15,16} that lead to growth and proliferation of rough electrodeposits collectively termed dendrites. Nucleated at the anode, these dendrites may grow as mossy deposits that react with the electrolyte and, if unchecked, will ultimately consume it all, drying out the cell. Dendrites may also grow and proliferate in the inter electrode space, ultimately short-circuiting the cell with potentially catastrophic consequences for safety. A remarkable, though poorly studied feature of the Li-S cell is that it possesses multiple internal safety measures that prevent catastrophic failure by dendrite-induced short circuits. LiPS dissolution and shuttling in the electrolyte provides an intrinsic mechanism for passivating dendrite tips by reaction with LiPS species in the electrolyte. Specifically, the tips concentrate electric field lines and the LiPS flux in the electrolyte, which leads to the reduction of LiPS and deposition of insoluble, insulating Li_2S on the tip surface limiting/eliminating further deposition of Li. This process also provides a high intrinsic overcharge tolerance for Li-S cells.



(a)



(b)

Figure 1.4 Discharge and Charge Profiles for Li-S cells: (a). Cell in which LiPS shuttling is dominant; inset is the drawing that shows the idea of ‘polysulfide shuttling’ (b). Cell in which sulfur is sequestered in carbon nanocapsules in which shuttling is eliminated over a wide range of current densities (0.1 – 3C). Reprinted with permission from ¹³. Copyrights 2011 Wiley-VCH Verlag GmbH & Co. KGaA, Weinheim.

1.3 Mechanism and electrochemistry in lithium sulfur battery

The complex coupling of electrochemistry, thermodynamics, and transport phenomena, and its immense potential to transform energy-storage in many fields, makes the Li-S battery very fertile ground for scientific research that bridges many fields. Unfortunately, Li-S cells have for the most part been studied as ‘black boxes’ with few published works focused on understanding the principles that define the limits of performance and operation. Based on the apparent clarity of the issues raised in the introduction, it is perhaps tempting to conclude that this neglect is justified, as the key mechanisms are already well understood. Reality is unfortunately inconsistent with this view and there remain multiple controversial perspectives. **Figure 1.5**¹⁷ summarize the four critical types of reactions currently thought to occur in the sulfur cathode. They are fragmentation reactions (I); electrochemical reduction reactions of elemental sulfur and lithium polysulfides (II); association or dissociation reactions of polysulfides (III); and chemical reactions of lithium polysulfides with nonaqueous electrolyte (IV). On the anode side of the cell, complex reactions also occur with lithium metal, including the reaction of lithium metal with electrolyte (V) and the reaction of lithium metal with lithium polysulfides (VI).

Correspondingly, **Figure 1.5b** shows a typical discharge and charge voltage profile for the first cycle of a Li-S battery¹⁸. Based on the phase change of sulfur species, the discharge process is typically divided into four reduction regions: Region I: A solid-liquid two-phase reduction from elemental sulfur to Li_2S_8 , which produces the upper voltage plateau during discharge at 2.2-2.3 V. Region II: A liquid-liquid single-phase reduction from the dissolved Li_2S_8 to low-order LiPS, during which the discharge voltage steeply declines and the solution’s viscosity gradually increases. Region III: A liquid-solid two-phase sequential reduction from the dissolved low-order

LiPS to insoluble Li_2S_2 or Li_2S , which is responsible for more than 60% of the theoretical capacity of the cell. Region IV: A solid-solid reduction from insoluble Li_2S_2 to Li_2S .

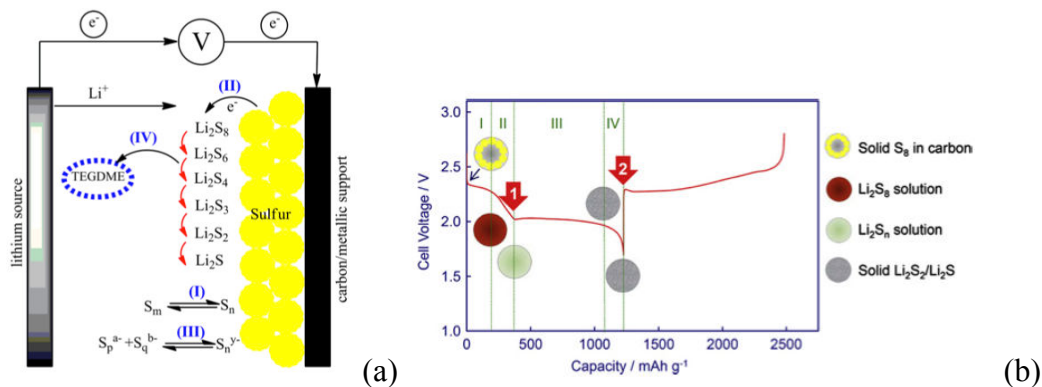


Figure 1.5 (a) Schematic of the Critical Reactions in a Li-S Cell. Reprinted with permission from ¹⁷. Copyrights 2014 American Chemical Society (b) A typical discharge and charge voltage profile of the first cycle of Li/S cell. Reprinted with permission from ¹⁸. Copyrights 2012 Elsevier.

Intrusive experimentation using the modern analytical tool set in principle provides a complementary approach for elucidating the fundamental processes at work in the Li-S cell. **Table 1.1** summarizes the most commonly used methods for interrogating reaction pathways in the Li-S battery. This list is considerably shorter than typically found in other areas of materials science because interrogation of the Li-S cell is, unfortunately, limited by several factors: (i) Some of the key intermediates in the charge /discharge states identified by theory are unstable and may associate or disassociate to form other, more stable species; (ii) The charge/discharge intermediates and products are all sensitive to the air and moisture, and can change under high vacuum. This provides very strong limitations on which tools can be used to quantify the amounts and to define the potentials at which each of the multitude of intermediate species proliferate; (iii) the intermediates appear to always co-exist, which means that it is never really practical to separate individual species for in-depth studies; (iv) lithium is a light, very active element and the ability to detect it in ionic form is limited.

X-ray diffraction (XRD) has proven to be a powerful technique to follow the lithium insertion mechanism in Li-ion batteries. In the Li-S system, as the redox reaction is accompanied by phase transformation (solid–liquid phases) of active material, structural and morphological changes occur at the positive electrode. Abruna and co-workers²⁹ employed a combination of in-situ X-ray diffraction (XRD) and K-edge X-ray absorption near edge structure (XANES) to perform inoperando investigations of Li-S cells with PVDF/tetraglyme-LiClO₄ gel-polymer electrolytes.

Table 1.1 Summarization of the most commonly used methods in the Li-S battery.

Techniques	Property characterized	Representative study (reference number)
Transmission electron microscopy (TEM)	Size, shape and crystallinity	19,20
Scanning electron microscopy (SEM)	Shape/assembly structure	21-23
X-ray diffraction (XRD)	Crystal structure	24-29
UV-vis Spectroscopy	Light absorption and scattering/Species identification	30-33
X-ray photoelectron spectroscopy (XPS)	Chemical composition/binding information	34-37
Energy dispersive X-ray analysis (EDX)	Chemical composition	38,39
Atomic force microscopy (AFM)	Shape, size, and work function	19,40
Near-edge X-ray absorption fine structure (NEXAFS/XANES)	Chemical composition/oxidation state	29,37,41-43
X-ray emission Spectroscopy (XES)	Electron band gap	37
Chemisorption and physisorption	Surface area/hole size	44-47

These studies confirm that crystalline S_8 transitions to non-crystalline LiPS in region I and that by the end of region IV, fully reduced crystalline Li_2S is observed. Both sets of observations are consistent with results reported in other in-situ x-ray studies²⁴⁻²⁶. However, there is disagreement about at what stage in the cell discharge Li_2S is observed. Specifically, in situ synchrotron-based results clearly indicate formation of crystalline Li_2S on the positive electrode at the very beginning of Region III, whereas the study by Abruna et al suggest that Li_2S is formed near the end of region III. This is an important difference because it has consequences for the reaction mechanism. A remarkable pair of results from all in-situ XRD studies is that Li_2S disappears completely from the cathode during cell recharge and that sulfur initially present in the orthorhombic state, first disappears during discharge and reappears during charge in the form of another allotrope: monoclinic b-sulfur.

A much larger number of ex-situ XRD studies of the Li-S battery cathode have been reported^{19,21-23,27,28,48,49}. While most of these works confirm the results reported from the in-situ work, namely that crystalline S_8 present in the electrode at the beginning of discharge gradually gives way to cubic crystalline Li_2S by the end of discharge^{22,27,48}, as with the in-situ studies there is discrepancy about where in the discharge process the Li_2S is first observed^{23,28}. There are also discrepancies about whether the Li_2S formed on the cathode can be completely removed by recharge. The in-situ XRD studies by Abruna and coworkers²⁹ show that Li_2S is completely removed upon cell recharge, but the authors only reported results for a single cycle of charge and discharge. These findings disagree with other reports²¹ where traces of Li_2S can still be observed in the cathode of Li-S cells subject to more cycles of discharge and charge. Considering the notoriously poor electronic and ionic conductivity of Li_2S , it is likely that the material gradually builds up in the cathode over prolonged cycling^{21,50}. Divided opinions also exist about sulfur

disappearance and reappearance in the cathode during Li-S battery cycling exists as well. In general, researchers agree that x-ray diffraction associated with crystallized sulfur disappears during initial discharge of a Li-S battery, even when care is taken to interrupt the cell at different depths of discharge^{23,27,28}. However, some studies reported the accumulation sulfur in the cathode during prolonged cycling¹⁹, particularly at high C-rates²². Sulfur formation at the end of charge has also been reported in some cases^{28,49} whereas in others soluble polysulfides formed during the initial discharge are argued to remain in solution throughout cell operation and to not transform back to solid S₈^{11,21,23,27}. These studies underscore the richness of the electrode processes and highlight the need for more in-depth work using other techniques.

The XANES study by Abruna and co-workers (**Figure 1.6**) is unique among in-situ studies of Li-S cells because it provides information about both the crystalline and amorphous species. One key finding from this work is that the clear demarcation of the four reaction regimes depicted in **Figure 1.5b** and the equally popular cartoons (**Figure 1.3**) that summarize understanding of the reactions that occur in each of these regimes may be gross over simplifications. In particular, the authors reported non-negligible concentrations of a multitude of high order LiPS species in region II and show evidence that these species undergo a complex set of disproportionation reactions to form the primary electroactive species LiS₃ responsible for the plateau in Region III (shown in **Figure 1.5b**). The appearance of fully crystalline Li₂S at the end of discharge is argued to occur by disproportionation of the reduction product, Li₂S₃, at the end of region III, rather than by the sequential electrochemical reduction process typically assumed. An important consequence of this study is that even at > 90% conversion of LiPS produced by the end of Region I, the overall cell capacity is at most 64% of the theoretical capacity. Thus, the presence of sulfur as electrochemically-inactive polysulfides can reasonably account for a significant

fraction of the discrepancy between the theoretical and actual storage capacity reported for Li-S cells. Another XANES study is carried out by Nazar group⁴¹ to show how sulfur fraction and sulfide precipitation impact capacity. In this study, the authors attribute the limited capacity to the disproportionation reaction of $S_8^{2-} \rightarrow S_6^{2-} + S_8$. The different results might come from the different cathodes and electrolyte they used: in Abruna's work, sulfur is physically mixed with carbon and the electrolyte is composed of $LiClO_4$ in Tetraglyme, while a sulfur impregnated in porous hollow carbon spheres cathode and $LiTFSI/LiNO_3$ in DOL/DME electrolyte is applied in Nazar's study.

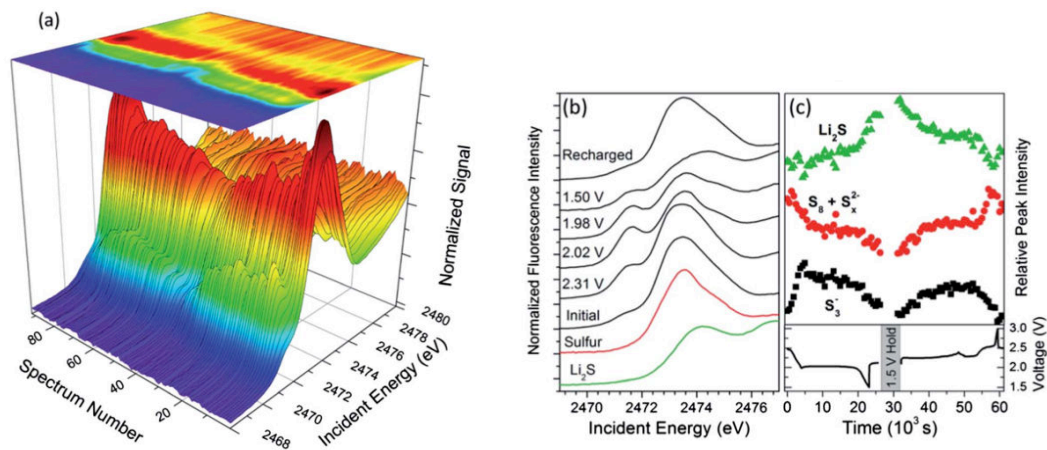


Figure 1.6 XAS data for a lithium sulfur battery with a gel polymer electrolyte. (a) Waterfall plot of dataset for a full galvanostatic cycle. (b) Spectra selected from specific points during the cycle. (c) Variation of fluorescence signal and cell voltage as a function of charge. Data points correspond to the intensity of the first derivative of each spectrum at 2471.1 eV (pre-peak, black), 2472.6 eV (main peak, red), and 2473.9 eV (Li₂S, green) Reprinted with permission from²⁹. Copyrights 2014 The Royal Society of Chemistry.

Identification of sulfide species formed during the charge/discharge process is critical in understanding the mechanism. U-vis spectroscopy is another powerful characterization tool and provides insight not only into the overall chemical composition of LiPS in electrolytes, but also potentially about the time-dependent concentration of each LiPS component. Barchasz et al ³², for example, used this method to investigate the electrolyte composition at different discharge potentials in a TEGDME-based electrolyte. They showed that besides the more familiar electrochemical reductions, there are complicated chemical reactions between PS anions in the electrolyte solution: $\text{Li}_2\text{S}_n + \text{Li}_2\text{S} \rightarrow \text{Li}_2\text{S}_{n-m} + \text{Li}_2\text{S}_{1+m}$; $\text{Li}_2\text{S}_n \rightarrow \text{Li}_2\text{S}_{n-1} + 1/8\text{S}_8$. Also, the deposition of insulating Li_2S results in electrode passivation and an early ending of discharge resulting in an incomplete end product Li_2S_2 . controlling the deposition of Li_2S might then be a critical point for achieving the full capacity of Li-S cell. Patel et al ³⁰ carried out what appears to be the first UV-vis spectroscopy study of a Li-S battery in operando. The authors showed that it is possible to establish qualitative and quantitative differences between soluble polysulfides in the catholyte. They also show that there are characteristic absorption wavelengths for each type of polysulfides and confirmed that the UV spectra of a range of catholyte solutions were correlated to the natural logarithm of concentration in agreement with the Beer-Lambert law. These experiments suggest that dissolved polysulfides are in equilibrium and there is a much larger content of certain mid-length polysulfide species present in the electrolyte at the end of charging process. Interestingly, those two points are precisely those reported in the XANES study discussed earlier. A year later, the same group extended the UV-vis study to investigate two electrolyte systems and to relate their observations to macroscale features of Li-S battery performance ³¹. It was found that the capacity of Li-S cells fade more quickly in sulfolane-based electrolytes than in TEGDME:DOL and that the higher solubility of Li-PS in the sulfolane-based

electrolyte leads to higher irreversible loss of active material. Most interesting, from a battery performance perspective, among these observations is that a maximum concentration of about 30mM of polysulfides is achieved in the electrolyte at the beginning of the low-voltage plateau (the beginning of Region III in Scheme 2(b)), which provides the first direct correlation between the appearance of the dip in the discharge curve and a viscosity spike in the electrolyte ¹⁸.

In addition to providing insights into the electrochemistry in Li-S battery electrolytes, these tools have also been used to correlate changes in morphology at the Li-S cell electrodes to performance. Aurbach et al. reported morphological and structural studies of composite sulfur electrodes by AFM ¹⁹. They found that the ratio of the conductive surface area to the total scanned surface area of a pristine electrode is close to 90%, but less than 30% of the surface is still conductive after 6 cycles of discharge and charge (**Figure 1.7**). This finding agrees with the findings from x-situ XRD studies that the electrode is covered by an insulating layer, which could be a critical factor that results in the capacity fading. These findings are largely in line with a much larger body of work based on ex-situ SEM ²¹⁻²³, TEM ^{19,20}, Raman ^{19,20,51} and in-situ electrochemical impedance spectroscopy ⁴⁰, which all show that if no special effort is made to sequester sulfur in the cathode, most of the sulfur in the cathode disappears at the end of region II of the discharge. Visualization studies using flow cells show that the disappearance is linked to dissolution of LiPS in the electrolyte. These studies also confirm that the electrode is covered by a film at the end of discharge due to the precipitation Li_2S , which increases the interfacial resistance of the cathode.

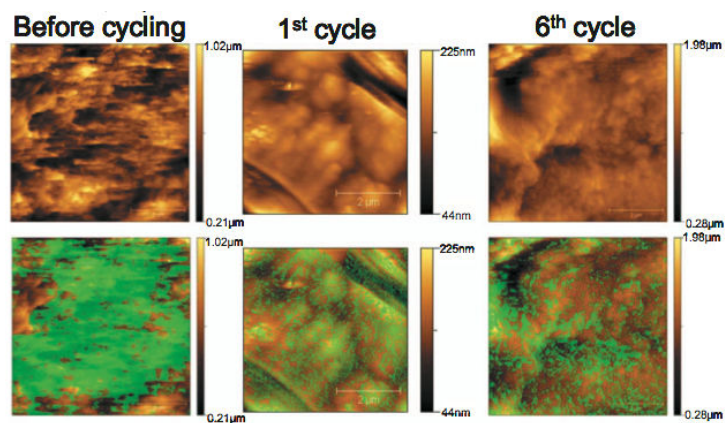


Figure 1.7 AFM topography and conductivity images of sulfur composite electrodes that underwent different numbers of cycles as indicated. Top row: Topography images; bottom row: Conductivity mapping superimposed on the topography images. Reprinted with permission from ¹⁹. Copyrights 2010 The Electrochemical Society.

With the growing trend of incorporating nanomaterials into the sulfur cathode for improving cell performance, other nano-characterization tools have received commensurate attention for understanding the mechanisms through which these materials function. For example, porous nanocarbons have been used as the host of sulfur because of lots of advantages, thus chemisorption and physisorption is used to characterize the surface area and pore size of the carbon host, which are important parameter of the system⁴⁴⁻⁴⁷. Also, in the carbon/sulfur composite, the distribution of the sulfur in the carbon matrix is important in determining the performance, and EDX is a powerful tool to map the individual elementary distribution^{38,39}. In addition, additives with multiple function are used, for the reason that they can interact with polysulfide to contain the capacity. In those work, XPS is widely used as a tool to probe the interaction between sulfur species and the function group/atom of the additives³⁴⁻³⁶.

Computer stimulations provide complementary insights into the electrochemical reactions in Li-S cells. Chen⁵² reported DFT simulations of Li_2S_n ($n=1\sim 8$) clusters in the discharge reaction and found that the stability of Li_2S_n ($1 < n < 8$) increases with decreasing n , explaining the favorable thermodynamics of the reduction of S_8 to Li_2S . In a careful study, Moore¹⁷ presented a comprehensive set of predictions based on thermochemical data for possible reactions in the Li-S system using high-level quantum chemical methods. The computed Gibbs free energies for the dissociation/association of polysulfide anions and lithium polysulfides in solution were used to develop a detailed reaction network for the discharge process. This analysis supports the existence of the following major intermediates, S_2^{2-} , S_3^{2-} , S_4^{2-} , S_3^{1-} , and shows that upon complete utilization of S_8^{2-} the most abundant intermediate in solution is S_3^{2-} , in agreement with the earlier inferences from in-situ XANES studies. These findings are significant because they imply that a successful strategy to maximize sulfur utilization in a Li-S cell is to use cells based on

electrolytes enriched with Li_2S_3 .

Shuttling of the dissolved polysulfide species in the Li-S battery has been studied theoretically by Akridge and coworkers⁵³ using a continuum approach. In particular, beginning with the basic Nernst equations for each of the two plateaus and a diffusion/reaction term that describes the shuttle process, and by imposing a sulfur species balance and a charge balance. The authors were able to theoretically describe the charge and discharge profiles in the Li-S cell. Significantly, this work elegantly shows that self-discharge, poor charge-discharge efficiency, asymmetry of the charge profile, and overcharge protection are all facets of the same phenomenon in the Li-S cell.

1.4 Outline of the dissertation

This dissertation focus on three critical aspect of lithium sulfur battery to resolve the issues introduced above. Firstly is to sequestering LiPS by creating species in the cathode that binds specifically with LiPS. Three studies were carried out under this topic. The first study is to find out the ideal functional groups, and amine group is targeted due to its high binding energy with LiPS, stability in the cell and wide availability. The second study then applies this idea in a more efficient and applicable way, which focuses on the method for integrating amine group and CNT. The third study finds that the inorganic cathode materials TiS_2 also has high binding energy for LiPS, thus a hybrid cathode of TiS_2 and sulfur is built, where two species work synergistically to give higher capacity.

The second method is to localize the dissolved LiPS by creating an ionic shielding for LiPS. A high-transference number membrane containing sulfonate groups was designed, in which the PEG backbone and the SO_3^{2-} groups facilitate electrolyte wettability and Li^+ ion conduction

while the negatively charged membrane will at the same time reject sulfur species (S_n^{2-}) due to the repulsive electrostatic interactions. Such unique characteristics are attractive in modifying both positively and negatively charged ion transport within the cell.

The last part of the dissertation will talk about the protection of lithium metal anode in lithium sulfur battery. We report on the chemistry and interfacial properties of artificial SEI films created by in-situ reaction of a strong Lewis Acid AlI_3 , Li metal, and aprotic liquid electrolytes. We find that these SEI films impart exceptional interfacial stability to a Li metal anode. We further show that the improvements come from at least three processes: (i) in-situ formation of an Li-Al alloy; (ii) formation of a LiI salt layer at the interface; and (iii) creation of a stable oligomer thin film on the Li anode.

References

1. P. G. Bruce, S. A. Freunberger, L. J. Hardwick and J. M. Tarascon, *Nat. Mater.*, 2012, 11, 19-29.
2. B. Dunn, H. Kamath and J.-M. Tarascon, *Science*, 2011, 334, 928-935.
3. J. M. Tarascon and M. Armand, *Nature*, 2001, 414, 359-367.
4. C. Jiang, E. Hosono and H. Zhou, *Nano Today*, 2006, 1, 28-33.
5. K. T. Lee and J. Cho, *Nano Today*, 2011, 6, 28-41.
6. J. Hassoun and B. Scrosati, *Adv. Mater.*, 2010, 22, 5198-5201.
7. Z. Yang, J. Guo, S. K. Das, Y. Yu, Z. Zhou, H. D. Abruña and L. A. Archer, *J. Mater. Chem. A*, 2013, 1, 1433-1440.
8. Miller TJ (2009) *Electrical Energy Storage for Vehicles: Targets and Metrics*, Ford Motor Company
9. J. Gao and H. D. Abruña, *J. Phys. Chem. Lett.*, 2014, 5, 882-885.
10. B. Meyer, *Chem. Rev.*, 1964, 64, 429-451.
11. J. R. Akridge, Y. V. Mikhaylik and N. White, *Solid State Ion.*, 2004, 175, 243-245.
12. J. Wang, *Carbon*, 2008, 46, 229-235.
13. N. Jayaprakash, J. Shen, S. S. Moganty, A. Corona and L. A. Archer, *Angew. Chem.*, 2011, 50, 5904-5908.
14. Q. Zeng, D.-W. Wang, K.-H. Wu, Y. Li, F. Condi de Godoi and I. R. Gentle, *J. Mater. Chem. A*, 2014, 2, 6439-6447.
15. P. T. Cunningham, S. A. Johnson and E. J. Cairns, *J. Electrochem. Soc.*, 1972, 119, 1448-1450.
16. J. W. Choi, *Electrochim. Acta*, 2007, 52, 2075-2082.
17. R. S. Assary, L. A. Curtiss and J. S. Moore, *J. Phy. Chem. C*, 2014, 118, 11545-11558.
18. S. S. Zhang, *J. Power Sources*, 2013, 231, 153-162.

19. R. Elazari, G. Salitra, Y. Talyosef, J. Grinblat, C. Scordilis-Kelley, A. Xiao, J. Affinito and D. Aurbach, *J. Electrochem. Soc.*, 2010, 157, A1131-A1138.
20. F. Wu, J. Chen, R. Chen, S. Wu, L. Li, S. Chen and T. Zhao, *J. Phys. Chem. C*, 2011, 115, 6057-6063.
21. S.-E. Cheon, K.-S. Ko, J.-H. Cho, S.-W. Kim, E.-Y. Chin and H.-T. Kim, *J. Electrochem. Soc.*, 2003, 150, A796.
22. H. S. Ryu, Z. Guo, H. J. Ahn, G. B. Cho and H. Liu, *J. Power Sources*, 2009, 189, 1179-1183.
23. L. Yuan, X. Qiu, L. Chen and W. Zhu, *J. Power Sources*, 2009, 189, 127-132.
24. N. A. Cañas, S. Wolf, N. Wagner and K. A. Friedrich, *J. Power Sources*, 2013, 226, 313-319.
25. J. Nelson, S. Misra, Y. Yang, A. Jackson, Y. Liu, H. Wang, H. Dai, J. C. Andrews, Y. Cui and M. F. Toney, *J. Am. Chem. Soc.*, 2012, 134, 6337-6343.
26. S. Walus, C. Barchasz, J. F. Colin, J. F. Martin, E. Elkaim, J. C. Lepretre and F. Alloin, *Chem. Comm.*, 2013, 49, 7899-7901.
27. H.-S. Ryu, H.-J. Ahn, K.-W. Kim, J.-H. Ahn and J.-Y. Lee, *J. Power Sources*, 2006, 153, 360-364.
28. Y. Wang, Y. Huang, W. Wang, C. Huang, Z. Yu, H. Zhang, J. Sun, A. Wang and K. Yuan, *Electrochim. Acta*, 2009, 54, 4062-4066.
29. M. A. Lowe, J. Gao and H. D. Abruña, *RSC Adv.*, 2014, 4, 18347-18353.
30. M. U. Patel, R. Demir-Cakan, M. Morcrette, J. M. Tarascon, M. Gaberscek and R. Dominko, *ChemSusChem*, 2013, 6, 1177-1181.
31. M. U. Patel and R. Dominko, *ChemSusChem*, 2014, 7, 2167-2175.
32. C. Barchasz, F. Molton, C. Duboc, J. C. Lepretre, S. Patoux and F. Alloin, *Anal. Chem.*, 2012, 84, 3973-3980.
33. N. A. Cañas, D. N. Fronczek, N. Wagner, A. Latz and K. A. Friedrich, *J. Phys. Chem. C*, 2014, 118, 12106-12114.
34. Q. Pang, D. Kundu, M. Cuisinier and L. F. Nazar, *Nat. Comm.*, 2014, 5, 4759.
35. X. Tao, J. Wang, Z. Ying, Q. Cai, G. Zheng, Y. Gan, H. Huang, Y. Xia, C. Liang, W. Zhang and Y. Cui, *Nano Lett.*, 2014, 14, 5288-5294.

36. R. Demir-Cakan, M. Morcrette, Gangulibabu, A. Guéguen, R. Dedryvère and J.-M. Tarascon, *Energy Environ. Sci.*, 2013, 6, 176-182.
37. L. Zhang, L. Ji, P. A. Glans, Y. Zhang, J. Zhu and J. Guo, *Phys. Chem. Chem. Phys.*, 2012, 14, 13670-13675.
38. J. Guo, Z. Yang, Y. Yu, H. D. Abruna and L. A. Archer, *J. Am. Chem. Soc.*, 2013, 135, 763-767.
39. L. Ma, H. Zhuang, Y. Lu, S. S. Moganty, R. G. Hennig and L. A. Archer, *Adv. Energy Mater.*, 2014, 4, 1400390.
40. N. A. Cañas, K. Hirose, B. Pascucci, N. Wagner, K. A. Friedrich and R. Hiesgen, *Electrochim. Acta*, 2013, 97, 42-51.
41. M. Cuisinier, P.-E. Cabelguen, S. Evers, G. He, M. Kolbeck, A. Garsuch, T. Bolin, M. Balasubramanian and L. F. Nazar, *J. Phys. Chem. Lett.*, 2013, 4, 3227-3232.
42. T. A. Pascal, K. H. Wujcik, J. Velasco-Velez, C. Wu, A. A. Teran, M. Kapilashrami, J. Cabana, J. Guo, M. Salmeron, N. Balsara and D. Prendergast, *J. Phys. Chem. Lett.*, 2014, 5, 1547-1551.
43. M. U. Patel, I. Arcon, G. Aquilanti, L. Stievano, G. Mali and R. Dominko, *Chemphyschem*, 2014, 15, 894-904.
44. Z. Li, Y. Jiang, L. Yuan, Z. Yi, C. Wu, Y. Liu, P. Strasser and Y. Huang, *ACS Nano*, 2014, 8, 9295-9303.
45. X.-Q. Zhang, Q. Sun, W. Dong, D. Li, A.-H. Lu, J.-Q. Mu and W.-C. Li, *J. Mater. Chem. A*, 2013, 1, 9449-9455.
46. X. Tao, X. Chen, Y. Xia, H. Huang, Y. Gan, R. Wu, F. Chen and W. Zhang, *J. Mater. Chem. A*, 2013, 1, 3295-3301.
47. L. Ji, M. Rao, S. Aloni, L. Wang, E. J. Cairns and Y. Zhang, *Energy Environ. Sci.*, 2011, 4, 5053-5059.
48. Y. -J. Choi, Y. -D. Chung, C. -Y. Baek, K.-W. Kim, H.-J. Ahn and J.-H. Ahn, *J. Power Sources*, 2008, 184, 548-552.
49. S. Xiong, K. Xie, Y. Diao and X. Hong, *Ionics*, 2012, 18, 867-872.
50. N. S. Choi, Z. Chen, S. A. Freunberger, X. Ji, Y. K. Sun, K. Amine, G. Yushin, L. F. Nazar, J. Cho and P. G. Bruce, *Angew. Chem.*, 2012, 51, 9994-10024.
51. J. Wang, J. Chen, K. Konstantinov, L. Zhao, S. H. Ng, G. X. Wang, Z. P. Guo and H. K.

Liu, *Electrochim. Acta*, 2006, 51, 4634-4638.

52. L. Wang, T. Zhang, S. Yang, F. Cheng, J. Liang and J. Chen, *J. Energy Chem.*, 2013, 22, 72-77.

53. Y. V. Mikhaylik and J. R. Akridge, *J. Electrochem. Soc.*, 2004, 151, A1969-A1976.

CHAPTER 2

Tethered Molecular Sorbents: Enabling Metal-Sulfur Battery Cathodes

Adapted with permission from

L. Ma, H. L. Zhuang, Y. Lu, S. S. Moganty, R. G. Hennig and L. A. Archer, Tethered Molecular Sorbents: Enabling Metal-Sulfur Battery Cathodes. *Advanced Energy Materials*, 2014, 4, 1400390.

2.1 Abstract

A rechargeable battery that employs sulfur at the cathode and a metal (e.g. Li, Na, Mg, or Al) at the anode provides perhaps the most promising path to a solid-state electrochemical storage device capable of high charge storage capacity. It is now understood that solubilization in the electrolyte and loss of sulfur in the form of long-chain lithium polysulfides (Li_2S_x , $2 < x < 8$) has hindered development of the most studied of these devices, the rechargeable Li-S battery. Beginning with density-functional calculations of the structure and interactions of a generic lithium polysulfide species with nitrile containing molecules, we show that it is possible to design nitrile-rich molecular sorbents that anchor to other components in a sulfur cathode and which exert high-enough binding affinity to Li_2S_x to limit its loss to the electrolyte. We find that sorbents based on amines and imidazolium chloride present barriers to dissolution of long-chain Li_2S_x and that introduction of as little as 2 w% of these molecules to a physical sulfur-carbon blend, leads to Li-S battery cathodes that exhibit stable long-term cycling behaviors at both high and low charge/discharge rates.

2.2 Introduction

Portable devices are being developed with increasing sophistication to meet rising consumer

demand for faster, smaller, smarter, more powerful machines that can provide improvements in productivity and connectivity. These needs require electrochemical storage technologies with higher specific capacities, improved safety, and longer performance lifetimes. Rechargeable batteries that achieve these performance metrics using earth-abundant materials offer additional attractive attributes, such as cost and scalability, considered key requirements for grid storage from intermittent sources, such as wind and solar. Additionally, the increasing number of motorized vehicles in developing societies and the resulting pollution produced by their harmful emissions calls for a transformation in the energy systems that power transportation.¹

Among rechargeable battery technologies, cells based on a sulfur cathode stand out as uniquely suited to these needs. Sulfur is cheap (\$0.02/g), abundant in regions all over the world, capable of storing vast amounts of electrochemical energy, and in its pristine form, is environmentally benign.²⁻⁵ A rechargeable lithium battery with a sulfur cathode and metallic lithium anode offers the highest theoretical specific energy (2.6 kW·h/kg) among solid state batteries. The theoretical specific energy of such a Li-S battery is more than one third the maximum energy that can be achieved by burning coal (6.7 kW·h/kg) and close to one fifth the energy density of commercial-grade gasoline, 12.5 kW·h/kg. Indeed, even accounting for the typical factor of 3 reduction in storage capacity from other cell components, Li-S batteries offer practical specific energies that can be a factor of 3 or more higher than existing rechargeable battery technology.² If the anode is sodium, a high specific energy (0.8 kW·h/kg) is possible at a fraction of the cost of the Li-S battery.

Commercially viable rechargeable batteries based on sulfur cathodes require solutions to several technical challenges.⁶⁻¹¹ First, the low electrical conductivity of sulfur (5×10^{-30} S/cm at 25 °C)

and its reduction compounds, sulfides, result in poor electrochemical contacts within the cathode, limiting utilization of the active electrode material. The shuttling of metal polysulfides is another serious problem; during discharge of a Li-S battery for example, lithium polysulfide ($Li_2S_n, 2 < n < 8$) is generated at the cathode, and dissolves into the electrolyte. The concentration gradient of polysulfide drives migration to the anode, causing chemical reactions with the lithium metal to form lower order polysulfides, including insoluble Li_2S_2 and Li_2S , which will deposit on the Li anode. Any soluble lower-order polysulfides generated in this reaction are free to diffuse back to the sulfur cathode, to react with sulfur and reform higher-order polysulfides. Therefore, the dissolution of polysulfides leads to not only loss of the active material and degradation in storage capacity of the Li-S cell, but can consume uncontrolled, large amounts of electrical energy during the charge cycle, lowering the Coulombic efficiency of the cell.

Researchers have proposed different methods to prevent polysulfide dissolution and shuttling in Li-S batteries. Many of the most successful approaches focus on physically restraining polysulfide dissolution using barrier materials, including micro- and mesoporous carbon as capsules for sulfur,¹¹⁻¹⁸ or incorporating sulfur into carbon nanotubes,^{19,20} graphene/graphene oxide sheets.^{21,22} However, very few studies have characterized the time-dependent loss of Li_2S_x from these cathodes. It is understood, however, that because the barrier to Li_2S_x dissolution in the electrolyte is kinetic, polysulfides physically trapped in the meso- or nanopores of a carbon host will eventually leach into the electrolyte leading to premature cell failure. Another drawback of these methods is that the energy cost of melting or vaporizing sulfur to infuse it into the pores of a host material can be quite high.

A recent study by Guo et al. suggests that interactions between lithium ions and nitrile groups in

high-molar mass polyacrylonitrile (PAN) chains in solution can be used to cross-link the polymer via Li_2S_x bridges.²³ Even after high-temperature pyrolysis of the PAN, the authors found that the sulfur remained anchored at the cross-links; such that carbon- Li_2S composites in which Li_2S is uniformly distributed in a carbon host results. The ability of the PAN chains to pull Li_2S_x species out of solution and to maintain their spatial distribution even at high temperature imply that the binding forces between Li_2S_x and PAN are strong and specific. Inspired by these observations, we theorized that similar types of interactions with other species in a sulfur cathode might be used to create thermodynamic barriers of defined size that permanently limit dissolution of long-chain lithium polysulfide in an electrolyte.

In this Article we report a facile route towards such sulfur-carbon composite cathodes that take advantage of strong lithium-nitrile interactions to limit lithium polysulfide dissolution in electrolytes. The approach is general, scalable, and based on a recent literature report,² it should also be directly applicable to oxygen-containing sorbent molecules. Beginning with a theoretical analysis of the structure and interactions of a generic lithium polysulfide species with nitrile containing molecules, we show that it is possible to rationally design sorbents that anchor to other cathode components and which exert high-enough binding affinity to Li_2S_x created near the carbon-electrolyte interface to prevent its loss to the electrolyte. We further find that alkoxy silane-functionalized amine and imidazolium chloride molecules exhibit binding energies for Li_2S_x that are higher than those computed for PAN and that when incorporated in a sulfur cathode, these molecules produce measureable improvements in electrochemical properties and lifetime of the electrode.

2.3 Results and Discussion

Figure 2.1 illustrates the approach used to create carbon/sulfur composite cathodes capable of sequestering lithium polysulfides through lithium-nitrile interactions. A mixture of carbon, sulfur, N-Methyl-2-pyrrolidone (NMP) solvent, and a nitrile-containing molecular sorbent is first formed by mechanical mixing of the components at high speed (step 1). Trace amounts of moisture and thermal energy added to remove the NMP solvent causes alkoxy silane groups to cross-link and anchor sparsely (step 2) to the surface of carbon conductivity aids via carboxylic acid, phenols, and other hydroxyl species present on the surface of the carbon. Upon battery discharge (step 3), it is supposed that lithium polysulfide species created in the discharge process bind to the tethered nitrile groups via the lithium-nitrile attraction, stabilizing the cathode against polysulfide loss to the electrolyte.

The binding energy E_b was calculated for a generic lithium polysulfide ($\text{Li-S}\bullet$) with PAN and two other nitrile-containing candidate sorbent molecules (3-trimethoxysilylpropyl) diethylenetriamine (TMS-PDTA) and 1-methy-3-trimethoxysilane imidazolium chloride (IM-Cl), with alkoxy silane anchoring groups (see **Figure 2.2**) that can bind to other components in a sulfur cathode. The density-functional calculations were performed with Gaussian09 using the PBE exchange-correlation functional and the cc-pVDZ basis sets.²⁴ **Figure 2.2** compares the binding energies for the two molecules with PAN and a fourth polymer, polyvinyl pyrrolidone (PVP) sometimes used as a binder in lithium battery electrodes. It is apparent from the figure that all of these molecules have sizable binding energies, with the values for IM-Cl being substantially larger than for any of the other species studied. It should be noted that our calculated binding energies are significantly larger than those computed between $\text{Li-S}\bullet$ species

and various vinyl polymers, which range from 0.30-1.26 eV,²⁵ indicating much stronger binding of the Li-S• species with the selected materials.

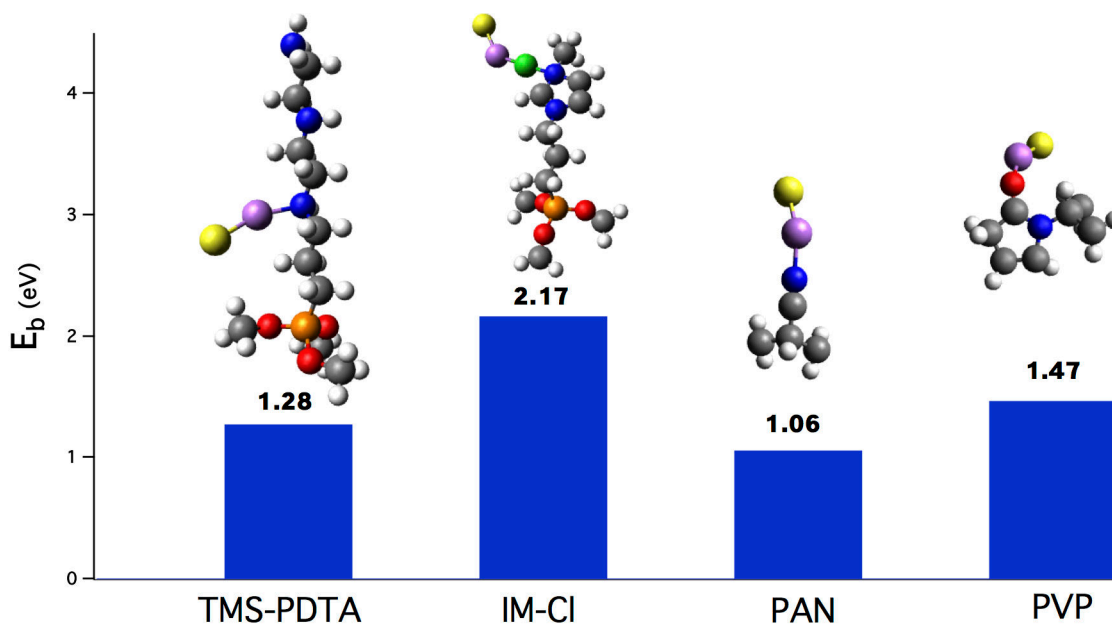


Figure 2.2 Density-functional theoretical results for the equilibrated structures and binding energies E_b for a representative long-chain lithium polysulfide ($\text{Li-S}\bullet$) with four nitrile-containing molecules: (3-trimethoxysilylpropyl) diethylenetriamine (TMS-PDTA); 1-methy-3-trimethoxysilane imidazolium chloride (IM-Cl); polyacrylonitrile (PAN); polyvinyl pyrrolidone (PVP). Yellow circles in the structures represent polysulfide species S_x ; purple – lithium; blue – nitrogen; gray – carbon; orange – silicon; red – oxygen; white – hydrogen; green – chlorine.

The relaxed structures determined by the density-functional calculations provide important additional insights into how the architecture and placement of the nitrile groups influence interactions with Li_2S_x molecules. Specifically, the figure shows that when isolated nitrile groups are part of an aliphatic open chain segment, as in PAN, Li_2S_x bonds via direct interactions between lithium and the nitrogen atoms along the chain segment. In situations where there are multiple nitrile groups in a single molecule, as in TMS-PDTA, Li_2S_x again bonds via lithium-nitrile interactions, but there is a preference for one of the three binding locations. Finally, when the nitrile groups are incorporated in a ring structure (e.g. IM-Cl and PVP), the Li_2S_x does not bond via lithium-nitrile interactions, but rather are anchored by strong lithium-oxygen (e.g. PVP) and even stronger lithium-chlorine (e.g. IM-Cl) bridges. Although one can provide reasonable a-posteriori explanations of these observations in terms of the relative stability of the net dipole that must exist on the sorbent site at which the Li_2S_x binds, our observations underscore how subtle details in molecular design of a sorbent might change both the strength and topography of its interactions with Li_2S_x and the accessibility of the sequestered lithium polysulfide to an electrolyte.

The DFT calculations of IR were carried out on TMS-PDTA and the mixture of TMS-PDTA and Lithium polysulfide respectively. **Figure 2.3a** shows the IR spectra of TMS-PDTA and Li-S-TMS-PDTA. We can see that the interactions between polysulfide and N in sorbent give rise to an additional Li-N stretch mode with the characteristic frequency of 630 cm^{-1} . This value is slightly different from the reference one calculated for a different material consisting of a strong Li-N bond²⁶, confirming our hypothesis that Li ions are significantly bonded with the electrophile center (Nitrogen) in amine group. The same calculation was carried out on IM-Cl and the mixture of IM-Cl and Lithium polysulfide respectively. The plot in **Figure 2.3b** shows a

new sharp band in the IM-Cl/Li-S blend near 2850 cm^{-1} instead of 630 cm^{-1} , and the new peak is actually the N-H band²⁷ in IM. When IM-Cl is mixed with Lithium polysulfide, the Li ion interacts with the Cl^{-1} , the Cl^{-1} lets go of the NH and this band appears.

Electrodes prepared according to the procedures described in the experimental section were used to characterize interactions between Li_2S_x , TMS-PDTA and IM-Cl using a range of physical and electrochemical testing procedures. **Figure 2.4a** is the infrared spectra for TMS-PDTA and a TMS-PDTA/lithium polysulfide mixture comprised of 50w% TMS-PDTA and 50w% Li_2S_4 dissolved in tetraglyme, an excellent solvent for Li_2S_4 . The band at 3296 cm^{-1} is characteristic of the N-H stretch associated with the three amine groups emanating from the hydrocarbon tail of TMS-PDTA. When TMS-PDTA is physically blended with Li_2S_4 , the N-H stretch is seen to shift by nearly 40 cm^{-1} (from 3296 cm^{-1} to 3250 cm^{-1}). Significantly, this shift is not observed for any of the other vibration modes associated with the CH_2 bend (1455 cm^{-1}) and C-O stretch (1192 cm^{-1}). This observation is an expected consequence of the strong interactions predicted between the nitrile group in TMS-PDTA and the lithium polysulfide species. The corresponding infrared spectra for 1-methy-3-trimethoxysilane imidazolium chloride are provided in **Figure 2.4b**. In this case there is no obvious shift produced by the lithium polysulfide mixture, notwithstanding the high E_b value for this pair. A straightforward explanation for both observations is apparent from the structure calculations provided in **Figure 2.2**; namely in the case of IM-Cl the Li_2S_x bonds to the sorbent molecule via a strong, likely ionic, Li-Cl linkage.

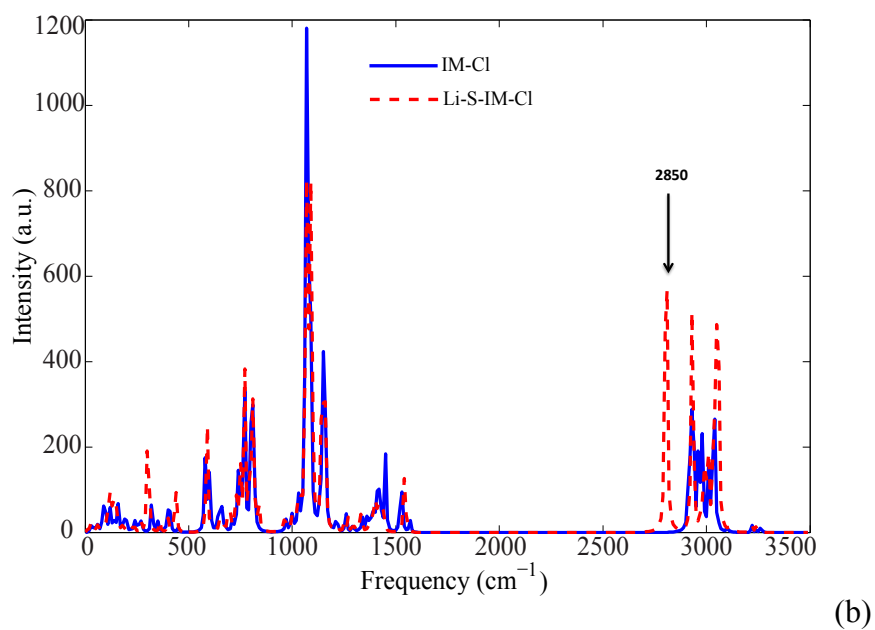
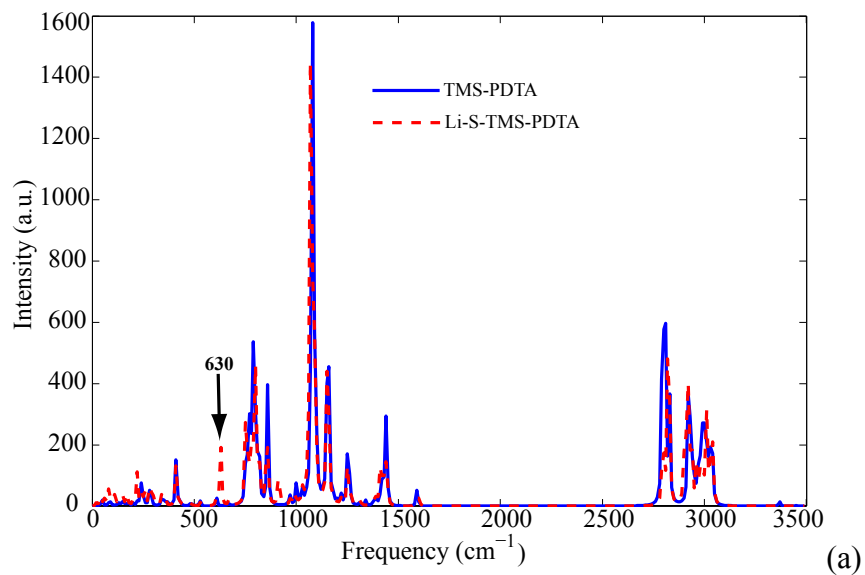
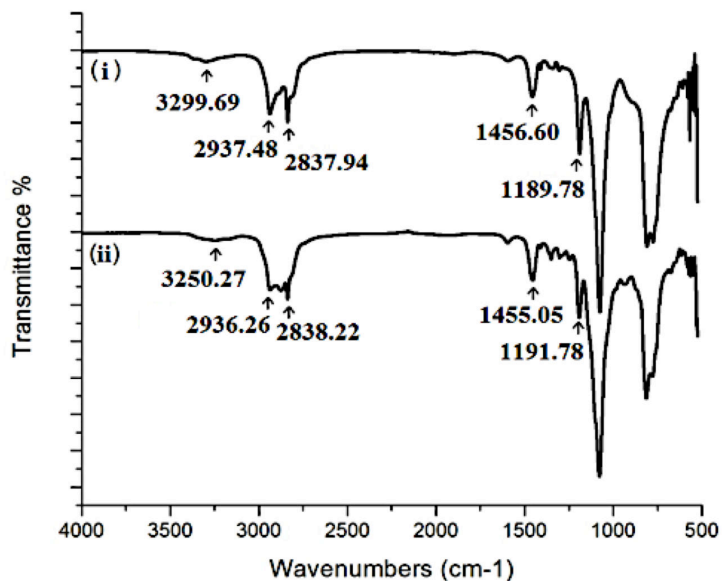
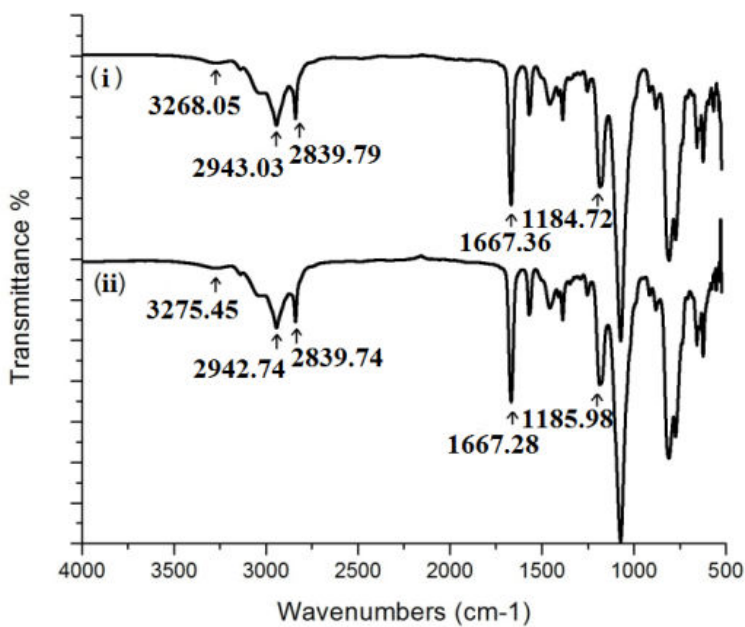


Figure 2.3 DFT calculation of IR on (a) TMS-PDTA and the mixture of TMS-PDTA and Lithium polysulfide; (b) IM-Cl and the mixture of IM-Cl and lithium polysulfide.



(a)



(b)

Figure 2.4 (a): FTIR spectra of electrodes comprised of pure TMS-PDTA (i) and a mixture of polysulfides and TMS-PDTA (ii); (b): pure IM-Cl (i) and mixture of polysulfides and IM-Cl (ii).

A more direct approach for evaluating the binding affinity of TMS-PDTA and IM-Cl for Li_2S_x is to characterize the dissolution of the polysulfide in a good solvent. For this purpose, we immersed cathodes comprised of Li_2S_4 or Li_2S_9 and a binder in tetraethylene glycol dimethyl ether (tetraglyme), a good solvent for Li_2S_x ($x > 2$) and characterized the time-dependent content of the respective polysulfides dissolved in the electrolyte. **Figure 2.5a** shows the raw ICP-AES data for elemental lithium obtained at $t = 10$ and $t = 60$ mins for an electrode containing pristine Li_2S_4 (i.e. no additives); the corresponding results for sulfur are shown in **Figure 2.5b**. By comparing the peak values with data obtained from calibration experiments, it is possible to quantify the content of Li_2S_x in the electrolyte as a function of time. **Figure 2.5c** presents results for the time-dependent concentration of sulfur in tetraglyme for cathodes based on pristine Li_2S_4 (i.e. no sorbent) and those containing IM-Cl and TMS-PDTA. The figure clearly shows that consistent with expectations from the calculated E_b values, the presence IM-Cl or TMS-PDTA sorbent dramatically reduces polysulfide loss to tetraglyme. Notably, the figure further shows that even at a bulk concentration of 6w%, the IM-Cl effectively eliminates dissolution of Li_2S_4 in tetraglyme. As a perhaps extreme example, similar measurements were performed using Li_2S_9 and the results are reported in **Figure S2.1**. In this case both sorbents are again observed to reduce lithium polysulfide loss to the electrolyte, but the effects are not as dramatic as for Li_2S_4 . Considering that Li_2S_x are less soluble in the DOL/DME mixture electrolyte used in most lithium/sulfur cells, we anticipate that a sulfur cathode incorporating IM-Cl or TMS-PDTA should manifest vastly improved cycling behavior in metal-sulfur cells.

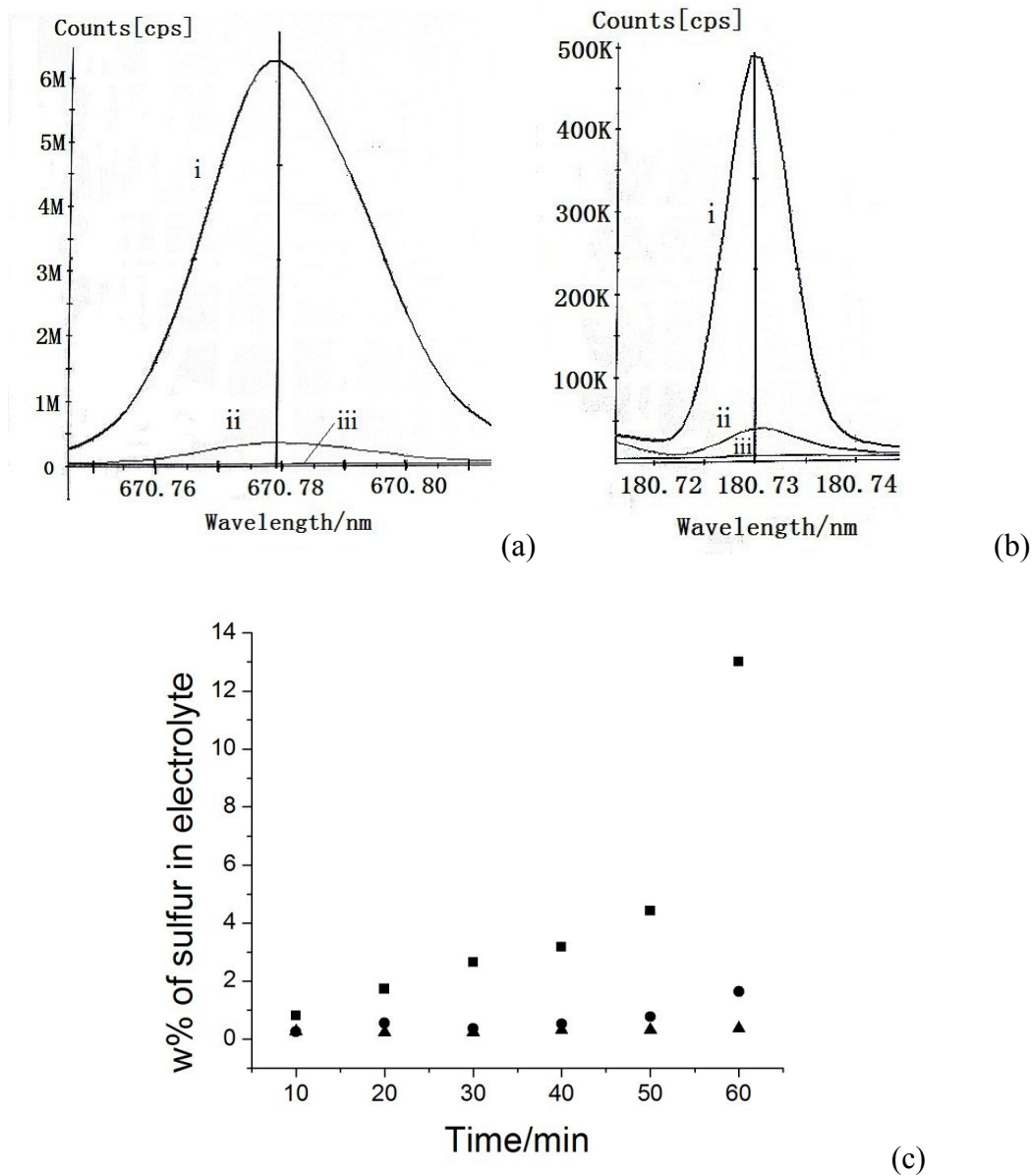
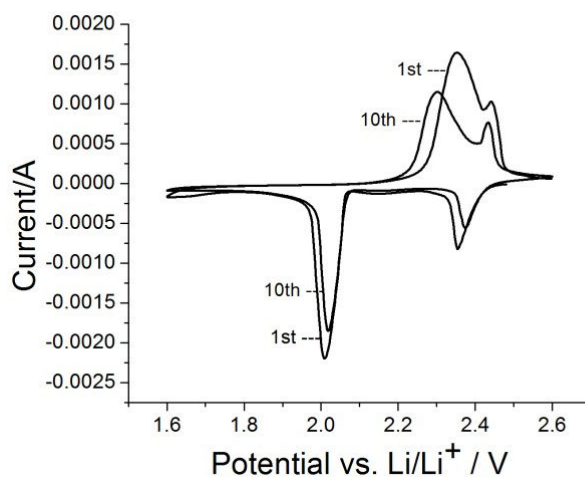


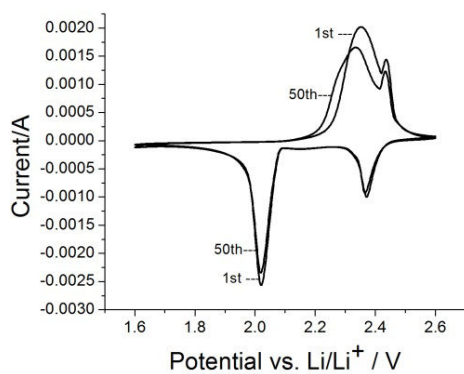
Figure 2.5 ICP-AES characterization of time-dependent Li_2S_4 dissolution in tetraglyme. (a) Raw data for elemental Li: (i) $t = 60$ mins; (ii) $t = 10$ mins; (iii) = blank (baseline). (b) Raw data for elemental sulfur: (i) $t = 60$ mins; (ii) $t = 10$ mins; (iii)=blank (baseline). (c) Sulfur content in tetraglyme for three different cases (squares represent the case of no sorbent; circles with TMS-PDTA; triangles with IM-Cl).

Figure 2.6a – 2.6c report cyclic voltammograms (CV) of Li/S cells containing (a) no sorbent, (b) 6w% TMS-PDTA and (c) 6w% IM-Cl as molecular sorbents in the cathode, with a scanning rate of 0.1mV/s. During discharge/charge process, a pair of redox peaks is observed in every case at potentials consistent with the two stages of reduction and oxidation of sulfur. Compared with the cathode without sorbent (**Figure 2.6a**), which already show noticeable changes in peak positions and current amplitudes by the 10th cycle, cells utilizing cathodes with either the TMS-PDTA or IM-Cl species show no noticeable changes even after 50 cycles. These results simultaneously demonstrate that both sorbents are electrochemically stable and are highly effective in preventing capacity fading due to the loss of sulfur and sulfides into the electrolyte and in maintaining high utilization of the active sulfur in the redox reactions.

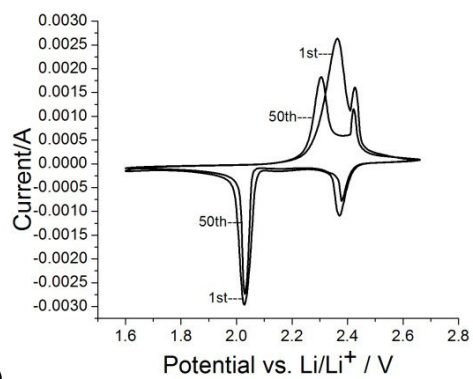
Voltage profiles for Li-S cells with and without TMS-PDTA or IM-Cl in the cathode are shown in **Figure 2.7a and 2.7b**. These data were obtained from galvanostatic measurements at a fixed current density of 335 mA/g (0.2 C, based on the theoretical capacity of sulfur). It is evident from the figure that two voltage plateaus (~2.4 V and ~2.0 V), corresponding to the reduction of sulfur from high order Lithium polysulfide to lower order lithium polysulfide are observed over many cycles.



(a)

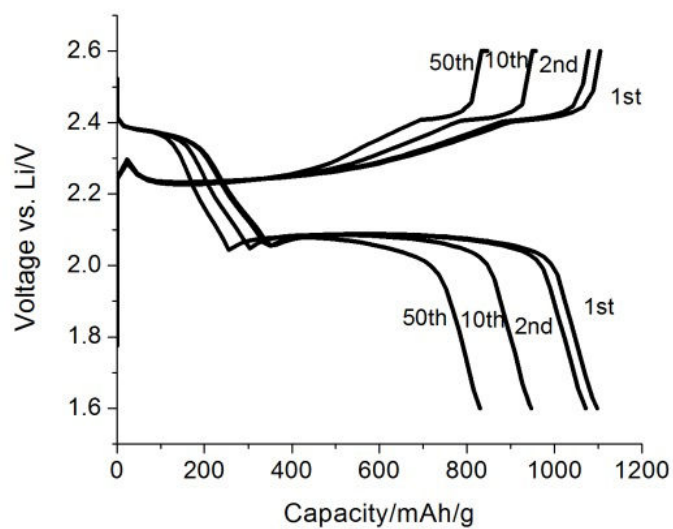


(b)

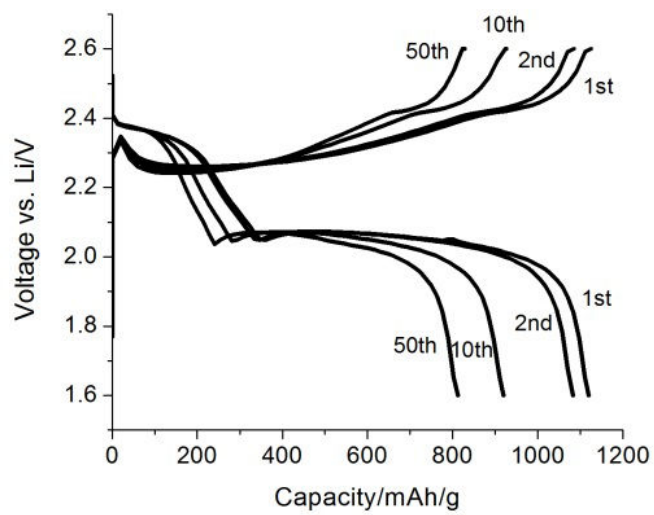


(c)

Figure 2.6 Galvanostatic voltage profile for Li-S cells: (a) without the molecular sorbent in the cathode; (b) with TMS-PDTA (c) IM-Cl.



(a)



(b)

Figure 2.7 Voltage vs. capacity profiles for Li-S cells with: (a) 6w% TMS-PDTA and (b) 6w% IM-Cl sorbents in the cathode.

Figure 2.8 shows the long-term cycling performance of Li-S batteries with 50w% sulfur, 6w% TMS-PDTA and IM-Cl, as well as without the sorbents, galvanostatically cycled at current densities of 0.2C. It is apparent in **Figure 2.8** that the electrodes with either sorbent exhibit markedly improved cyclability and Columbic efficiency close to 100% (i.e. essentially no shuttling) even after 100 cycles. The results are most dramatic at the high C rate where Li-S cells without the cathode additives rapidly fail, but those containing the sorbent additive exhibit stable cycling performance upon extended cycling (**Figure S2.2**). The stability of the cathode material is also evidenced by the recovery of capacity at 0.1C following charging at high rate of 1C (**Figure S2.3**). The specific capacity retention of each cathode material with or without additives is given in **Table 2.1**. The advantage of adding additives is very obvious at 0.2C already and even more significant when the current rate is up to 1C.

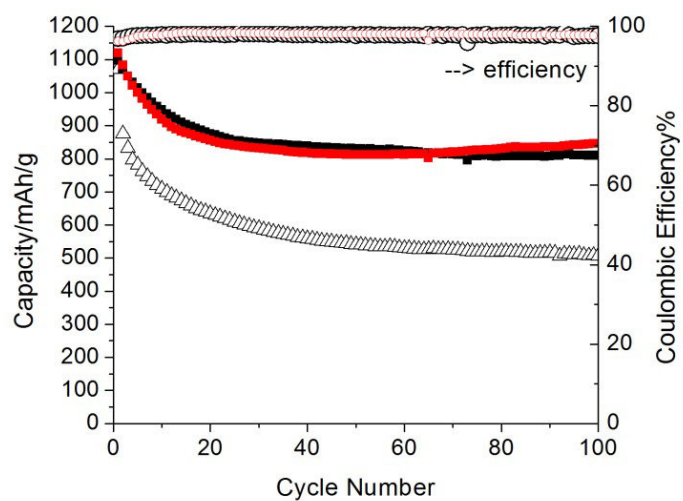
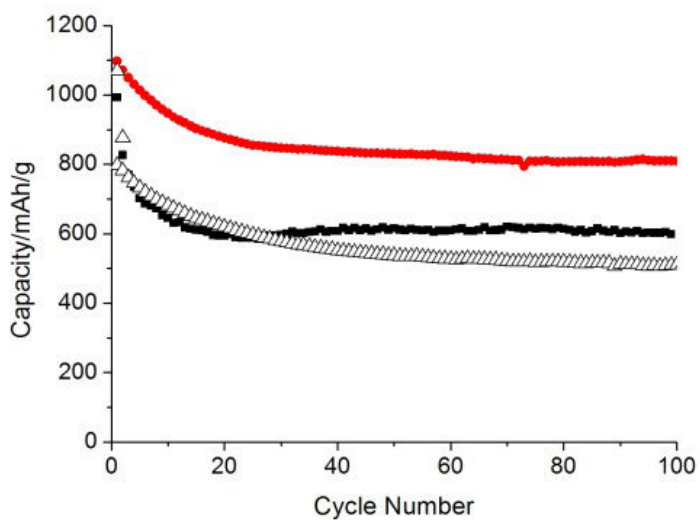


Figure 2.8 Long-term cycling performance of Li-S batteries without additives (black triangle), with TMS-PDTA (black square) and the corresponding Coulombic efficiency represented as black cycle, with IM-Cl (red square) and the corresponding Coulombic efficiency represented as red cycle at 0.2C

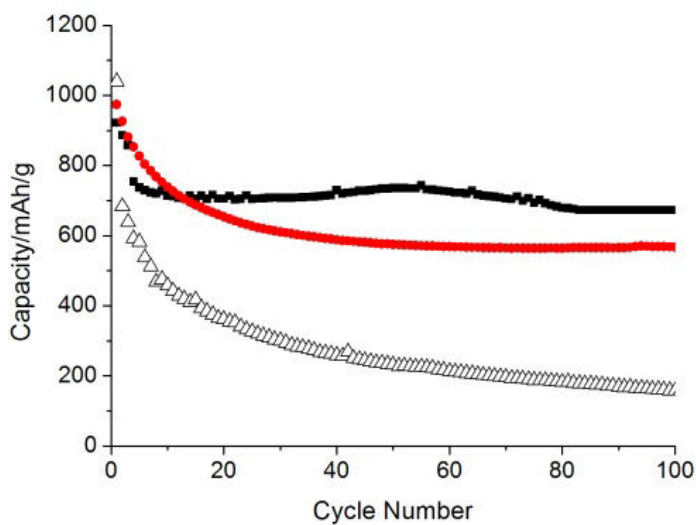
Table 2.1 The percentage of discharge capacity retained of each cathode with or without additives after 100 cycles in comparison to the tenth cycle capacity.

	0.2C			1C		
	No additive	TMS-PDTA	IM-Cl	No additive	TMS-PDTA	IM-Cl
C_{100}/C_{10} %	70	86	94	34	77	80

We also prepared sulfur-carbon composite cathodes with different TMS-PDTA sorbent contents and compared their cycling performance under galvanostatic charge/discharge conditions. **Figure 2.9** shows that at low current rates, cathodes with 6w% of TMS-PDTA exhibit the highest charge storage per unit mass. On the other hand, at a high current density of 1C, cathodes with the lowest sorbent content (2w%) yield the highest capacity. These trends can be explained in terms of the competing effects the sorbents have on cathode performance. Specifically, the ability of the sorbents to attract the polysulfides and keep them in the cathode should grow as the content of sorbent, and hence proximity to polysulfides in the cathode, rises. However, the silane anchoring groups in the TMS-PDTA makes it insulating; addition of more sorbent increases this effect, which compromises sulfur utilization in the cathode particularly at high currents – precisely what we observe.



(a)



(b)

Figure 2.9 Comparison of Li-S battery performance with different weight fractions of PMS-PDTA in the cathode: without additives (black triangle), with 6w% TMS-PDTA (red square), with 2w% IM-Cl (a) Cells cycled at 0.2 C; (b) Cycled at 1C.

SEM images of the cathode before and after discharge and charge are reported in **Figure 2.10**. Upon cycling of these cathodes in Li-S cells, it is apparent that the sorbent again gives rise to significant differences. Comparison of **Figures 2.10b and 2.10d** indicates that the morphology of the electrodes containing TMS-PDTA changes little during 100 cycles of charge and discharge. On the other hand, cathodes without the molecular sorbent exhibit large changes in morphology after cycling. In particular, many rod-like particulate structures are formed in these cathodes giving them a somewhat open, porous morphology. We believe these differences stem directly from the loss of sulfur to the electrolyte in the former materials, which produces consolidation and aggregation of the carbon particles left behind. More remarkable to us, however, is the absence of any noticeable change in morphology of the cathodes containing the TMS-PDTA. This observation is significant because as shown in **Figure 2.8** the discharge capacity of these cells after 100 cycles is quite stable, but substantially lower than the theoretical capacity of sulfur. We believe these results imply that poor sulfur utilization due to reduced electrical conductivity (e.g. as produced by choking by insulative Li_2S electrodeposits in the cathode) of the cathode, as opposed to sulfur loss to the electrolyte, is the source of the lower than theoretical capacities observed. Electrochemical impedance spectroscopy (EIS) results of cells with TMS-PDTA before and after cycles are provided in **Figure S2.4**. The conductivity of sulfur cathode and the cathode surface properties will strongly affect the charge-transfer resistance (R_{ct}), and the increase of R_{ct} indicates the formation of the insulating solid film of Li_2S and Li_2S_2 . Also, the production of insulating reduction products on cathode surface could increase the interphase contact resistance and enlarge R_{int} .²⁸ The cumulative agglomerates will decrease the electrically conductive area on the cathode surface and hinder the transportation of ions toward the inside of the cathode, resulting in slow transfer reaction kinetic and capacity

fading. Hence, the observed increase of R_{ct} and R_{int} in **Figure S2.4** indicates that the limited sulfur utilization is due to the insulated Li_2S formation on the electrode and further reduction of the electrical conductivity.

Figure 2.11 shows TEM images of the composite cathodes with TMS-PDTA and IM-Cl sorbents. To determine the distribution of sulfur in the composites, elemental identification was performed after 100 cycles. **Figure 2.11b and 2.11c** shows the energy dispersive X-ray (EDX) maps for carbon and sulfur based on the area shown in the annular dark field (ADF) image of the cathode materials with TMS-PDTA. The edge of carbon and sulfur EDX maps in **Figure 2.11b and 2.11c** matches results shown in the ADF image, indicating that carbon and sulfur are homogeneously distributed throughout the composite. The analysis can also be applied to the cathode materials containing the tethered IM-Cl sorbent (**Figure 2.11e and 2.11f**), again showing that the distribution of carbon and sulfur is homogeneous in the composite.

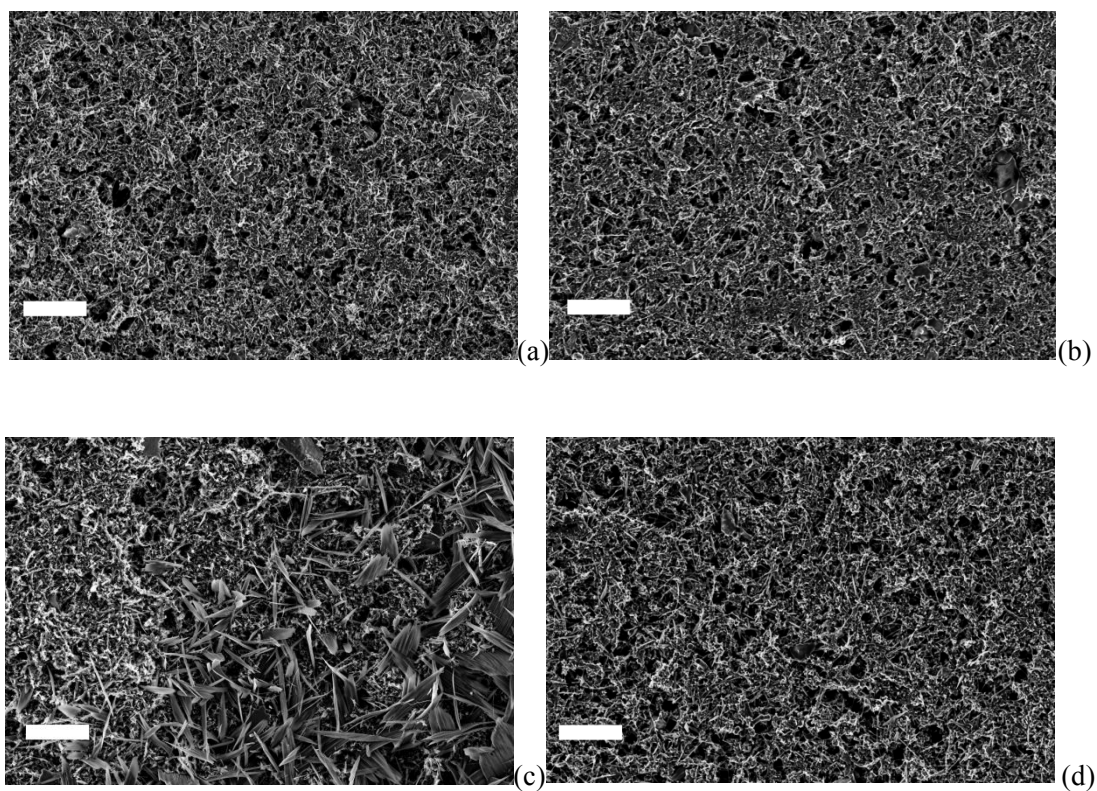


Figure 2.10 SEM images of the L-S battery cathode before and after galvanostatic cycling at a fixed rate of 335 mA/g (0.2C). (a) Cathode with 6w% TMS-PDTA before charge/discharge; (b) Same as (a) except without sorbent; (c) Same as (a), but after 100 charge-discharge cycles; (d) Same as (b) but after 100 cycles. Scale bar= $10\ \mu\text{m}$

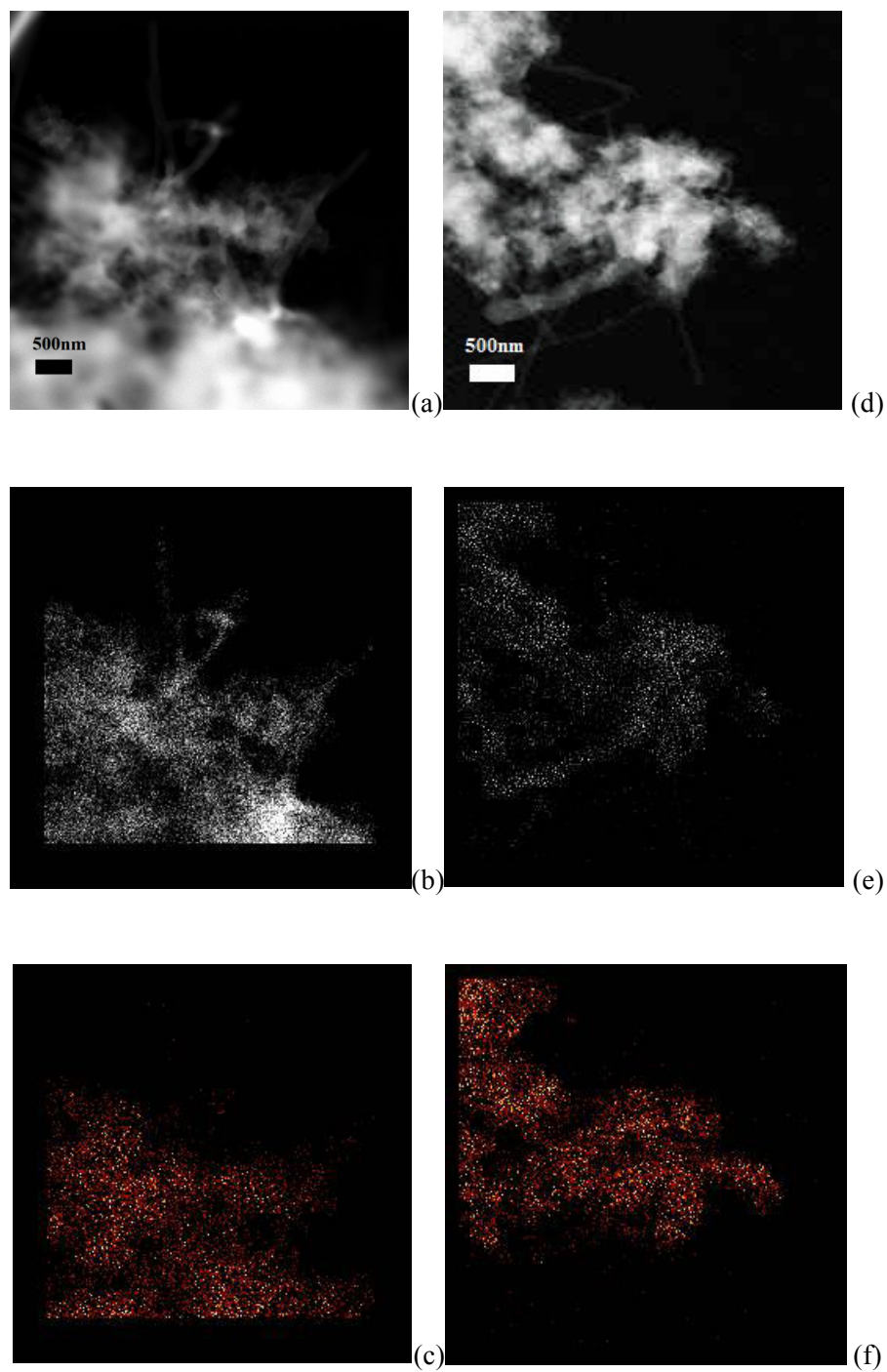


Figure 2.11 TEM images of the L-S battery cathode after galvanostatic cycling at a fixed rate of 335 mA/g (0.2C). (a) Cathode with 6w% TMS-PDТА after 100 charge-discharge cycles; (d) Same as (a) except with 6w% IM-Cl; (b and c) EDX carbon and sulfur maps based on the area shown in (a); (e and f) EDX carbon and sulfur maps based on the area shown in (d).

2.4 Experimental Section

2.4.1 Synthesis of electrode materials

3-trimethoxysilylpropyl diethylenetriamine was obtained from Gelest, Inc and used as received. 1-methy-3-trimethoxysilane imidazolium chloride was synthesized according to a previously described method.²⁹ Two lithium polysulfide species, Li_2S_4 and Li_2S_9 , were used to experimentally characterize interactions between the additive molecules in **Figure 2.2** and lithium polysulfides. To synthesize Li_2S_4 , 920mg Li_2S , 3.2g sulfur and 0.5g lithium powder (from FMC Lithium) were added to 5mL tetraglyme (tetraethylene glycol dimethyl ether) and stirred for 24hrs. The mixture was filtered to obtain a dark reddish liquid. The synthesis was performed with and without TMS-PDTA. Following Rauh et al's procedure,^{30,31} Li_2S_9 was prepared in a solution process wherein stoichiometric amounts of elemental sulfur, S_8 , and Li_2S were co-dissolved into tetraglyme, followed by heating at 80 °C with magnetic stirring for 6h. Composite carbon sulfur cathodes were created on aluminum foil using slurries containing 50w% sulfur powder, 20w% Vapor grown carbon fibers³² from Showa Denko USA, 20w% Super-P Li from TIMCAL, and 10w% poly(vinylidene difluoride) (PVDF, Sigma Aldrich) as binder in an excess of N-Methyl-2-pyrrolidone (NMP). Electrodes containing TMS-PDTA sorbents were created by first dissolving TMS-PDTA in the desired concentration in NMP and blending the resultant solution into the slurry using a ball mill. The slurry Electrodes for physical and electrochemical analysis were obtained by coating the slurry on Aluminum foil (0.004in thick, Alfa Aesar) and drying at 60°C for 12h in convection oven. The resulting slurry-coated aluminum was roll-pressed and the electrode reduced to required dimensions with a punching machine.

2.4.2 Materials characterization

Interactions between TMS-PDTA, IM-Cl, and lithium polysulfides were characterized using Fourier Transform Infrared Spectroscopy. A Bruker Optics Vertex80v Infrared Spectrometer with air-sensitive samples tested in a vacuum-evacuated chamber. Inductively coupled plasma atomic emission spectroscopy (ICP-AES) was used to quantify sulfur content in the electrolytes as a function of time. To quantify the content of lithium and sulfur in the electrolyte, the peak intensity count values of Li and S obtained from the ICP-AES raw data (elemental counts versus wavelength) is used in concert with the respective calibration curves (**Figure S2.5**) to determine the respective elemental concentrations. All measurements were performed on 10 ml aliquots of the electrolyte collected every 10 mins. Morphologies of the composite cathode materials were studied using FEI Tecnai G2 T12 Spirit Transmission Electron Microscope (120kV) and elemental mapping (EDX and EELS) was performed using FEI Tecnai F20 Transmission Electron Microscope (200kV). Impedance was measured against frequency using a Novocontrol N40 broadband dielectric spectroscopy.

2.4.3 Electrochemical characterization

2030 coin-type cells were assembled using lithium metal (0.03in thick, Alfa Aesar) as the anode electrode, a microporous polyethylene material, Celgard 2500 polypropylene membranes as separator, carbon-composite sulfur cathodes containing well-defined amounts of IM-Cl and TMS-PDTA, and 40 μ L 0.1M lithium bis(trifluoromethanesulfone) imide (LiTFSI) and 0.2M LiNO₃ in DOL(1,3-dioxolane): DME (1,2-dimethoxyethane) (v:v=1:1) for each cell. Cell assembly was carried out in an argon-filled glove-box (MBraun Labmaster). The room-temperature cycling characteristics of the cells were evaluated under galvanostatic conditions

using Neware CT-3008 battery testers and electrochemical processes in the cells were studied by cyclic voltammetry using a CHI600D potentiostat.

2.5 Conclusion

In summary, we have developed a novel class of molecular sorbents for sulfur cathodes, which take advantage of strong lithium-nitrogen and lithium-chlorine interactions to sequester lithium polysulfides in the cathode. By designing the sorbent species with anchoring groups that can cross-link within the cathode and bind to the surface of carbon we show that tethered sorbents based on amines and imidazolium chloride molecules present strong barriers to long-chain lithium polysulfide (Li_2S_x , $x > 2$) dissolution and loss to tetraglyme, a well-known excellent solvent for long-chain Li_2S_x . Through density-functional calculations, we further show that the Li_2S_x entrapment is of thermodynamic origin and persists via strong lithium-electrophile interactions that in the case of imidazolium-containing additives can be a factor of two higher than other species. Application of the concept to lithium batteries leads to cells with potential profiles that are not noticeably changed during their first discharge cycles, relative to a sulfur-carbon composite cathode without the molecular sorbents, but which upon galvanostatic cycling display remarkable improvements in stability at both low and high discharge/charge rates. As an illustration of the effectiveness of the tethered sorbents, it is found that as little as 2w% of a nitrile-rich molecular species can increase the storage capacity of the sulfur cathode from effectively 100 to at least 700 mAh/g after 100 charge/discharge cycles at a rate of 1C. Our approach circumvents the need to apply coatings to the carbon or for thermal infusion of the sulfur into a porous carbon host. Preliminary thermodynamic analysis suggest that the method can be used with oxygen-, chlorine-, fluorine-, and phosphorous-rich molecules, and we expect

future reports will elaborate on the relative effectiveness of additives species based on each of these molecules for preventing polysulfide loss in lithium-sulfur, as well as other metal- (e.g. Na, Mg, and Al) sulfur secondary batteries.

Acknowledgements

The material is based on work supported as part of the Energy Materials Center at Cornell, an Energy Frontier Research Center funded by the U.S. Department of Energy, Office of Science, Office of Basic Energy Sciences under Award Number DESC0001086. We also acknowledge the National Science Foundation, Partnerships for Innovation Program (Grant#IIP-1237622) for partial support for the study. This work made use of the electron microscopy facility at the Cornell Center for Materials Research (CCMR), an NSF supported MRSEC through Grant DMR-1120296.

References

1. P. G. Bruce, *Solid State Ion.* 2008, 179, 752-760.
2. Z. C. Yang, J. C. Guo, S. K. Das, Y. C. Yu, Z. H. Zhou, H. D. Abruna, L. A. Archer, *J. Mater. Chem.* 2013, 1, 1433-1440.
3. V. S. Kolosnitsyn, E. V. Karaseva, *Russ J. Electrochem.* 2010, 44, 506-509.
4. J. Hassoun, B. Scrosati, *Angew. Chem.* 2010, 122, 2421-2424.
5. J. Hassoun, B. Scrosati, *Adv. Mater.* 2010, 22, 5198-5201.
6. Y. V. Mikhaylik, J. R. Akridge, *J. Electrochem. Soc.* 2004, 151, A1969-A1976.
7. D. Aurbach, E. Pollak, R. Elazari, G. Salitra, C. S. Kelley, J. Affinito, *J. Electrochem. Soc.* 2009, 156, A694-A702.
8. J. H. Shin, E. J. Cairns, *J. Electrochem. Soc.* 2008, 155, A368-A373.
9. J. L. Wang, J. Yang, J. Y. Xie, N. X. Xu, *Adv. Mater.* 2002, 14, 963-965.
10. L. F. Xiao, Y. L. Cao, J. Xiao, B. Schwenzer, M. H. Engelhard, L. V. Saraf, Z. M. Nie, G. J. Exarhos, J. Liu, *Adv. Mater.* 2012, 24, 1176-1181.
11. X. L. Ji, K. T. Lee, L. F. Nazar, *Nat. Mater.* 2009, 8, 500-506.
12. C. Liang, N. J. Dudney, J. Y. Howe, *Chem. Mater.* 2009, 21, 4724-4730.
13. X. Ji, S. Evers, R. Black, L. F. Nazar, *Nat. Comm.* 2011, 2, 325.
14. B. Zhang, X. Qin, G. R. Li, X. P. Gao, *Energy Environ. Sci.* 2010, 3, 1531-1537.
15. C. Zhang, H. Wu, C. Yuan, Z. Guo, X. W. Lou, *Angew. Chem, Int. Ed.* 2012, 51, 9592-9595.
16. N. Jayaprakash, J. Shen, S. S. Moganty, A. Corona, L. A. Archer, *Angew. Chem. Int. Ed.* 2011, 50, 5904-5908.
17. S. Thieme, J. Bruckner, I. Bauer, M. Oschatz, L. Borchardt, H. Althues, S. Kaskel, *J. Mater. Chem.* 2013, 32, 9225-9234.
18. J. Bruckner, S. Thieme, F. Böttger-Hiller, H. T. Grossmann, P. Strubel, H. Althues, S. Spange, S. Kaskel, *Adv. Funct. Mater.* 2013, 24, 1284-1289.

19. J. Guo, Y. Xu, C. Wang, *Nano Lett.* 2011, 11, 4288-4294.
20. G. Zheng, Y. Yang, J.J. Cha, S. S. Hong, Y. Cui, *Nano Lett.* 2011, 11, 4462-4467.
21. L. Ji, M. Rao, L. Zheng, Y. Li, W. Duan, J. Guo, E. J. Cairns, Y. Zhang, *J. Am. Chem. Soc.* 2011, 133, 18522-18525.
22. H. Wang, Y. Yang, Y. Liang, J. T. Robinson, Y. Li, A. Jackson, Y. Cui, H. Dai, *Nano Lett.* 2011, 11, 2644-2647.
23. J. Guo, Z. C. Yang, Y. Yu, H.D. Abruna, Archer, L.A. *J. Am. Chem. Soc.* 2013, 135, 763-767.
24. M. J. Frisch, G. W. Trucks, H. B. Schlegel, G. E. Scuseria, M. A. Robb, et al, *Gaussian 09*, revision A.1, Gaussian, Inc., Wallingford, CT, 2009.
25. W. Z. She, Q. Zhang, W. Li, G. Zheng, H. Yao, Y. Cui, *Chem. Sci.* 2013, 4, 3673-3677.
26. Takashi. Y, Kazuhisa S, Masatoshi A, Kuo-Hsiang. C, Jenn-huei. L, Norman. L. A, J. *Comput. Chem.* 2003, 3, 319.
27. Stephen. T, R. A. O, *Norg. Chem.* 1984, 23, 4352-4360.
28. Zhaofeng. D, Zhian. Z, Yanqing. L, Jin. L, Jie. Li, Yexiang. L, *J. Electrochem. Soc.* 2013, 160, A553-A558.
29. Y. Lu, S.S. Moganty, J. L. Schaefer, L. A. Archer, *J. Mater. Chem.* 2012, 22, 4066-4072.
30. R. D. Rauh, K. M. Abraham, C. F. Pearson, J. K. Surprenant, S. B. Brummer, *J. Electrochem. Soc.* 1979, 126, 523-527.
31. R. D. Ruah, F. S. Shker, J.M. Marston, S. B. Brummer, *J. Inorg, Nuclear Chem.* 1977, 39, 1761-1766.
32. Y. Kambe, A. J. Fernandes, L. A. Archer, *Mater. Res. Soc. Symp. Proc.* 2013, 1541

Appendix

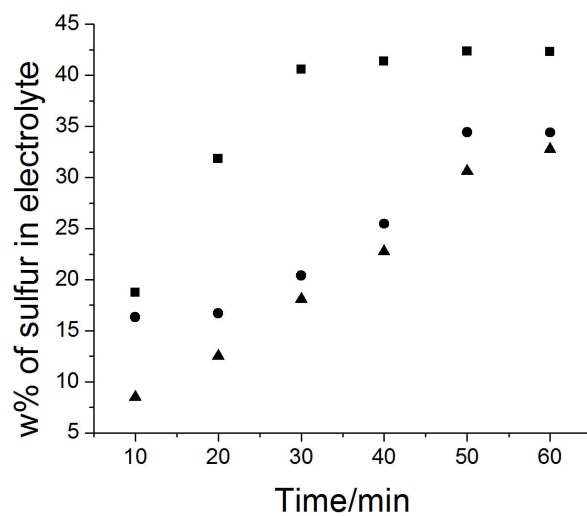


Figure S2.1 Sulfur content in three different cases when Lithium Polysulfide is Li_2S_9 (squares represent the case of no sorbent; circles with TMS-PDTA; triangles with IM-Cl)

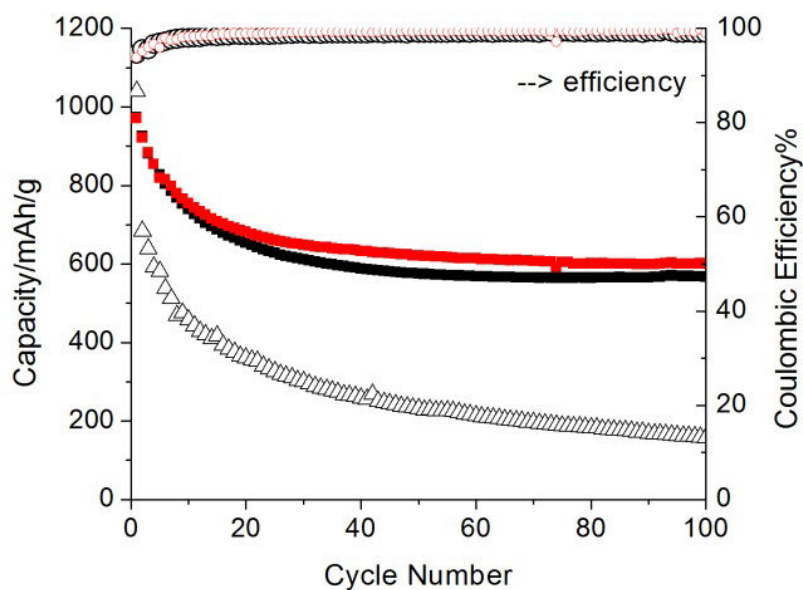


Figure S2.2 Long-term cycling performance of Li-S batteries without additives (black triangle), with TMS-PDTA (black square) and the corresponding Coulombic efficiency represented as black cycle, with IM-Cl (red square) and the corresponding Coulombic efficiency represented as red cycle at 1C.

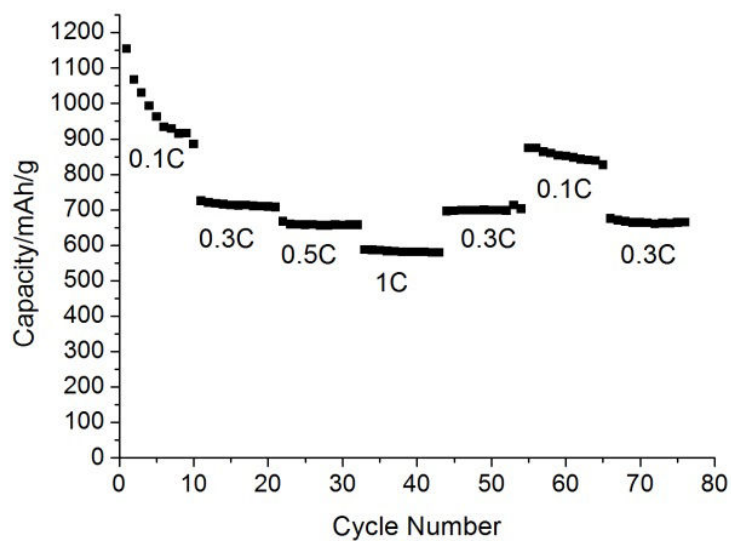


Figure S2.3 Capacity versus cycle number in a step rate Galvanostatic cycling experiment for Li-S cells containing 6w% TMS-PDTA sorbent in the catode.

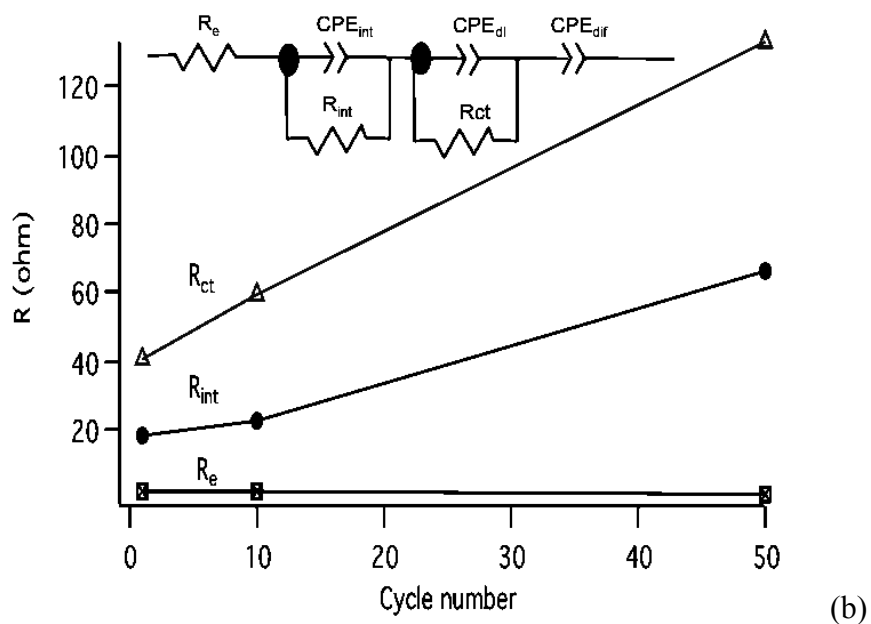
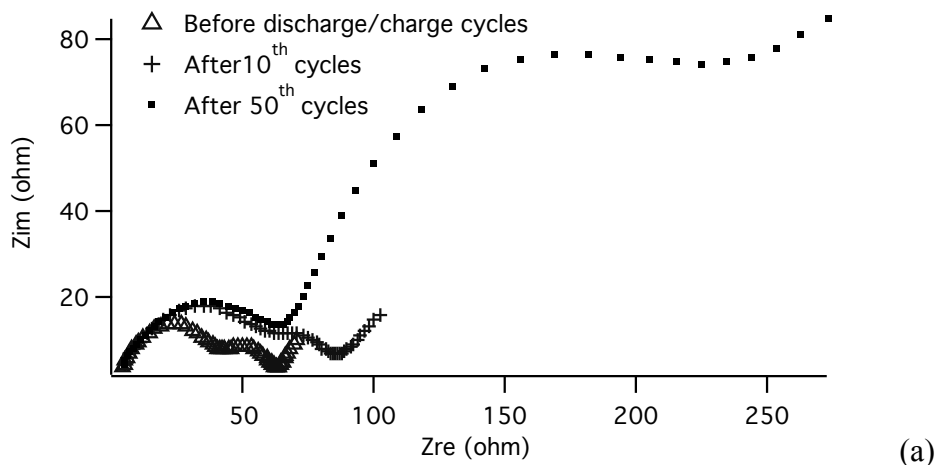


Figure S2.4 (a) Nyquist plots of Li-S cell with TMS-PDTA before discharge/charge cycles and after 10 and 50 cycles. Nyquist plots are analyzed by Zview software. (b) Plots of electrolyte resistance (R_e), interphase contact resistance (R_{int}) and charge-transfer resistance (R_{ct}) as a function of cycle number, with the equivalent circuit for lithium/sulfur cell shown in inset.

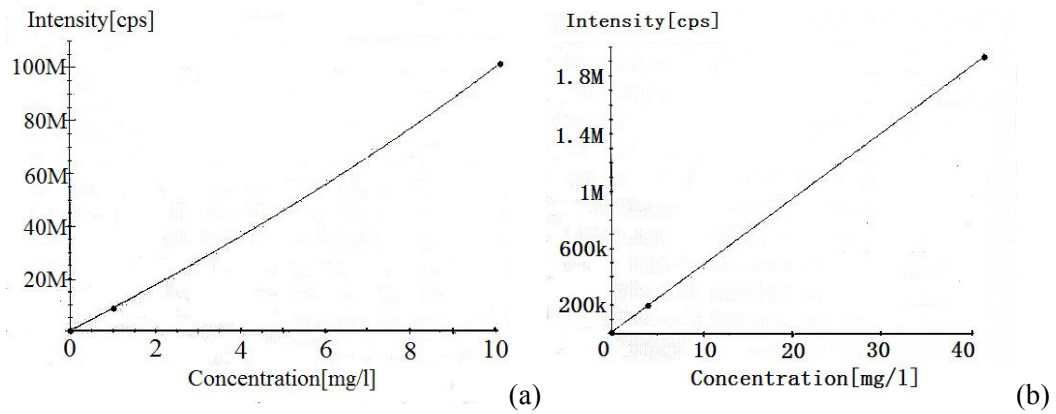


Figure S2.5 ICP-AES Calibration curves for estimating concentration of (a) Lithium and (b) sulfur from measured peak intensity

CHAPTER 3

Enhanced Li-S batteries using Amine-functionalized carbon nanobutes in the Cathode

Adapted with permission from

L. Ma, H. L. Zhuang, S. Wei, K. E. Hendrickson, M. Kim, G. Cohn, R. G. Hennig, L. A. Archer,

Enhanced Li-S batteries using Amine-functionalized CNT in the Cathode, ACS Nano 2016,

10,1050-1059

3.1 Abstract

The rechargeable Lithium-Sulfur (Li-S) battery is an attractive platform for high-energy, low-cost electrochemical energy storage. However, practical Li-S cells are limited by several fundamental issues, such as the low conductivity of sulfur species and the dissolution of long-chain lithium polysulfides (LiPS) into the electrolyte. We report on an approach that allows high-performance sulfur-carbon cathodes to be designed and synthesized, in which polyethylenimine (PEI) polymers bearing a large amount of amine groups in every molecular unit are attached to the cathode by reaction with hydroxyl and carboxyl functionalized carbon nanotubes. Significantly, for the first time we carried out direct dissolution kinetics measurements and showed that the incorporation of the hybrids in the sulfur cathode produces a factor of three or more reduction in both the dissolution rate and equilibrium concentration of LiPS in the electrolyte. The composite shows high capacity at both low and high current rates with extremely stable performance – capacity retention rate of 96% is obtained at 0.5C. The observed excellent electrochemical performance can be attributed to the specific and strong interaction between sulfur species and the amine groups, interconnected conductive carbon nanotube substrate, and the combination of physical barrier and thermal sequestering for LiPS provided by the CNT-PEI

composite.

3.2 Introduction

The rechargeable Lithium-Sulfur (Li-S) battery is under active consideration by research teams worldwide as an attractive platform for high-energy, low-cost electrochemical energy.^{1, 2} The low cost of sulfur (\$0.02/g) and the high theoretical energy density (2500 Wh/kg or 2800 Wh/L) of the sulfur cathode are widely regarded as the main drivers for this interest.³⁻⁵ Realization of this promise in a practical Li-S cell has so far been elusive because the electrode kinetics, active material utilization, and lifetime of the cell are limited by several fundamental issues, which derive from the complex solid-state and solution physical chemistry of the electrodes and electrolyte.^{6, 7} The poor ionic and electronic conductivity of sulfur and its reduction compounds with lithium leads to sluggish electrode kinetics, poor active material utilization, and unacceptable overall cell performance at moderate charge/discharge rates. Dissolution of long-chain lithium polysulfides (Li_2S_x , $2 < x < 8$) (LiPS) into the electrolyte and the shuttling of polysulfides between cathode and anode consume the active material in a parasitic process that ultimately ends in premature cell failure.^{8, 9} Great efforts have been applied to enhance the electronic conductivity and prevent the dissolution of LiPS, the most effective of which focus on synergetic benefits of nanoengineered carbons, including micro/meso porous carbon,^{10, 11} carbon nanotubes/nanofibers,^{12, 13} graphene/graphene oxide sheets,^{14, 15} and carbon nanospheres,^{16, 17} to simultaneously facilitate electron transport and to sequester soluble species in the cathode.

Among nanoengineered carbons, Carbon Nanotubes (CNTs) are emerging as among the most effective and practical choices as conductivity aids in a battery cathode. In the specific case of the Li-S cell, CNTs offer at least four specific features that justify this interest: (i) CNT have

high aspect ratios, high surface area, and large surface to volume ratios. This means that their percolation threshold is low and that diffusion lengths for both lithium ions and electrons are low. The materials can therefore be thought to provide an ideally, interconnected conductive scaffold to accommodate sulfur and its poorly conductive reduction products in the cathode;^{18, 19} (ii) The CNT microstructure may also be beneficial for kinetically trapping long-chain LiPS in the cathode, which without compromising interfacial contact between the active materials and electrolyte, limits LiPS dissolution and loss to the electrolyte;^{20, 21} (iii) At CNT concentrations above the percolation threshold, it creates a mechanically strong scaffold in the cathode. Integration of a polymer binder and sulfur creates a mechanically robust electrode, able to accommodate periodic volume expansion and contraction of sulfur that accompanies its redox reaction with lithium;^{12, 19} (iv) With worldwide efforts focused on economical processes for large-scale and cost-effective manufacture of CNTs, a variety of CNTs is now available at modest prices of 0.10-25 \$/g. It is predicted that this cost could drop to as little as 10-30 \$/kg within next ten years, when production capacity is expected to reach hundreds of thousand of tons annually.²²

The barriers CNTs and other carbon-based nanomaterials present to dissolution of LiPS are now understood to be kinetic; a soluble LiPS species physically trapped by the host material will eventually leach into the electrolyte. It is possible to augment interactions between cathode components and LiPS by using polar additives or metal oxides such as SiO_2 ,²³ TiO_2 ,²⁴ and Al_2O_3 .²⁵ The strong affinity between LiPS and nitrile or chlorine containing molecules has recently been confirmed both by density functional theory and diffusion experiments.²⁶ Oxides, such are also applied to serve as polysulfide reservoirs to hinder the dissolution of sulfur species. Polymer coatings have already been used as an additional physical barrier to hinder LiPS

dissolution, however these barriers are insufficient for at least two reasons. First, they only reduce the kinetics of LiPS loss to the electrolyte, which makes their effect temporary. Second, the conductivity of the electrode is decreased as a result of the insulating polymers typically employed.^{21, 27} Another approach is to modify the carbon surface with amphiphilic polymers to improve the interaction. Polyvinyl pyrrolidone (PVP), for example, has been employed in this manner as a coating onto carbon surface via non-polar physical adsorption.²⁸ However the modification is just a physical wrapping/coating of the carbon/sulfur particles, thus the effect will fade with time when there is no bonding between those polymers and the carbon substrate. A big disadvantage of all these methods is that the polar additives or oxides, or the polymer coatings are insulators, which will lower the conductivity of the electrode, resulting in limited utilization of the active materials.

Here we report an approach that allows high-performance sulfur-carbon composite cathodes to be designed and synthesized. Specifically, hybrid particles comprised of multiwall carbon nanotubes (CNTs) covalently grafted with polyethylenimine (PEI) polymers, bearing a large amount of amine groups in every molecular unit, are created via a grafting-to reaction using hydroxyl and carboxyl groups on the CNTs. The hybrid particles are shown to form effective anchors for LiPS in the Li-S battery cathode. Covalent attachment of PEI to CNT is confirmed by XPS and Raman spectroscopy. In addition, the strong affinity of LiPS to PEI-functionalized CNT is verified by density-functional theory (DFT) calculations, which yield a substantial binding energy of 1.24 eV. Significantly, we show via direct dissolution kinetics measurements that incorporation of the hybrids in the sulfur cathode produces a factor of three or more reduction in the dissolution rate and equilibrium concentration of LiPS in the electrolyte. These features together with other intrinsic merits of CNTs, such as effective physical trapping for

LiPS,¹⁹⁻²¹ good conductivity and robust mechanical properties, are shown to yield CNT-PEI/sulfur composite cathodes that exhibit excellent electrochemical properties, including stable cycling performance at rates up to 3.35 mA/cm² or 2C. An advantage of our materials design is that we are able create strong and multidentate interactions with LiPS and elemental sulfur throughout the cathode. It means that the content of PEI need not be large, for the present study it never exceeded 8%, compared with~20% in typical coating studies.^{21, 27} A second advantage comes from the fact that the PEI is covalently bonded to the cathode substrate, through strong, but sparse amide linkages. This means that the electrode architecture is preserved under the mechanical and chemical stresses that accompany extended cycling. The sparse covalent attachment of PEI is also beneficial as it allows the high electrical conductivity of the electrode to be preserved.

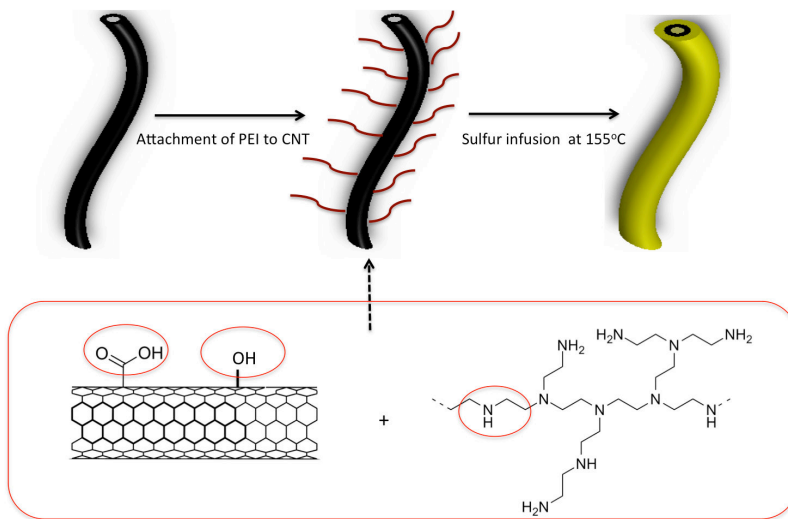


Figure 3.1 Procedure of preparation of CNT-PEIS composite.

3.3 Results and discussion

Figure 3.1 illustrates the two-step preparation procedure of the CNT-PEI/Sulfur composite: First, PEI is covalently attached to the CNTs via a reaction with the hydroxyl and carboxyl functional groups on the CNTs. The reaction product is vigorously washed with water to remove any excess PEI, which is highly soluble in water, and dried in preparation for the next step. In the second step, sulfur is loaded to the composite by liquid infusion and annealing at 155°C, the temperature at which liquid sulfur has its lowest viscosity.²⁹ Multiple analytical tools were used to verify the covalent attachment of PEI to the CNTs and to characterize the interaction between PEI and the discharge products in the sulfur cathode. The XPS survey scanning spectra are presented in **Figures 3.2a** and **3.2b**). It is apparent that before reaction with PEI, there is only a signal from C 1s (285 eV) and O 1s (532 eV), which arises from the hydroxyl and carboxyl groups on the CNTs. After reaction with PEI and washing to remove the untethered PEI, there is an additional N 1s signal (400 eV); providing evidence that the PEI is bonded to the CNT substrate. Deconvolution of the N 1s signal reveals peaks for both amine (399.3 eV) and amide (401.8 eV) groups, implying that bonding between PEI and carboxylic acid groups on the particles has occurred and that even after attachment to CNT, amine groups remain available for interaction with LIPS. Besides the N signal, the C 1s signal is also altered after reacting PEI and CNTs (**Figure 3.2d**). Before the PEI treatment, the C 1s spectrum shows the C-O hydroxyl bonding at 286.1eV and O-C=O carboxyl bonding at 288.8eV (**Figure 3.2e**).^{30, 31} After the reaction with PEI, signals associated with the C-N amine bond at 285.6 and -N-C=O bonding at 287.9 eV appear.³² ³³ Furthermore, the hydroxyl and carboxyl bonding signal disappear, indicating the nearly complete conversion of hydroxyl and carboxyl groups (**Figure 3.2f**).

Density Functional Theoretical (DFT) analysis was used to quantify the strength of the interactions between PEI and LiPS. The Gaussian09 program using the PBE exchange-correlation functional and cc-pVDZ basis sets was used for this analysis. The optimized atomic configuration of LiPS and PEI is illustrated in **Figure 3.3a**. This analysis also reveals a high binding energy of 1.24 eV, which is significantly higher than the binding energy (0.34 eV) between LiPS and graphene;²⁸ it is also higher than that of 0.83 eV, between LiPS and PVDF,³⁴ a common binder for the sulfur cathode. The DFT analysis can be used to calculate the IR spectra of PEI and for LiPS/PEI mixtures. **Figure 3.3b** compares the calculated spectra for pure PEI and a LiPS/PEI mixture. An additional infrared peak at 640 cm^{-1} in the mixture of PEI and LiPS is apparent. The analysis further shows that this peak results from the formation of N-Li bonds in the mixtures.³⁵ Experimental FTIR spectra for pure PEI and mixture of LiPS and PEI are reported in **Figures 3.3c** and **3.3d**, respectively. A distinct, but weak peak appears at around 650 cm^{-1} in the spectrum for LiPS/PEI, but is not seen in pure PEI. We view this as confirmation of the DFT result and supportive of the formation of Li-N bonds in the composites. Further, the peak at around 3200 cm^{-1} corresponding to the N-H stretching mode shifts to a lower number in the mixture compared to pure PEI. More importantly, this shift is not observed for any of the other vibration modes, such as the one associated with the CH_2 bend at 1455 cm^{-1} (**Figure 3.3d**).

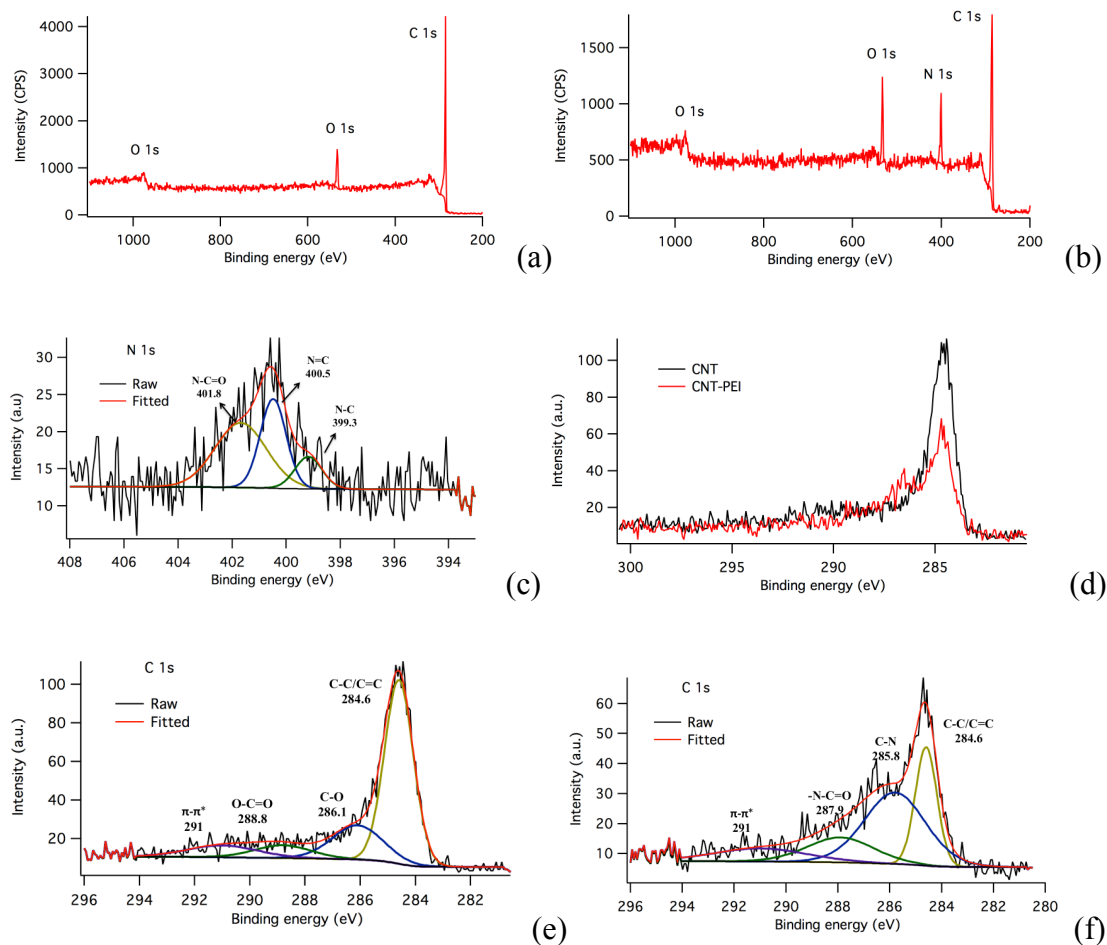


Figure 3.2 XPS survey scanning spectra for: (a) unmodified CNTs; and (b) PEI modified CNTs. (c) High-resolution N 1s spectrum of PEI modified CNTs. (d) Comparison of the C 1s signal of CNTs before and after attachment of PEI. (e) High-resolution C 1s XPS spectrum of unmodified CNTs. (f) High-resolution C 1s XPS spectrum of PEI modified CNTs. (f) High-resolution C 1s XPS spectrum of PEI modified CNTs.

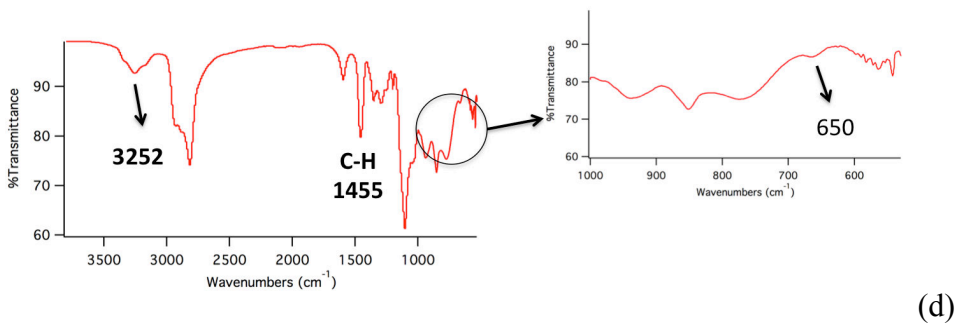
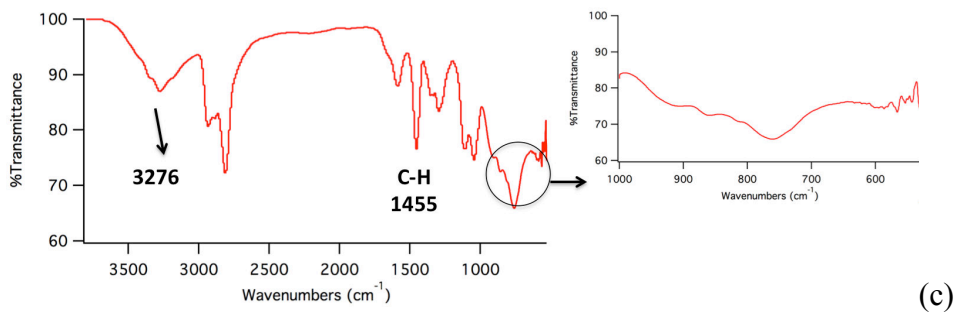
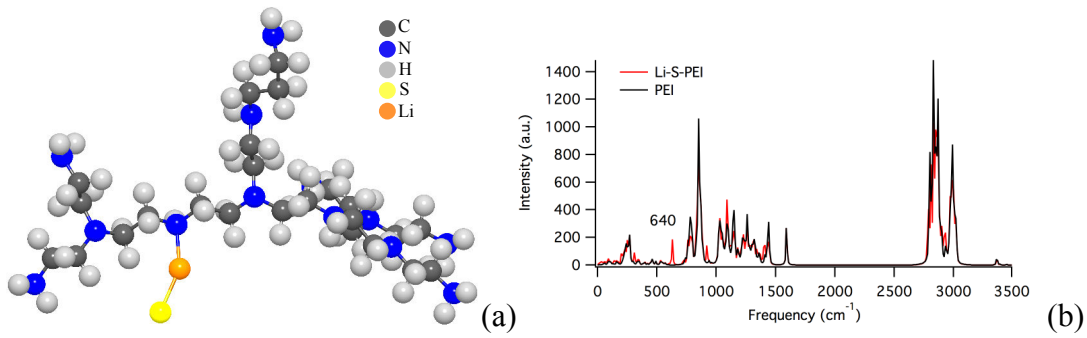


Figure 3.3 (a) Structure of PEI deduced from DFT analysis of the binding energy between PEI and the Li-S⁻ species. (b) DFT calculation of IR spectra of the mixture of Li-S⁻ species and PEI (red) and pure PEI (black). (c) Experimental FTIR spectra of pure PEI. (d) Experimental FTIR spectra of mixture of Li₂S₉ and PEI.

The bonding between the amine groups and the LiPS is also verified by the XPS spectra of the discharge product of the sulfur/PEI-CNT composite cathodes. The Li 1s spectrum (**Figure 3.4a**) shows a Li-N and a Li-S signal, which is in agreement with expectations for formation of a Li-N bond.³⁶ The N 1s spectrum is also changed after discharge, indicating the interaction again in a manner consistent with the presence of strong interactions between LiPS cathode discharge products and amine groups present in the cathode (**Figure 3.4b**).

The XPS S 2p spectrum of the composite shows the successful loading of sulfur onto the CNTs (**Figure 3.4c**). The S 2p signal can be deconvoluted into an S 2p_{3/2} and 2p_{1/2} doublet at 163.8 and 165 eV, respectively, with the expected energy separation of 1.2 eV and intensity ratio of 2:1.³⁷³⁸ The binding energy of the S 2p_{3/2} peak is slightly lower than the literature value, and this happens after the calibration of C-C peak to 284.6 eV, implying that elemental sulfur interacts with the composite. In the S 2p signal after discharge, lithium sulfide peaks are observed between 161.5-162.7 eV,^{36, 39} indicating the full discharge of elemental sulfur. There is also a sulfate signal, which is thought to result from the air and moisture sensitivity of Li₂S. To probe the interaction between the amine group on PEI and sulfur upon sulfur loading, a high-resolution scan of the N spectrum before and after sulfur loading was performed. The results reported in **Figures 3.4d** and **3.4e** show that the area of the peak corresponding to the amine group decreases, strongly indicative of a chemical reaction at the amine group. Previous studies have reported that sulfur mixed with amine-containing organic molecules results in the formation of compounds with sulfur-amine bonds.³⁹⁻⁴¹ The amine group donates an electron to elemental sulfur, leading to a decrease of amine group content detected by XPS. This reaction also explains why the sulfur peaks shift to lower binding energy—the electron donation from the amine groups enhances the electric field, reducing the energy for the S 2p electron to be knocked out by the x-

rays.

The Raman spectra of the composite also provide information about the interaction between elemental sulfur and the CNT-PEI composite (**Figure 3.5** and **Table 3.1**). The intensity ratio between the D band (I_D) and the G band (I_G) is indicative of a basic structural change in the CNTs, with a greater value of this parameter implying more defects.^{42, 43} Upon sulfur loading onto the CNT composite, an increase in the I_D/I_G ratio is observed, indicating an increase of sp^3 carbons on the nanotubes, which imply that sulfur interrupts the $C=C$ sp^2 bond in CNT. Thus both XPS and Raman spectra verified that sulfur is anchored to the composite via strong chemical interaction.

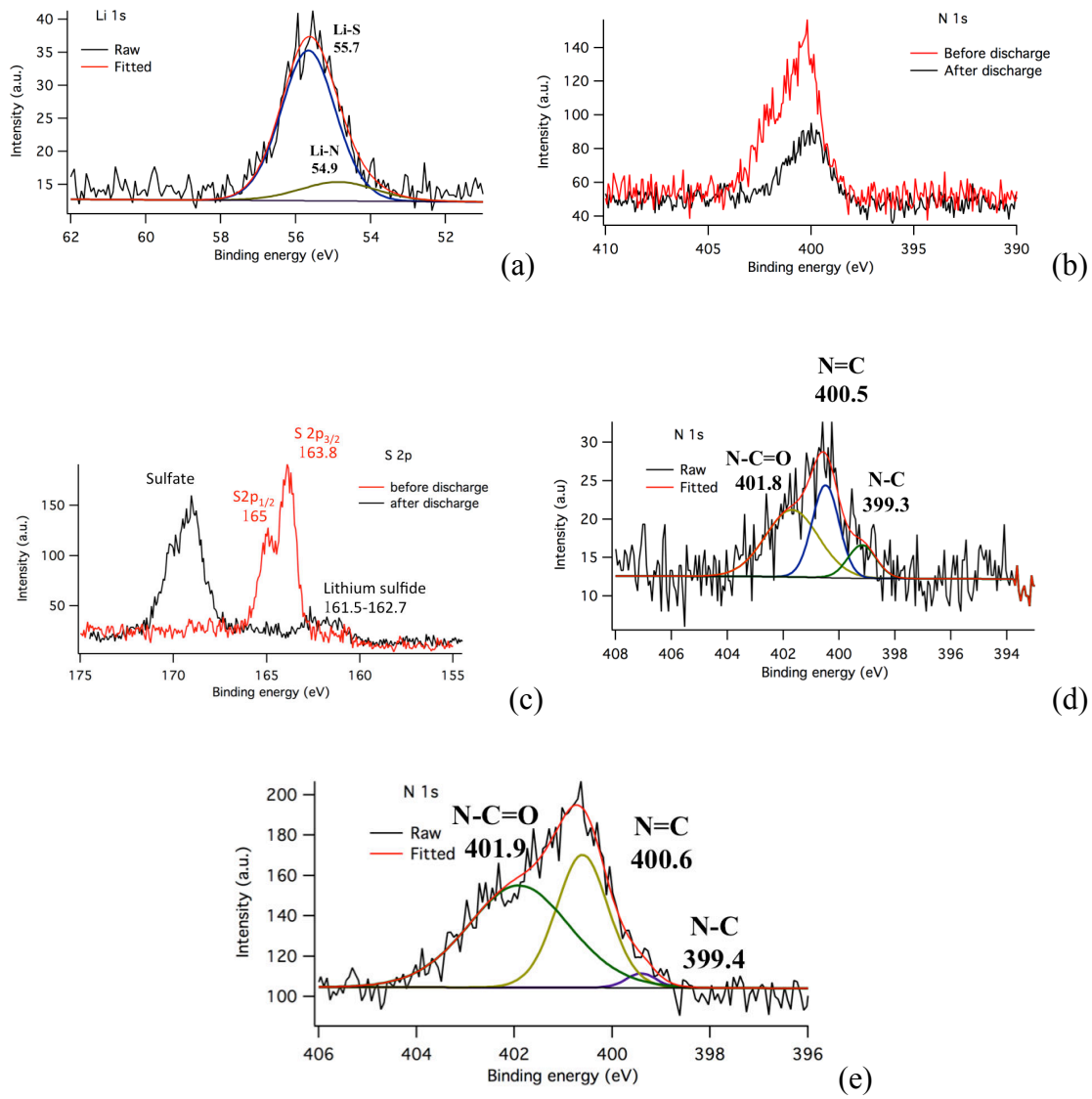


Figure 3.4 High resolution XPS spectra for: (a) Li 1s of discharge product of CNT-PEIS composite; (b) N 1s before and after discharge; (c) S 2p before and after discharge; (d) N 1s of CNT-PEI composite before sulfur loading; and (e) N 1s of sulfur loaded CNT-PEI composite.

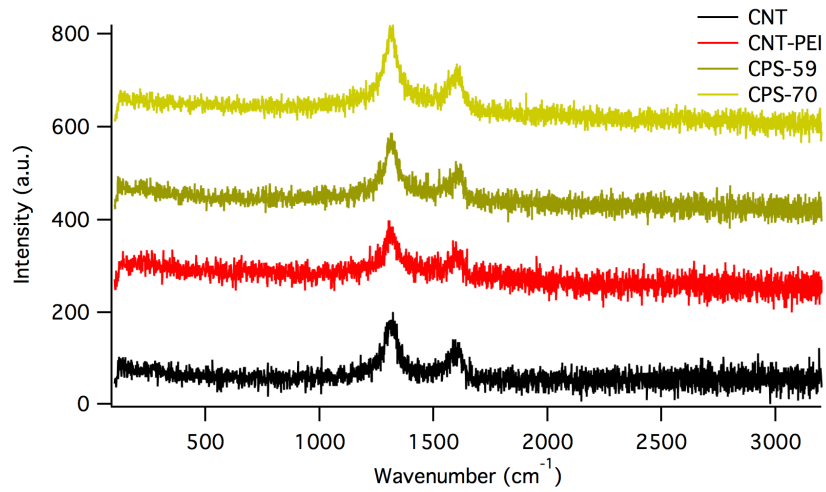


Figure 3.5 Raman spectra of CNT, CNT-PEI and sulfur loaded CNT-PEI composite.

Table 3.1 I_D/I_G ratio in different composites.

	I_D/I_G
CNT	1.94
CNT-PEI	2.02
CPS-59	2.34
CPS-70	2.47

Two CNT-PEI/S composites, CPS-59 and CPS-70, with different sulfur content (59 wt.% and 70 wt% respectively) were prepared, and the sulfur content determined using TGA (**Figure S3.1**) as described in Supporting Information section. Table S1 summarizes the surface area and pore size information derived from Brunauer-Emmett-Teller (BET) analysis. Upon sulfur loading, with the infusion of the sulfur in the microstructure provided by CNT network, the pore volume and pore size of the composite decrease, and the effect is even more dramatic when higher sulfur content is loaded. These results indicate that the sulfur is filled in the microstructure of CNT, but still allowing electrolyte access to the active materials by the presence of residual micropores. XRD analysis of CNT-PEI and CNT-PEI/S composites (**Figure 3.6**) was used to probe the crystal structure of the materials. The attachment of PEI onto CNT clearly does not affect the carbon structure; but the sulfur spectrum is affected by sulfur loading in the composites. At 59w% sulfur, only a weak sulfur peak is observed, which implies that sulfur is mostly amorphous. In contrast, at 70w% sulfur, there is a strong peak associated with crystalline sulfur. The loss of crystallinity of sulfur in the composites at the lower sulfur loading can be interpreted in terms of the confinement of sulfur in the cathode associated with its interactions with the CNT-tethered PEI. At the higher sulfur loading, we believe that all of the sulfur is not anchored to PEI and as such is freer to adopt crystalline structures typical of the equilibrated material. This interpretation is consistent with the observation of a sulfur loss process at elevated temperature in TGA experiments using composites with 59 wt.% sulfur. **Figure S3.2** compares the impedance of Li-S cells using cathodes comprised of physical mixture of carbon black and sulfur (70 wt%), CNTS-60, CPS-59 and CPS-70. The impedance is observed to decrease dramatically for all of the CNT-based materials. Also, at the same sulfur loading, the impedance of CNT-PEI/S composite is comparable or even smaller than that of CNT-60, implying that the attachment of PEI not only

maintained the high conductivity of CNT matrix, but also improved it to some extent; perhaps because the oxygen containing functional groups on CNT are replaced. In contrast, in previous studies employing polymer coatings in sulfur cathodes,^{21, 27} the insulating polymer adsorbs indiscriminately on the conductive surfaces in the electrode, increasing the resistance at the electrolyte/electrode interface, which limits the rate capability of the cathode.

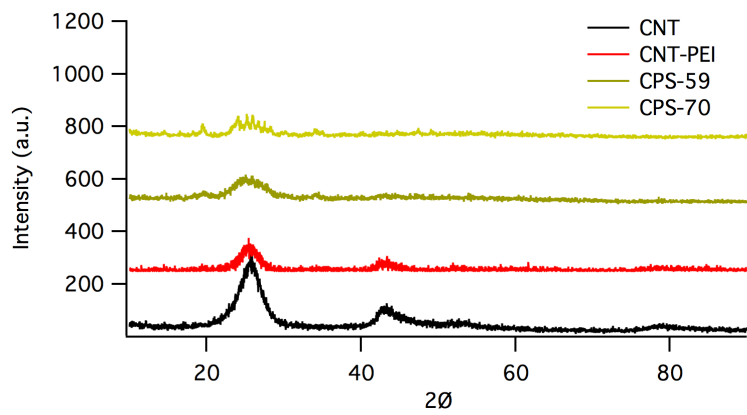


Figure 3.6 XRD analysis of CNT-PEI and CNT-PEI/S composite at different sulfur loadings.

The covalent attachment of PEI onto CNT and affinity of LiPS for PEI-functionalized CNT implies that Li/S battery cathodes based on the materials should exhibit improved performance upon extended electrochemical cycling. **Figure 3.7a** reports results from cyclic voltammetry (CV) of Li/S cells using CPS-70 as cathode, with a scanning rate of 0.1 mV/s. During discharge/charge process, a pair of redox peaks is observed at potentials consistent with the two stages of reduction and oxidation of sulfur. The stable position and intensity of the peaks demonstrate the steady and reversible electrochemical reaction of sulfur in the composite. Similarly, the voltage profile obtained from galvanostatic discharge experiments at 838 mA/g (0.5C, based on the theoretical capacity of sulfur) reported in **Figure 3.7b** shows two strong voltage plateaus over many cycles. The first discharge plateau at ~2.35 V corresponds to the reduction of elemental sulfur into high order LiPS. The second plateau at ~2.0V, is indicative of the reduction of high order LiPS into low order LiPS. **Figure 3.7c** compares the long-term cycling performance of Li-S batteries with three different types of cathodes, CNT-PEI composite with 59 wt% sulfur content (CPS-59), CNT-PEI composite with 70 wt % sulfur content (CPS-70), and unmodified CNT with 60% sulfur content (CNTS-60), but with the same sulfur infusion treatment, cycled galvanostatically at 0.5C. There is very obvious improvement in performance of cathodes based on the CNT-PEI hybrids. The capacity of the unmodified CNT is seen to fade quickly; consistent with loss of active materials from the carbon matrix, while the performance of the sulfur loaded CNT-PEI composite is very stable with high Coulombic efficiency. In conventional Li-S battery, a high initial capacity loss is typically observed due to the dissolution of LiPS. Once in the electrolyte, the LiPS cannot be fully recovered in the following charge process, which leads to poor utilization of the active electrode material and capacity fading.^{21, 26, 43} In lithium-sulfur cells employing CNT-PEI/S composites, it is apparent that very stable

performance is observed, even at 70% sulfur content. These performance improvements evidently stem from PEI's role in effectively preventing LiPS dissolution and the intrinsic improvements in cathode conductivity stemming from the CNT substrate. It is also apparent that the initial capacity Li-S cells employing the CNT-PEI/S composites is slightly lower than typical value;^{23, 26} this result is thought to be due to the need for an activation process over the first few cycles since elemental sulfur is strongly interacting with the composite. Interestingly, CPS-70 exhibits higher electrochemical energy storage capacity than CPS-59, while the cycling performance of CPS-59 is more stable than that of CPS-70. These differences can be explained in terms of differences in the features observed in XRD and TGA analysis of the composites. CPS-70 has higher sulfur content and shows strong crystalline sulfur peaks in XRD, indicating part of the sulfur is not anchored to the CNT, which might be responsible for the capacity fading in CPS-70 since the exposed sulfur will be dissolved into the electrolyte upon sulfur reduction. In contrast, in CPS-59, the sulfur is mostly confined and anchored onto the composite, thus very little capacity fading is observed in the cycling performance. After deep cycling of CPS-70 electrode for as many as 300 cycles at 0.5C, a high capacity of 750 mAh/g can be retained, corresponding to a high capacity retention of $\sim 79\%$ (**Figure 3.7d**). The simultaneous achievement of exceptional cycling stability and nearly 100% Coulombic efficiency over 300 cycles seen in **Figure 3.7d** also provides strong support for the suppression of the shuttling of LiPS in Li-S cells utilizing CNT-PEI/S composite as cathodes.

High rate capability of the CNT-PEIS composite is shown in **Figure 3.7e**, where CPS-70 is cycled at high current rate, such as 1C (1675mA/g) and 2C (3350mA/g) and still has stable performance. The capacity of the cells generally follows the typical trend that at a lower current rate the capacity is higher. The cycling stability of 0.5C is better than 1C and 2C, but it is

comparable at 1C and 2C after the capacity reaches steady state. **Figure 3.7g** shows the excellent rate capabilities of CPS-70 at various current densities, where the capacity of CPS-70 can recover to high values at 0.5C after high current (4C) is applied.

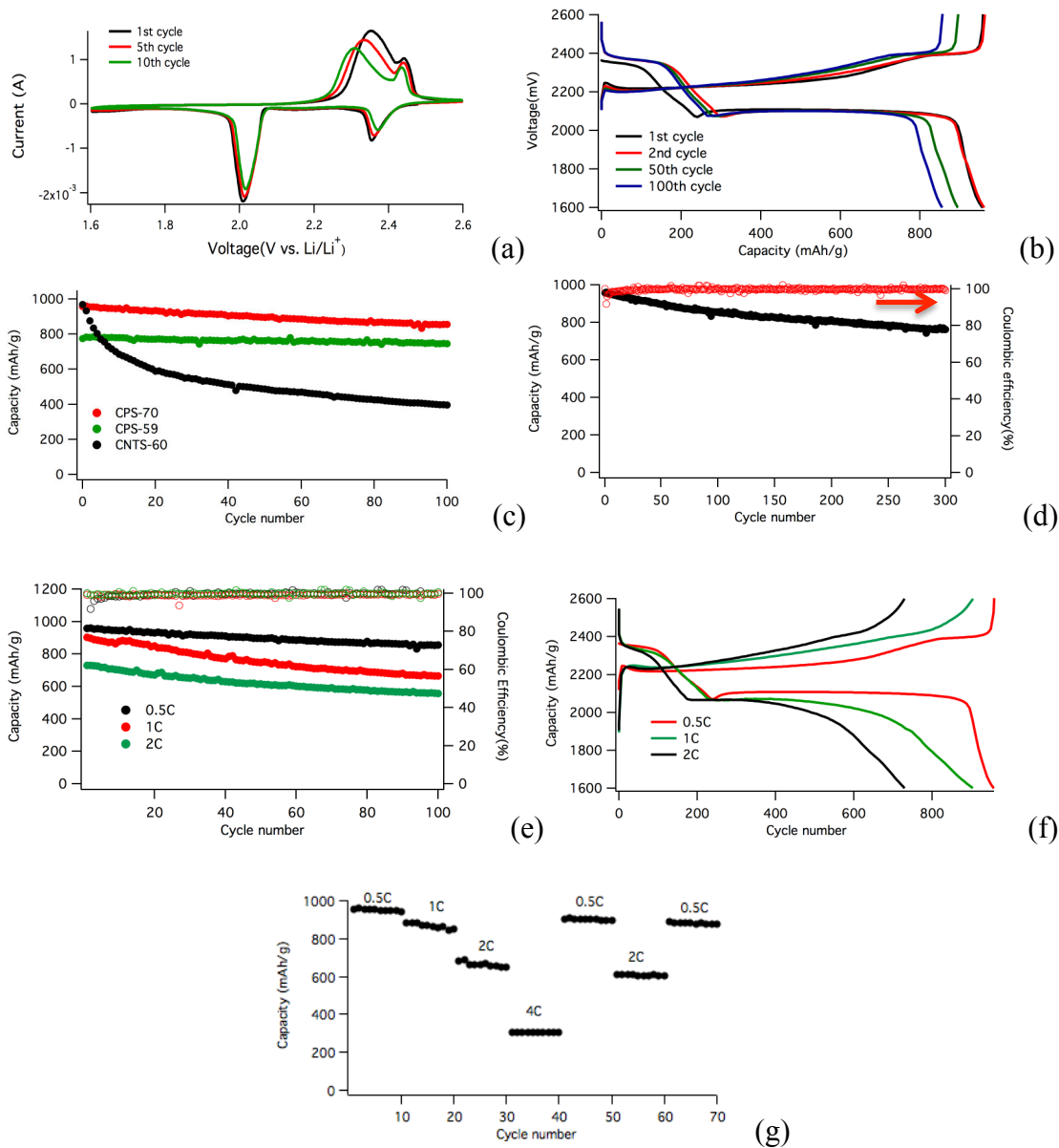


Figure 3.7 (a) Galvanostatic voltage profile for Li-S cell with CPS-70 as cathode at scanning rate of 0.1 mV/s. (b) Voltage vs capacity profile at different cycles for Li-S cell with CPS-70 as cathode cycled at 0.5C (838 mA/g) (c) Long-term cycling performance of Li-S cells with CPS-70, CPS-59 and CNTS-60 as cathodes respectively cycled at 0.5C (838 mA/g) (d) Deep cycling of CPS-70 at 0.5C (838 mA/g) (e) Long-term cycling performance of Li-S cells with CPS-70 cycled at 0.5C (838 mA/g), 1C (1675 mA/g) and 2C (3350 mA/g) respectively, with filled circles representing capacity and blank circles representing Coulombic efficiency. (f) Voltage vs capacity profile for Li-S cell with CPS-70 as cathode cycled at 0.5C (838 mA/g), 1C (1675 mA/g) and 2C (3350 mA/g) respectively. (g) Rate capabilities of CPS-70 at various current densities.

To develop a deeper understanding of the working mechanism of the CNT-PEI/S composites, the morphology of the materials before and after discharge was interrogated using Scanning Electron Microscopy (SEM) (**Figure 3.8**). **Figure 3.8a** and **Figure 3.8b** shows that the attachment of PEI to CNT has no observable effect on the morphology of CNT. In contrast, **Figure 3.8c** and **Figure 3.8d** shows the CNT-PEI/S composite with different sulfur loadings have very different morphologies. In particular, for CPS-70, sulfur particles are observed on the surface of the material, while almost none are seen for CPS-59. This observation explains the difference observed in the XRD spectra and cycling performance between the two materials—only a fraction of the sulfur is anchored to the CNT-PEI hybrids in the cathode. **Figure S3.4** reports the elemental mapping of carbon and sulfur in CPS-59 within the selected area, indicating homogenous distribution of carbon and sulfur in the composite. The morphology of the composite after discharge is reported in **Figure 3.8e-3.8g**, showing that unmodified CNT is coated with large and nonuniform Li_2S particles/layer after discharge, while for the CNT-PEI, the morphology of CNT is still maintained after the discharge. This difference is likely a reflection of the strong affinity between PEI and LiPS, which can help to anchor both the elemental sulfur and the reduction products to prevent their detachment from both the inner and outer surface of the CNT.

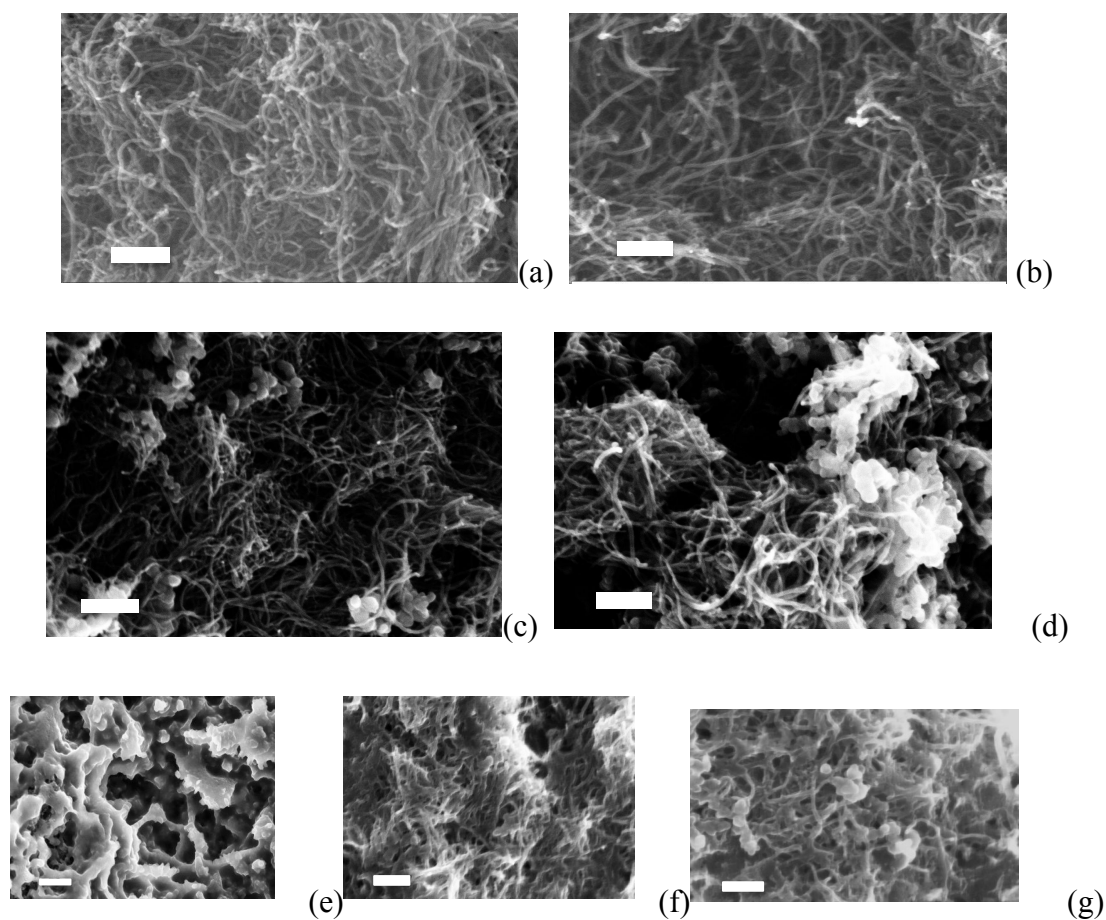


Figure 3.8 SEM images for: (a) Pristine CNT; (b) CNT-PEI hybrid; (c) CPS-59; (d)CPS-70; (e) Li-S cell cathode applying CNT/S-60 after discharge; (f) Li-S cell cathode applying CPS-59 after discharge; (g) Li-S cell cathode applying CPS-70 after discharge. Scale bar = 200nm.

As a final step to understanding the superior electrochemical behaviors of the CNT-PEI/S composite cathodes, we directly evaluate the dissolution kinetics of LiPS trapped in the cathode. Electrode coupons comprised of LiPS composited with the different types of carbon matrices (unmodified CNT and the CNT-PEI composite) were immersed into 10mL tetraglyme, a good solvent for LiPS and a commonly used electrolyte solvent in Li-S cells, and the time-dependent concentration of the solution measured (**Figure S3.5**). The solvent was continuously stirred during the measurements to ensure uniform distribution of sulfur species in the electrolyte; allowing the sulfur concentration at different time to be determined by Inductively coupled plasma atomic emission spectroscopy (ICP-AES) (**Figure S3.6**), performed on small aliquots of the extracted electrolyte. The rate constant k for dissolution can be determined from the time-dependent concentration information, with the help of equations 1-3. Specifically, a straight line plot of $\log_e(1-c/c_s)$ vs time, yields k as the slope. This analysis also yields the equilibrium concentration (c_s) of LiPS in the electrolyte, at which LiPS has equal chemical potential in the electrolyte and cathode. Comparing dissolution rate constants in each case (**Table 3.2**), the CNT-PEI is seen to reduce the rate of dissolution of LiPS by a factor of three or more. Additionally, **Table 3.2** shows similar large reductions in c_s and percentage LiPS loss to the electrolyte at steady state, supporting our hypothesis that the changes are thermodynamic and the anchoring of sulfur to the CNT-PEI support is covalent. It is also apparent that both the solubility and dissolution rates are higher with increasing chain length of LiPS (**Table 3.2**).

$$dc/dt=k(c_s-c) \quad (1)$$

$$c= c_s (1-e^{-kt}) \quad (2)$$

$$-kt = \log_e(1-c/c_s) \quad (3)$$

where k is the rate constant of dissolution, t is time, c is concentration of LiPS dissolved into the electrolyte, and c_s is equilibrium concentration.

3.4 Materials and Method

3.4.1 Preparation of CNT-PEI composite

Multi-walled, carboxylic acid functionalized carbon nanotube (>8% carboxylic acid functionalized, avg. diam.* L =9.5 nm*1.5um)was obtained from Sigma-Aldrich and was dried before use. Polyethylenimine (PEI) solution (50 wt% in water) was obtained from Sigma-Aldrich (average M_w ~750,000 by LS, average M_n ~60,000 by GPC). The CNT-PEI composite was synthesized by heating the mixture of 100 mg CNT suspension (1mg/mL) and 1g PEI solution at 80°C with stirring for 12h. The product was washed with water for 5 times and dried at 100°C overnight.

3.4.2 Preparation of CPS-59, CPS-70 and C-S60

Sulfur incorporation was performed using the vapor phase infusion method. For CPS-59, mixture of sulfur and CNT-PEI composite at a weight ration of 1.5: 1 is balled mill for 20min, after which the mixture was sealed in a glass tube under vacuum. The mixture was heated at 155°C for 6h. CPS-70 was prepared in the same way but with a different ration of sulfur and CNT-PEI at 2.5:1. In the preparation of CS-60, unmodified CNT is used and sulfur: CNT = 1.5:1.

3.4.3 Preparation of Li_2S_4 and Li_2S_9 for FTIR spectra and kinetic study

To synthesize Li_2S_4 , 920 mg Li_2S , 3.2g Sulfur and 0.5 g lithium powder (from FMC Lithium) were added to 5 mL tetraglyme (tetraethylene glycol dimethylether) and stirred for 24h. The

mixture was filtered to obtain a dark reddish liquid. Li_2S_9 was prepared following Rauh et.'s procedure⁴⁴ in a solution process where stoichiometric amounts of elemental sulfur and Li_2S were co-dissolved into tetraglyme, followed by heating at 80°C with stirring for 6h.

3.4.4 Characterization of the composite

Interaction between PEI and LiPS was characterized using FTIR spectroscopy by using a Bruker Optics Vertex80v infrared spectrometer with air-sensitive samples tested in a vacuum-evacuated chamber. Crystal structure was characterized using Scintag Theta-Theta X-ray Diffractometer (XRD). Thermogravimetric analysis (TGA) was used to determine the content of Sulfur in the composite. Raman spectra was done by using Renishaw Invia Confocal Raman microscope. Morphologies of the electrodes were studied using LEO 1550 FESEM (Zeiss SEM) and FEI Tecnai G2 T12 Spirit TEM (120 kV). Impedance was measured versus frequency using a Novocontrol N40 broadband dielectric spectroscopy. X-ray photoelectron spectroscopy (XPS) is used to do elemental analysis and obtain chemical bonding information. Inductively coupled plasma atomic emission spectroscopy (ICP-AES) was used to quantify sulfur content in the electrolytes as a function of time.

3.4.5 Electrochemical Characterization

2030 coin-type cells were assembled using Lithium metal (0.76 mm. thick, Alfa Aesar) as the anode electrode, a microporous material, Celgard 2500, membranes as separator, a cathode with 80% as prepared C/S composite, 10% Super-P Li carbon black from TIMCAL, and 10% poly(vinylidene difluoride) (PVDF, Sigma Aldrich) as binder in an excess of N-methyl-2-pyrrolidone in NMP, and electrolyte of 40uL 1M lithium bis(trifluoromethanesulfone) imide (LiTFSI) and

0.2M LiNO₃ in DOL (1,3-dioxolane) : DME (1,2-dimethoxyethane) (v:v=1:1) for each cell. The sulfur loading per electrode is 1.2mg/cm². Cell assembly was carried out in an argon-filled glove-box (MBraun Labmaster). The room-temperature cycling characteristics of the cells were evaluated under galvanostatic conditions using Neware CT-3008 battery testers and electrochemical processes in the cells were studied by cyclic voltammetry using a CHI600D potentiostat.

3.4.6 Preparation of LiPS electrode for kinetic study

Li₂S₄ and Li₂S₉ were prepared as described above. 30mg LiPS species (10 wt.% in tetraglyme solution), 100mg CNT or CNT/PEI and 20mg Polyvinylidene fluoride (PVDF) was mixed and coated onto Alumina and used for kinetic study before drying under vacuum. Heat was not applied due to the unstable properties of LiPS decomposition into other forms when exposed to air or heat. All of the electrode preparation and sample collection was done in glove box.

3.4.7 Theoretical section

We perform the density-functional theory calculations carried out using the Gaussian09 program using the PBE exchange-correlation functional and the cc-pVDZ basis sets.⁴⁵ Similar to previous studies,^{26, 34} species of lithium polysulfides are modeled by Li-S dimers. All atomic coordinates are fully relaxed until the maximum interatomic forces are less than 4.5×10^{-4} Hartree/Bohr or 0.023 eV/Å. The binding energy E_b between a LiS dimer and PEI is calculated with $E_b = E_{\text{PEI}} + E_{\text{LiS}} - E_{\text{PEI+LiS}}$,

where E_{PEI} denotes the total energy of a pure PEI polymer, E_{LiS} refers to the total energy of the LiS dimer, and $E_{\text{PEI+LiS}}$ is the total energy of the functionalized system.

Table 3.2 Rate constant for dissolution k , percentage of loss of sulfur into the electrolyte, and equilibrium concentration c_s in each case.

	k	Loss of sulfur in the electrolyte (%)	c_s (mg/L)
Li ₂ S ₉ with CNT	$6.22 \cdot 10^{-5}$	78	2300
Li ₂ S ₄ with CNT	$6.1 \cdot 10^{-5}$	39	1172
Li ₂ S ₉ with CNT-PEI	$2.1 \cdot 10^{-5}$	16	481
Li ₂ S ₄ with CNT-PEI	$1.16 \cdot 10^{-5}$	12	350

3.5 Conclusion

In summary, we report on the creation of multiwall carbon nanotube (CNT)- polyethylenimine (PEI) hybrid particles and show by means of spectroscopic analysis that the PEI is covalently linked to the CNT. By means of DFT analysis and spectroscopic measurements we show that the larger number of amine groups each anchored PEI chains introduces to the cathode produce strong, covalent bonding of LiPS in the cathode. Direct measurements of the dissolution kinetics of LiPS/CNT and LIPS/CNT-PEI composites in tetraglyme show that both the dissolution rate and equilibrium concentration of LiPS in the electrolyte are substantially lower for the CNT-PEI materials, indicating that they stabilize the sulfur cathode by a combination of kinetic and thermodynamic means. Application of the materials as cathodes in Li-S batteries shows a direct relationship between anchoring of sulfur in the cathode and cycling performance of the cells.

Acknowledgements

The authors acknowledge support of the National Science Foundation Partnerships for Innovation Program (Grant No. IIP-1237622). This research also used computational resources of the Texas Advanced Computing Center under contracts No. TG-DMR050028N and No. TG-DMR140067. Electron microscopy, X-ray diffraction, X-ray photoelectron spectroscopy facilities and optical spectrometers available through the Cornell Center for Materials Research (CCMR) were used for this work (NSF Grant DMR-1120296).

References

1. L. Ma, K. Hendrikson, S. Wei and L. A. Archer, *Nano Today*, 2015, 10, 315.
2. P. G. Bruce, *Solid State Ion.*, 2008, 179, 752-760.
3. L. Ma, S. Wei, H. L. Zhuang, K. E. Hendrikson, R. G. Hennig, L. A. Archer, *J. Mater. Chem. A* 2015, 3, 19857-19866.
4. S. Wei, L. Ma, K. E. Hendrikson, Z. Tu, L. A. Archer, *J. Am. Chem. Soc.* 2015, 137, 12143-12152.
5. S. Urbonaite, T. Poux and P. Novák, *Adv. Energy Mater.*, 2015, 5, 1500118.
6. S. Evers and L. F. Nazar, *Acc. Chem. Res.*, 2012, 46, 1135-1143.
7. K. E. Hendrickson, L. Ma, G. Cohn, Y. Lu and L. A. Archer, *Adv. Sci.*, 2015, 2, 1500068.
8. A. Manthiram, Y. Fu, S. -H. Chung, C. Zu and Y.-S. Su, *Chem. Rev.*, 2014, 114, 11751-11787.
9. S. Zhang, K. Ueno, K. Dokko and M. Watanabe, *Adv. Energy Mater.*, 2015, 5, 1500117.
10. J. Schuster, G. He, B. Mandlmeier, T. Yim, K. T. Lee, T. Bein and L. F. Nazar, *Angew. Chem. Int. Ed.*, 2012, 51, 3591-3595.
11. G. He, X. Ji and L. Nazar, *Energy Environ. Sci.*, 2011, 4, 2878-2883.
12. G. Zheng, Y. Yang, J. J. Cha, S. S. Hong and Y. Cui, *Nano Lett.*, 2011, 11, 4462-4467.
13. R. Elazari, G. Salitra, A. Garsuch, A. Panchenko and D. Aurbach, *Adv. Mater.*, 2011, 23, 5641-5644.
14. H. Wang, Y. Yang, Y. Liang, J. T. Robinson, Y. Li, A. Jackson, Y. Cui and H. Dai, *Nano Lett.*, 2011, 11, 2644-2647.
15. L. Ji, M. Rao, H. Zheng, L. Zhang, Y. Li, W. Duan, J. Guo, E. J. Cairns and Y. Zhang, *J. Am. Chem. Soc.*, 2011, 133, 18522-18525.
16. N. Jayaprakash, J. Shen, S. S. Moganty, A. Corona and L. A. Archer, *Angew. Chem. Int. Ed.*, 2011, 50, 5904-5908.
17. B. Zhang, X. Qin, G. R. Li and X. P. Gao, *Energy Environ. Sci.*, 2010, 3, 1531.
18. Y.-G. Guo, J.-S. Hu and L.-J. Wan, *Adv. Mater.*, 2008, 20, 2878-2887.

19. X.-B. Cheng, J.-Q. Huang, Q. Zhang, H.-J. Peng, M.-Q. Zhao and F. Wei, *Nano Energy*, 2014, 4, 65-72.
20. G. Zhou, D.-W. Wang, F. Li, P.-X. Hou, L. Yin, C. Liu, G. Q. Lu, I. R. Gentle and H.-M. Cheng, *Energy Environ. Sci.*, 2012, 5, 8901.
21. X. Ji, K. T. Lee and L. F. Nazar, *Nat. Mater.*, 2009, 8, 500-506.
22. Q. Zhang, J. Q. Huang, W. Z. Qian, Y. Y. Zhang and F. Wei, *Small*, 2013, 9, 1237-1265.
23. X. Ji, S. Evers, R. Black and L. F. Nazar, *Nat. Comm.*, 2011, 2, 325.
24. S. Evers, T. Yim and L. F. Nazar, *J. Phys. Chem. C*, 2012, 116, 19653-19658.
25. Y. J. Choi, B. S. Jung, D. J. Lee, J. H. Jeong, K. W. Kim, H. J. Ahn, K. K. Cho and H. B. Gu, *Phys. Scripta*, 2007, T129, 62-65.
26. L. Ma, H. Zhuang, Y. Lu, S. S. Moganty, R. G. Hennig and L. A. Archer, *Advanced Energy Materials*, 2014, 4, 1400390.
27. W. Zhou, H. Chen, Y. Yu, D. Wang, Z. Cui, F. J. DiSalvo and H. D. Abruña, *ACS Nano*, 2013, 7, 8801-8808.
28. G. Zheng, Q. Zhang, J. J. Cha, Y. Yang, W. Li, Z. W. Seh and Y. Cui, *Nano Lett.*, 2013, 13, 1265-1270.
29. B. Meyer, *Chem. Rev.*, 1976, 76, 367-388.
30. M. S. WHITTINGHAM, *Science*, 1976, 192, 1126-1127.
31. C. Yi, S. Qi, D. Zhang and M. Yang, in *Carbon Nanotubes*, eds. K. Balasubramanian and M. Burghard, Humana Press, 2010, vol. 625, ch. 2, pp. 9-17.
32. H. J. Kim, I. S. Bae, S. J. Cho, J. H. Boo, B. C. Lee, J. Heo, I. Chung and B. Hong, *Nanoscale Res. Lett.*, 2012, 7, 30.
33. M. A. Ali, S. Srivastava, P. R. Solanki, V. Reddy, V. V. Agrawal, C. Kim, R. John and B. D. Malhotra, *Sci. Rep.*, 2013, 3.
34. Z. W. Seh, Q. Zhang, W. Li, G. Zheng, H. Yao and Y. Cui, *Chem. Sci.*, 2013, 4, 3673-3677.
35. T. Yoshida, K. Sakakibara, M. Asami, K.-H. Chen, J.-H. Lii and N. L. Allinger, *J. Comput. Chem.*, 2003, 24, 319-327.

36. D. Aurbach, E. Pollak, R. Elazari, G. Salitra, C. S. Kelley and J. Affinito, *J. Electrochem. Soc.*, 2009, 156, A694.
37. M. A. Hampton, C. Plackowski and A. V. Nguyen, *Langmuir*, 2011, 27, 4190-4201.
38. X. Liang, C. Hart, Q. Pang, A. Garsuch, T. Weiss and L. F. Nazar, *Nat. Comm.*, 2015, 6.
39. Z. Wang, Y. Dong, H. Li, Z. Zhao, H. B. Wu, C. Hao, S. Liu, J. Qiu and X. W. Lou, *Nat. Comm.*, 2014, 5, 5002.
40. J. W. Thomson, K. Nagashima, P. M. Macdonald and G. A. Ozin, *J. Am. Chem. Soc.*, 2011, 133, 5036-5041.
41. R. E. Davis and H. F. Nakshbendi, *J. Am. Chem. Soc.*, 1962, 84, 2085-2090.
42. A. Jimeno, S. Goyanes, A. Eceiza, G. Kortaberria, I. Mondragon and M. A. Corcuera, *J. Nanosci. and Nanotechnol.*, 2009, 9, 6222-6227.
43. J. H. Kim, T. Kim, Y. C. Jeong, K. Lee, K. T. Park, S. J. Yang and C. R. Park, *Adv. Energy Mater.*, 2015, 5, 1500268.
44. R. D. Rauh, K. M. Abraham, G. F. Pearson, J. K. Surprenant and S. B. Brummer, *J. Electrochem. Soc.*, 1979, 126, 523-527.
45. M. J. Frisch, G. W. Trucks, H. B. Schlegel, G. E. Scuseria, M. A. Robb, et al, *Gaussian, Inc.*, Wallingford, CT, USA, 2009.

Appendix

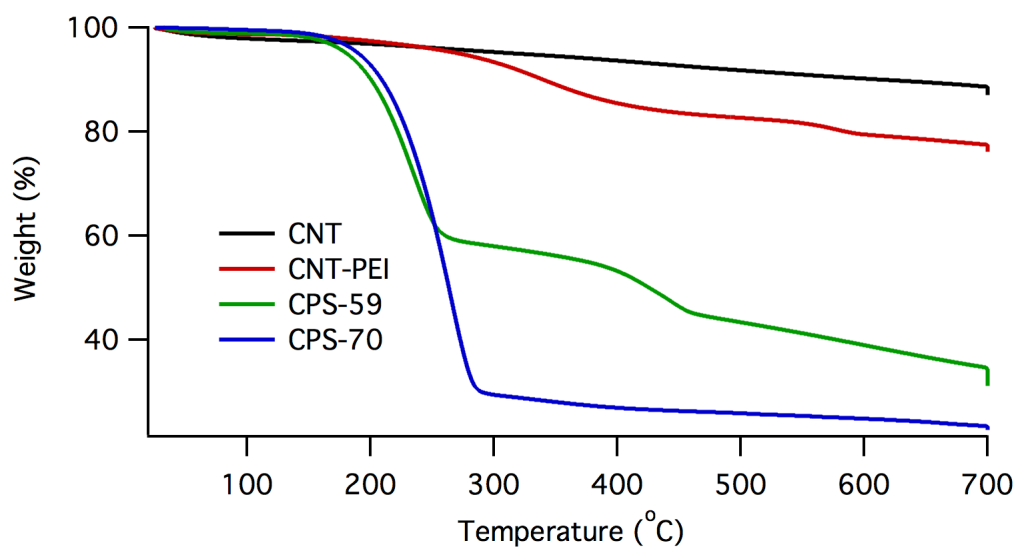


Figure S3.1 Thermogravimetric analysis of CNT-PEI and CNT-PEI/S composite with different sulfur loadings.

Method to determine sulfur content in different composite.

Take CPS-59 as an example. $W_s = 1 - W_{PEI} - W_{CNT}$

$$W_{CNT} = 0.31$$

From TGA of CNT-PEI, $W_{PEI} / W_{CNT} = (1 - 0.76) / 0.76 = 0.32$

$$W_s = 1 - W_{PEI} - W_{CNT} = 1 - 0.32 * 0.31 - 0.31 = 0.59$$

Table S3.1 Physical characterization by BET (Brunauer–Emmett–Teller) analysis.

	BET total surface area (m ² /g)	Pore volume (cm ³ /g)	Micropore surface area (m ² /g)	BJH pore size (nm)
CNT	348.2	3.2	16.1	16.0
CNT-PEI	280.6	2.5	11.2	15.6
CPS-59	68.7	0.53	6.9	3.2
CPS-70	39.7	0.09	4.3	2.5

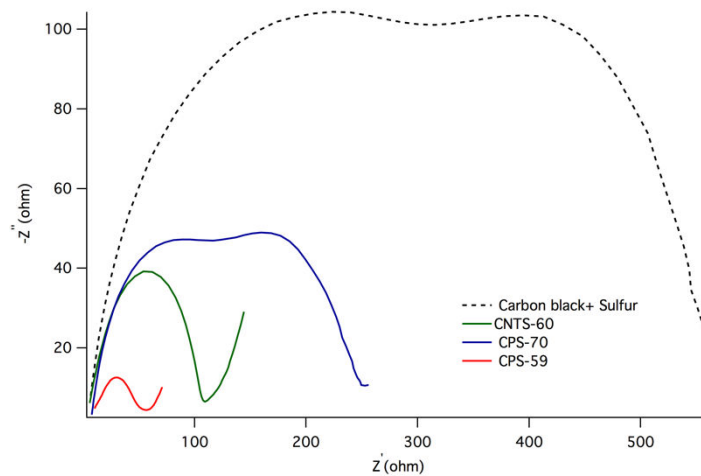


Figure S3.2 Impedance of electrode with sulfur loaded onto different carbon matrix. (Sulfur content is 70 wt% in physical mixing of carbon black and sulfur).

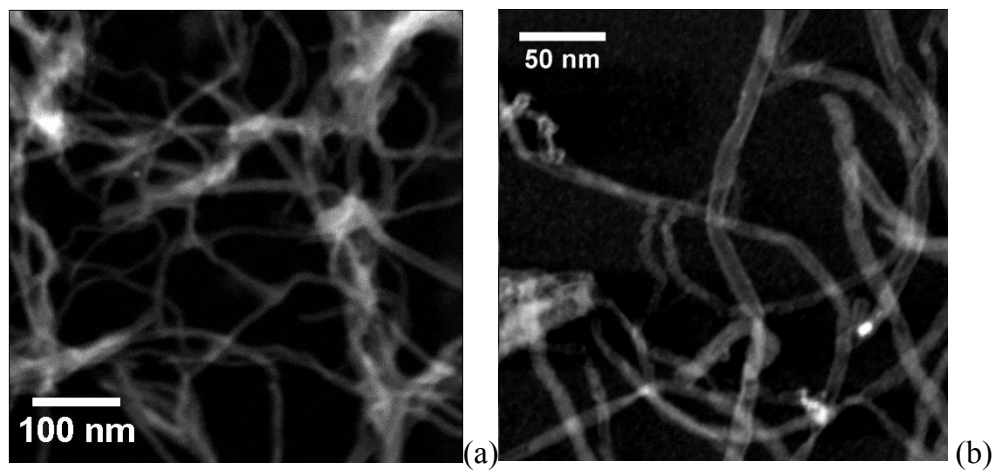


Figure S3.3 TEM of CNT-PEI/S composite (CPS-59).

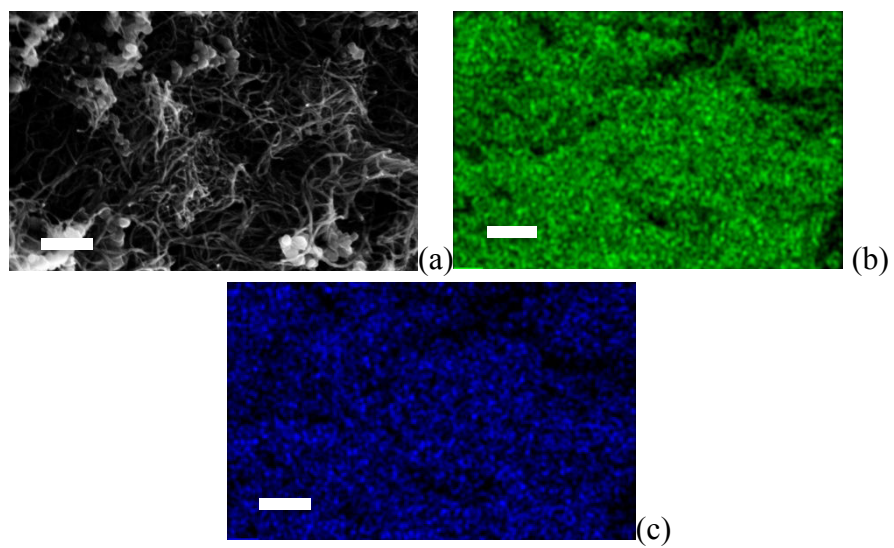


Figure S3.4 Elemental mapping of the distribution of carbon (b) and sulfur (c) in CPS-59 of the selected area (a). Scale bar=200nm.

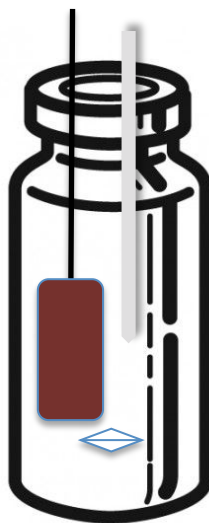


Figure S3.5 Equipment for the kinetic study of LiPS dissolution.

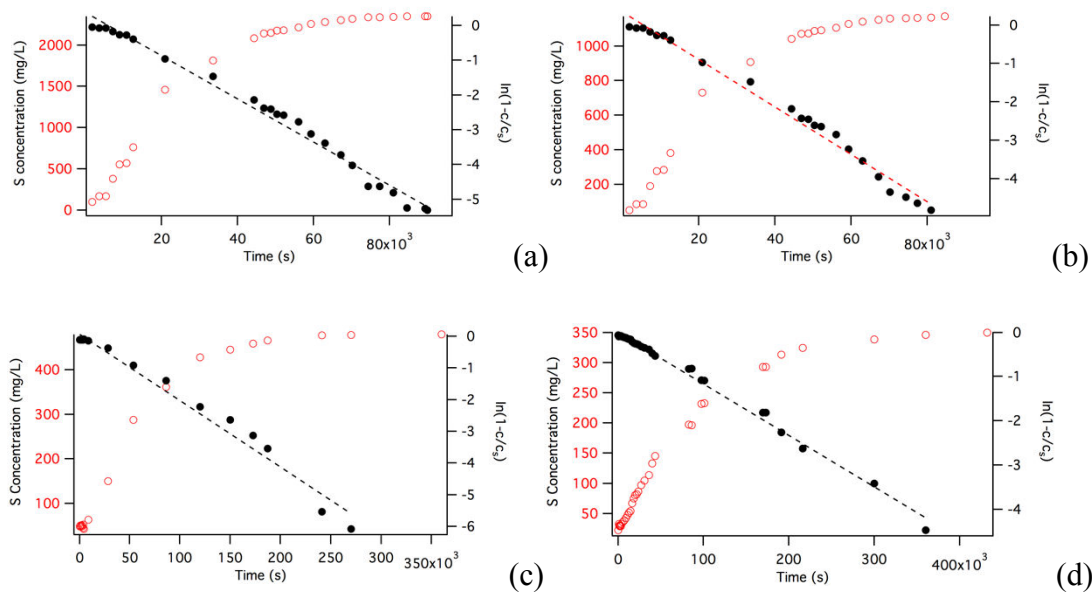


Figure S3.6 Sulfur concentration vs. time in (a) Li_2S_9 electrode with unmodified CNT; (b) Li_2S_4 electrode with unmodified CNT; (c) Li_2S_9 electrode with CNT-PEI composite; (d) Li_2S_4 electrode with CNT-PEI composite.

CHAPTER 4

Hybrid Cathode Architectures for Lithium Batteries based on TiS_2 and Sulfur

Adapted with permission from

L. Ma, S. Wei, H. L. Zhuang, K. E. Hendrickson, R. G. Hennig, L. A. Archer, Hybrid Cathode Architectures for Lithium Batteries based on TiS_2 and Sulfur, *Journal of Materials Chemistry A*, 2016, 3, 19857-19866

4.1 Abstract

Great efforts have been devoted to development of rechargeable lithium-sulfur (Li-S) battery designs that offer extended cycling. The poor electronic and ionic conductivity of sulfur and its reduction compounds with lithium; solubility of some sulfides in the most commonly used Li-S electrolyte solvents; and the volume changes that accompany lithiation and delithiation processes in a sulfur cathode, pose significant challenges that have so far impeded commercialization of rechargeable Li-S batteries. We demonstrate that TiS_2 , which uses an intercalation chemistry and is known for its high rate capability and stable performance as a lithium battery cathode, and sulfur, which has very high capacity (1675mAh/g) when coupled in a conversion-based electrochemical reaction with lithium metal, can be combined to produce hybrid cathodes in which the two materials function synergistically in the same electrolyte and within the same working voltage. We further show that co-generation of interconnected S_8/TiS_2 hybrid foams through thermal reaction of Ti precursor foams and S_8 yields 3D hybrid cathode structures in which sulfur is infused into porous TiS_2 foams. In galvanostatic electrochemical cycling studies the hybrid cathodes demonstrate high areal specific capacity ($9\text{mAh}/\text{cm}^2$) and high retention ratio even at a relatively large areal mass loading of $\sim 40\text{mg sulfur}/\text{cm}^2$ and high current density

(10mA/cm²). We attribute the improved performance of the materials to the synergistic effect in which TiS₂ not only improves the conductivity and rate capability of the cathode, but exerts a strong affinity for soluble lithium polysulfides, which limit their loss to the electrolyte.

4.2 Introduction

Rapid advances in multiple areas of technology — portable devices, electric vehicles and renewable energy generation systems are fueling demand for safe and high efficiency energy storage.^{1,2} Since their introduction in the mid 1990s, rechargeable lithium ion batteries (LIBs) have rapidly gained market share over other storage solutions and, notwithstanding their limited storage capacity, they are today the dominant choice for portable electrical energy storage⁶⁻⁹. TiS₂ is among the earliest examples of an intercalating cathode material used in rechargeable lithium batteries. It offers the lowest weight and cost of all the layered dichalcogenides and exhibits both high electronic conductivity and high lithium diffusion rate, which are ideal transport features for a cathode material. The intercalation electrochemistry of TiS₂ has been intensively studied and reviewed by Whittingham.³⁻⁵ It is now understood that the material offers many advantages as a cathode, but suffers from its modest theoretical specific capacity (239 mAh/g) and low discharge voltage (2.1 V vs Li/Li⁺), compared to the later developed Li-ion batteries (LIB), such as LiCoO₂ and LiFePO₄.

Elemental sulfur, S₈, is like TiS₂ a promising lithium battery cathode material that utilizes earth abundant constituents, but is limited by a low discharge voltage (~ 2.2 V). Unlike TiS₂, the S₈ cathode is based on a conversion redox chemistry, $16\text{Li} + \text{S}_8 \rightleftharpoons 8\text{Li}_2\text{S}$, in which every sulfur atom can accommodate up to two lithium ions in the discharged state, for an exceptional theoretical specific capacity (1675 mAh/g) and high specific energy (2600 Wh/kg or 2800 Wh/L).⁶⁻⁸ The

chemistry also occurs spontaneously, is in principle fully reversible, and does not require intervention using catalysts or other means. In practice however, lithium batteries based on sulfur cathodes achieve only a fraction of their theoretical capacity due to poor utilization of the active material. This problem can be traced to multiple sources. First, sulfur and its reduction products with lithium are poor electronic and ionic conductors. Carbon in a spectrum of forms is among the most studied materials used as cathode additives for improving electronic conductivity of the sulfur cathode and it is rare to find functional sulfur cathodes with more than 70% of the active material. To overcome the poor ionic conductivity of sulfur and its reduction compounds, electrolytes that dissolve some or all of the active cathode material are often used to take advantage of faster ionic transport in the liquid state. Secondly, the complicated solution electrochemistry of sulfur results in the formation of different types of lithium polysulfides (Li_2S_x , LiPS) during normal cell cycling. Unfortunately, the most sulfur-rich of the LiPS species dissolve freely in the electrolyte and are able to diffuse to and react with an unprotected anode.⁹ This process consumes the active electrode material at both the cathode and anode, and also leads to formation of a passivating layer on the anode, which increases its interfacial resistance over many charge/discharge cycles. Together, these problems lead to unstable cell performance and capacity loss over time. A final, more practical drawback is that the insulative properties of sulfur limits the cathode loading to below 2 mg/cm^2 ,¹⁰⁻¹³ which means that an assessment of specific energy on a more practically relevant per cell basis leads to values below what is achievable in present LIB where much higher active materials loading ($\sim 20 \text{ mg/cm}^2$) are typical.^{14, 15} The study by Jie¹⁶ nicely underscores the case for new Li-S cell designs in which high sulfur loadings are achieved in the cathode, in order for the sulfur cathode to live up to the potential for this chemistry.

An important breakthrough in understanding of the synergistic roles carbon may play in facilitating electronic transport in the cathode and limiting LiPS loss to the electrolyte has fostered interest in rational approaches for engineering the battery cathode. Mesoporous and microporous carbons have for example been shown to provide the ability to sequester sulfur and its reduction products in the cathode.^{6, 17-20} Carbon nanotubes/fibers,²¹⁻²⁵ graphene/graphene oxide sheet,²⁶⁻²⁸ and carbon spheres^{12, 29, 30} have likewise been investigated as additives in the cathode that simultaneously increase electronic conductivity and limits fading due to LiPS loss. The interaction between LiPS and the non-polar carbon surface is unfortunately weak, thus the LiPS physically trapped in the carbon barrier materials will eventually leach into the electrolyte driven by the chemical potential gradient between these species in the cathode and electrolyte. Because this driving force increases with sulfur loading in the cathode, these proposed solutions become less effective when cells based on high active materials loadings in the cathode are evaluated. Density functional analysis of LiPS in the cathode has been reported by multiple groups to show that introduction of oxygen- and amine-containing functional groups in the cathode increases binding of LiPS and limits its loss.³¹ On this basis one can rationalize early research using oxide particles or polymers as adsorbents or additives in the cathode,³¹⁻³⁷ which show some improvement in cyclability of sulfur cathodes. A drawback of this approach has been that all of the additives that strongly bind LiPS in the cathode are electronic insulators and compromise the ability to also achieve high active loadings.

Herein we report on TiS₂/S₈ hybrid cathode materials that offer multiple synergistic attributes that make them attractive for achieving improved active material utilization and high loadings. First, the majority of the discharge for a S₈ cathode occurs at nearly the same potential as for TiS₂. It means that the materials can be employed in a hybrid cathode without the need for

sophisticated electronic controls. Second, TiS_2 has high conductivity, both electronic and Li ion conductivity, which means that it can be used to augment transport in a sulfur cathode. Third, DFT analysis of TiS_2/S_8 hybrids show that TiS_2 binds to LiPS with an affinity nearly ten times stronger than carbon-based materials such as graphene, which can help reduce LiPS loss to the electrolyte. Based on these attributes, it is feasible to combine TiS_2 and S_8 in a hybrid cathode such that the high conductivity and strong binding affinity of TiS_2 for LiPS helps to overcome the low conductivity and high tendency for dissolution of sulfur species. Fourth, both TiS_2 and S_8 are electrochemically active, which means that there are inherent synergies that can help enhance energy storage capacity of the cathode. Finally, TiS_2 can be synthesized in a variety of architectures that allows these synergies to be investigated in multiple cathode configurations.

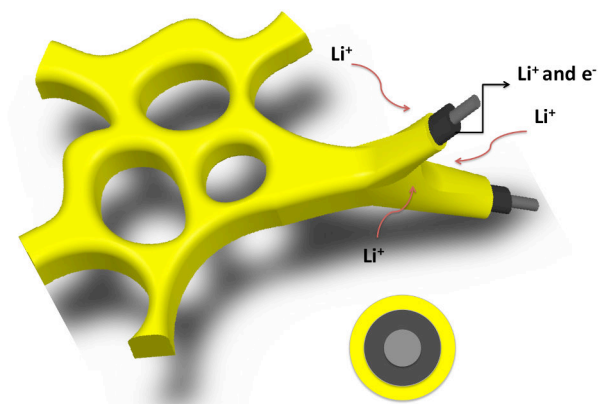
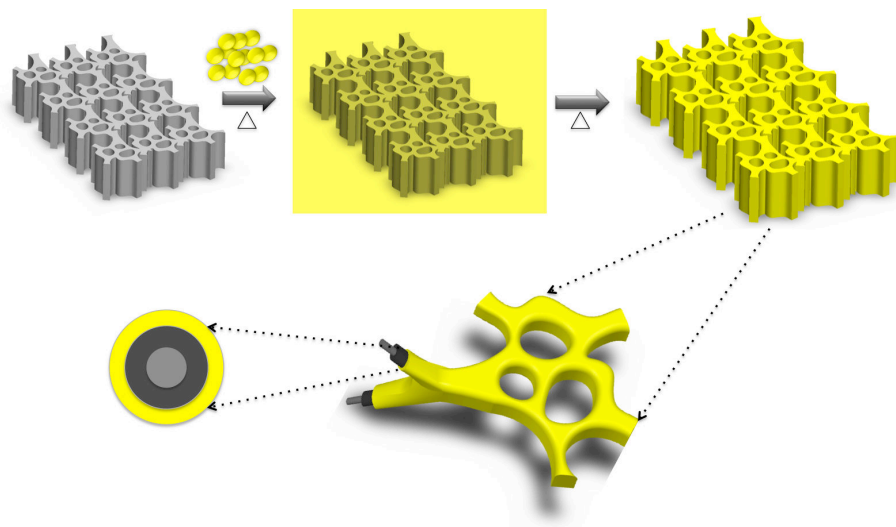


Figure 4.1 (a) One-step method to prepare sulfur infused TiS_2 foam. (b) Diagram of the cross section of the foam during discharge. Yellow: Sulfur; Dark gray: TiS_2 ; Gray: Ti.

This report investigates the structure and electrochemical characteristics of two TiS_2/S_8 hybrid cathode configurations. The first, depicted in **Figure 4.1** is a TiS_2/S_8 foam created by infusing sulfur in a closed vessel into a 3D titanium metallic foam structure followed by high temperature reaction of Ti and S_8 to form TiS_2/S_8 composites with varying sulfur contents (**Figure 4.1**). The foam design is attractive because the high surface area and porous structure facilitates good transport of electrons and ions, allowing much higher active materials loadings to be realized than typical for TiS_2 or sulfur cathodes. Additionally, by infusing sulfur into the foams, no binder or conductive additive is needed, which will further increase the percentage of active materials. By systematically adjusting the Ti/ S_8 ratio and the reaction temperature, it is possible to systematically vary the TiS_2 to S_8 ratio on the cathode to evaluate its effect on performance. We compare structure and electrochemistry of these materials with those obtained in a second design, wherein the preformed TiS_2 particles are physically blended with sulfur.

4.3 Results and discussion

It has been reported that in contrast to most other electrode materials which exhibit improved transport properties upon integration of conductive carbon additives, integration of carbon in a TiS_2 cathode may lead to reduced performance by disordering the TiS_2 sheets and pinning Li-ion transport between the layers. The strong affinity between LiPS and TiS_2 means that care is needed in designing the hybrid cathode to avoid similar problems. We first investigated the simpler of the two hybrid cathode designs created by physically mixing TiS_2 and sulfur, as described in the experimental section. **Figure 4.2** compares the voltage profiles for the TiS_2 /carbon, Sulfur/carbon, and the TiS_2/S_8 hybrid cathode in the same electrolyte (1M LiTFSI and 0.2M LiNO_3 in DOL/DME (v:v=1:1)). The TiS_2 electrode shows symmetric discharge and

charge characteristic, with a working voltage between 1.9-2.3 V, which overlaps with the range seen for the sulfur electrode. Results reported in **Figure S4.1** shows that the TiS_2 /carbon cathode exhibits very stable cycling performance, with a capacity around 200mAh/g at a slow scan rate of 0.1C. These results are comparable to those reported in reference ³⁻⁵ and indicate that the activity of TiS_2 is not compromised by the carbon component or by the electrode processing procedures used in the present study.

More information can be obtained by comparing the voltage profile of the TiS_2 /carbon and sulfur/carbon electrodes with that obtained for the TiS_2/S_8 hybrid cathode. In the discharge process, the hybrid electrode is observed to display an additional short plateau at a slightly lower potential near the end of the typical extended second plateau for a S_8 cathode. This feature is unique to the hybrid cathode and we associate it with reduction of TiS_2 . The final voltage drop at the end of the discharge is also not as steep as observed for typical elemental sulfur electrode. Also, in the charge process, the over potential for the hybrid cathode disappears at the beginning of the process, which can be compared with the obvious and large overpotential observed at the same rate for the sulfur electrode. These changes all indicate that TiS_2 is electrochemically active in a TiS_2/S_8 hybrid cathode created by simply blending the two materials. Furthermore, **Figure S4.1** shows obvious improvement in utilization of the active materials with the incorporation of TiS_2 into the sulfur electrode. The higher capacity in the hybrid system also indicates that the dissolution and loss of LiPS (lithium polysulfides) is greatly suppressed. This plot also nicely illustrates how TiS_2 and sulfur work synergistically in the cathode—the capacity of the electrode is improved by incorporation sulfur into TiS_2 , while the utilization rate and rate capability of sulfur is greatly improved by adding of TiS_2 . **Table S4.1** summarizes the comparison of the battery performance with different cathode materials. It is obvious that the degradation rate is

decreased and the utilization rate is increased with the incorporation of TiS_2 . A similar concept has already been demonstrated in the mixed rate cathodes proposed by Whittingham, as early as 1981.⁵ In these cathodes, MoS_3 was used as the high-energy component. Their idea was that the admixture of TiS_2 with a higher energy density but lower rate cathode material, such as MoS_3 , should allow the retention of the latter's high capacity whilst permitting high current capability. **Figures S4.1b~4.1d** clearly show that this concept works arguably even better for sulfur--- the performance of sulfur at high rate is seen to be dramatically improved with the incorporation of TiS_2 while the overall electrode capacity is as obviously improved by incorporation of the high capacity sulfur in the cathode. It has to be noticed that the electrode preparation procedure used herein does not involve complex electrode engineering but it already shows obvious improvement in the hybrid system, and we expect more dramatic effect when nanomaterials or other technique are involved.

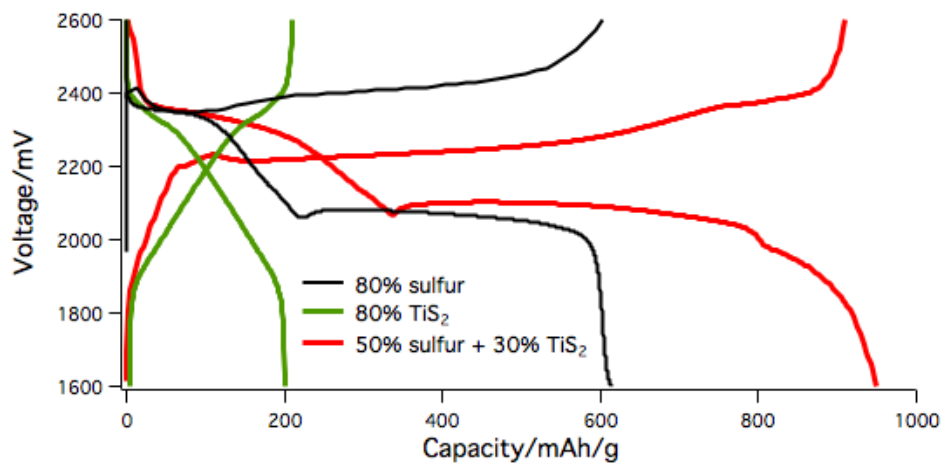


Figure 4.2 Voltage profile of electrodes containing TiS₂, Sulfur, and TiS₂-sulfur mixture.

To understand the interactions between TiS_2 and sulfur, we performed density-functional theory + U calculations where the localized Ti d orbitals are treated with the Hubbard U correction. **Figures 4.3a** and **4.3b** illustrate respectively top and side views of the optimized atomic structures of a Li_2S trimer adsorbed on TiS_2 . As can be seen, the two Li atoms are relaxed to the positions atop the central S atom of the 6-membered rings of TiS_2 in order to maximize the attractive interactions between the Li cations and surrounding S anions. Bader analysis shows that 0.9 electrons are transferred from the Li to S atoms implying robust ionic bonding. Significant interactions between Li_2S and TiS_2 are also manifested by a large positive binding energy that is determined as 2.60 eV. This value is nearly three-times greater than that between LiPS and polyacrylonitrile as reported in our earlier study³¹ and around ten times higher than that between LiPS and carbon-based graphene. This result is also consistent with that of Cui's group, where they apply TiS_2 as a capsule coating for Li_2S electrode.⁴⁴ Thus the DFT prediction demonstrates the great potential of TiS_2 as LiPS sorbents in sulfur cathode to prevent LiPS dissolution and loss to the electrolyte. The results presented in Figure S1 also lend support to this idea, where the TiS_2/S_8 hybrid electrode shows much higher capacity and higher utilization of the active materials than that of sulfur electrode, indicating that more active materials is maintained in the electrode in the case of hybrid system compared with that in the sulfur electrode.

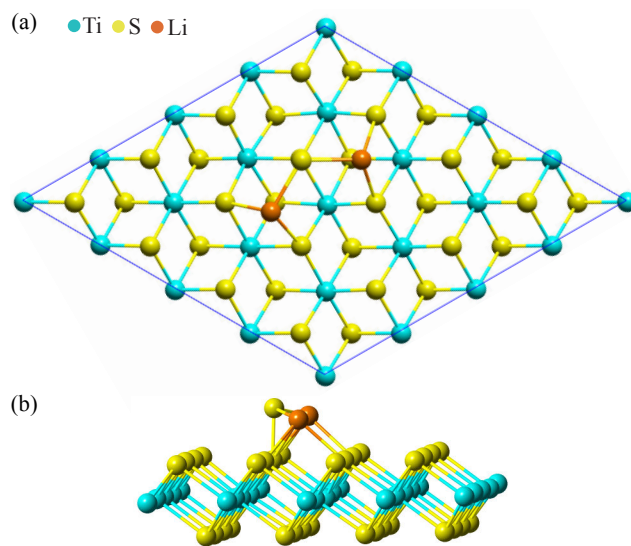


Figure 4.3 (a) Top and (b) side views of Li₂S adsorption on TiS₂.

The binding affinity of TiS_2 for LiPS can also be evaluated by characterizing the dissolution of LiPS in a good solvent, such as tetraethylene glycoldimethyl ether (tetraglyme), which is also a direct way to verify DFT calculation. Cathodes comprised of Li_2S_4 , binder and different matrix (with or without TiS_2) were immersed into tetraglyme, and ICP-AES as applied to characterize the time-dependent content of the polysulfides dissolved in the electrolyte by detecting the sulfur concentration in a small amount of extracted electrolyte every 10 min. **Figure 4.4** shows that consistent with the DFT calculation, in the cases where only carbon is providing physical barrier for LiPS dissolution, the concentration of LiPS dissolved in the electrolyte increases rapidly with time. However, when some part of the carbon is replaced with TiS_2 , LiPS dissolution is greatly suppressed, which can be attributed to the strong affinity for LiPS of TiS_2 .

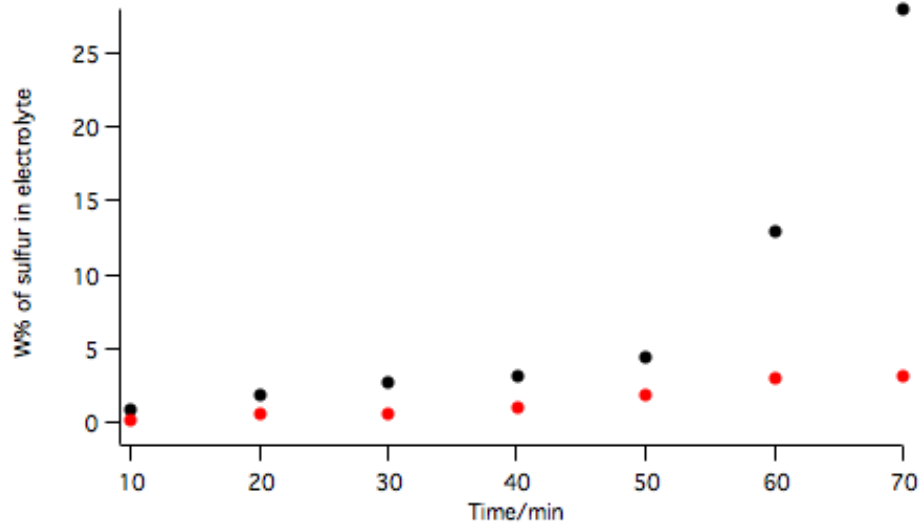


Figure 4.4 Sulfur content in tetraglyme for two different cases (black represents the case of carbon matrix without TiS₂; red with TiS₂).

Electrochemical Impedance Spectroscopy (EIS) and SEM were used to characterize the hybrid cathodes before and after cycling. **Figure 4.5a** shows that the width of the Nyquist plot decreases by a factor of at least four upon incorporation of TiS_2 in a sulfur cathode. The figure also shows that this trait is shared with the TiS_2 , meaning it likely reflects the high interfacial conductivity of the cathode, brought about by incorporation of TiS_2 . This observation is obviously important because the insulating nature of sulfur is one of the major factors thought to impede utilization of the material in the cathode. **Figures 4.5b-d** compare the impedance spectra for the three electrode materials measured before and after galvanostatic cycling. It is seen that the spectra for the TiS_2 electrode change little, indicative of an electrode able to form a very stable interphase with the electrolyte. In contrast, the sulfur cathode shows a clear change in its impedance spectrum after cycling, with a new interface (second lobe) appearing after the electrode is cycled. This behavior is consistent with earlier studies, which report deposition and gradual build-up of a Li_2S insulating layer onto the electrode after cycling.³⁸⁻⁴⁰ Interestingly, for the TiS_2/S_8 hybrid cathode, the impedance spectrum shrinks after cycling, a feature the hybrid electrode evidently shares with the TiS_2 cathode. It may indicate that interaction between TiS_2 and LiPS species might help to facilitate a more uniform deposition of Li_2S onto the electrode. **Figure 4.6** compares the morphology of the electrode before and after cycling as revealed by SEM analysis. For the sulfur electrode, voids are clearly present on the electrode surface, which are covered by large particles after cycling; the particles are likely the Li_2S layer that gives rise to the 2nd lobe in the impedance spectrum. On the other hand, for the TiS_2/S_8 hybrid cathode, the morphology of the electrode is maintained after cycling.

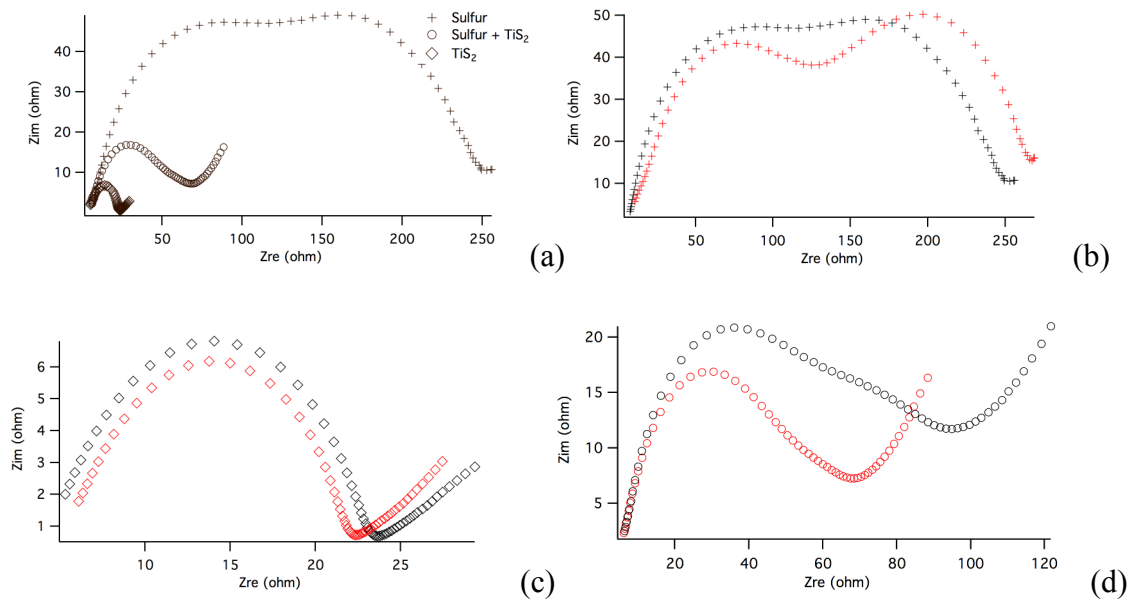


Figure 4.5 (a) Comparison of Impedance spectra of Sulfur, TiS₂ and TiS₂/S blended system. Impedance before (black) and after (red) cycling of (b) sulfur electrode, (c) TiS₂ electrode. (d) TiS₂/S₈ hybrid cathode.

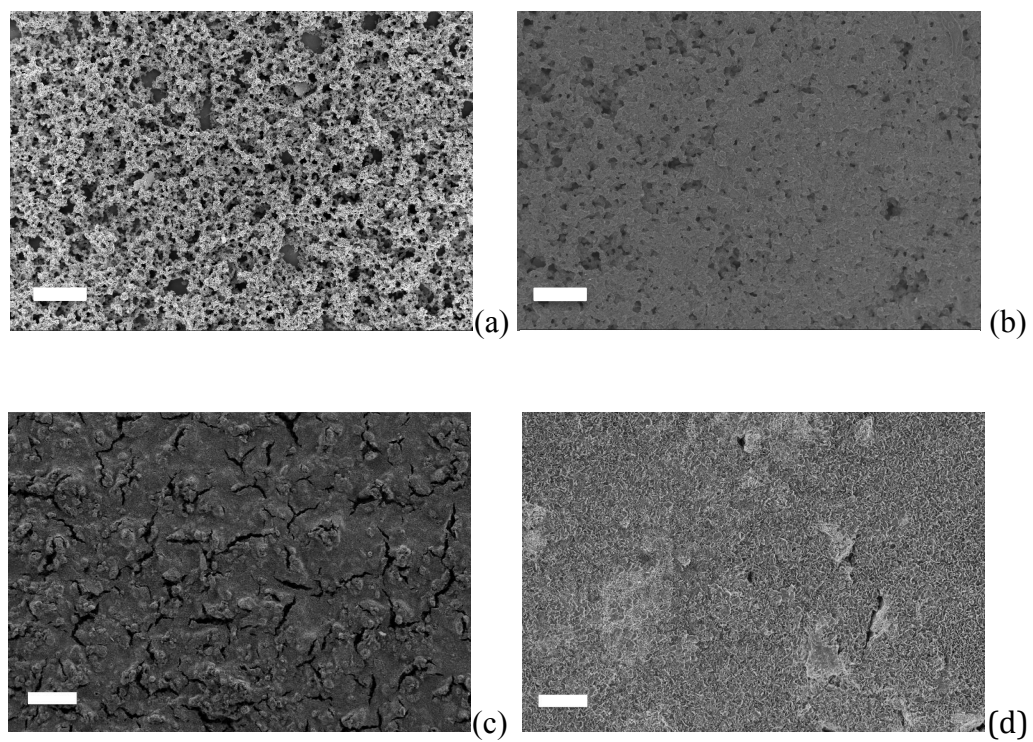


Figure 4.6 SEM images of sulfur electrode before cycling (a), after cycling (b); TiS₂/S₈ hybrid cathode before cycling, (c); after cycling, (d). Scale bar =50 μ m.

While the synergies of TiS_2 and S_8 are already demonstrated to be real and beneficial from our studies of simple blended electrodes, the materials provide opportunities for designing novel 3D hybrid cathode architectures that take advantage of these synergies to achieve high active material loadings. Specifically, we now turn to consideration of TiS_2/S_8 foams created using a 1-step infusion approach. The materials preparation procedures are described in detail in the Experimental section. Pure Ti metal foam (XRD and SEM shown in **Figure S4.2a** and **Figure S4.2b** respectively) was physically mixed with different amounts of sulfur and sealed in vacuum quartz tube. The mixture was heated to various temperatures for 6h to facilitate infiltration of sulfur vapor into the pores and reaction with the Ti metal framework to achieve a conformal coating of the structure. Initial evidence that the procedure is successful comes from the observation that irrespective of the sulfur/Ti ratio employed, the product preserves the foam-like texture of the starting Ti material. It is comprised of three parts: an unreacted Ti metal core of the foam, a TiS_2 outer surface, and sulfur infused into the porous structure. TGA was performed in air to determine the content of each species in the foam (**Figure 4.7**). During the heating step from room temperature to 700°C , sulfur sublimates between $200\sim 300^\circ\text{C}$ (curve 3~5); TiS_2 is converted to TiO_2 (curve2)(XRD shown in **Figure S4.3**); and Ti metal exhibits no weight change (curve1). Based on the different reaction to heat of the three species, it is possible to compute the weight percentage of each of the three components in any foam synthesized using our approach. An example of the analysis is given in the supporting information (**Method 4.1**) and the results are listed in **Table 4.1**. The weight increase of the foam after heating should all come from elemental sulfur, regardless of whether it exists as S_8 or TiS_2 , which provides a straightforward approach to cross-check the content of each species (see **Table 4.1**). It is apparent from the table that the calculated compositions are close to the actual value. By increasing the ratio of S_8 to Ti

in the initial mixture, the portion of the Ti foam that is converted to TiS_2 increases, and the content of sulfur present in the foam also increases. The sulfur loading in TSF5, TSF10, and TSF15 are substantially higher than typically studied in lithium-sulfur cells, $4.6\text{mg}/\text{cm}^2$, $21\text{mg}/\text{cm}^2$ and $40\text{mg}/\text{cm}^2$, respectively; confirming that the 3D hybrid structures do allow us to achieve the goal of comparable or higher cathode loadings to what is possible in LIB cathodes. **Figure S4.4** are SEM images of TSF5, TSF10 and TSF15, respectively, which shows that all of the materials maintain their porous foam-like structure.

X-ray Diffraction (XRD) analysis was used to characterize the chemical compositions of the species in the hybrid foams (**Figure 4.8**). Curve 1 is the XRD spectrum of pure TiS_2 powder, which matches perfectly to the TiS_2 crystal structure, with a strong characteristic peak around 15° , indicating the (001) surface of TiS_2 crystal. Irrespective of the initial sulfur loading, the subsequent figures show that diffraction identified with TiS_2 is always evident. Beginning with TSF5, small sulfur peaks begin to appear in the foam and by TSF10 and TSF15 very clear and strong sulfur peaks are observed, indicating the existence of elemental sulfur. The XRD spectra do not show Ti metal peak though we have shown on the basis of TGA some unreacted Ti metal is present for all of the materials. Raman spectra also show features consistent with sulfur that becomes more distinct as the sulfur content is increased (**Figure S4.5**).

Table 4.1 S₈/ TiS₂/Ti content in TSF5, TSF10, and TSF15. Percentage of sulfur, TiS₂ and Ti metal, the mass ratio of Ti:S, the molar ratio of Ti:S is calculated from TGA. The last column shows the mass ratio of Ti:S originally added to quartz tube.

	S ₈ (wt. %)	TiS ₂ (wt. %)	Ti metal (wt. %)	Ti:S(mass)	Ti:S(molar)	Ti:S (input mass)
TSF5	5	87	8	1:1.21	1:1.8	1:1.19
TSF10	20	73	7	1:1.62	1:1.24	1:1.63
TSF15	34	62	4	1:2.19	1:3.3	1:2.21

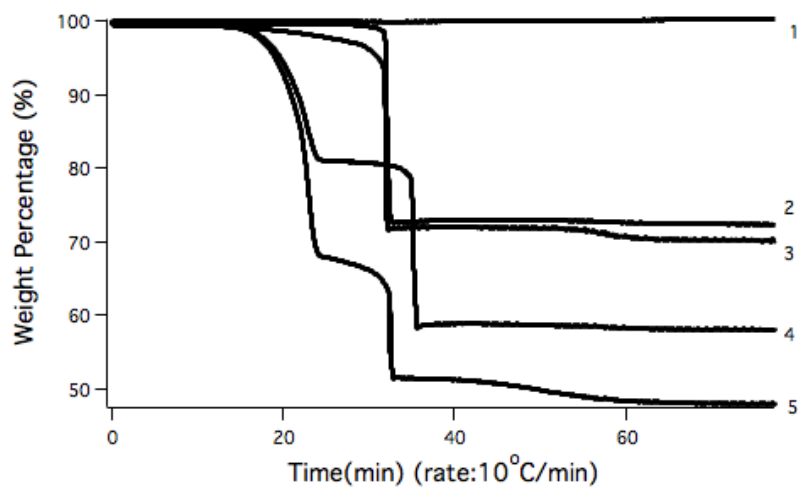


Figure 4.7 Thermogravimetric analysis of 1. Pure Ti metal; 2. Pure TiS_2 powder; 3. TSF-5; 4. TSF-10; 5. TSF-15 burned in air.

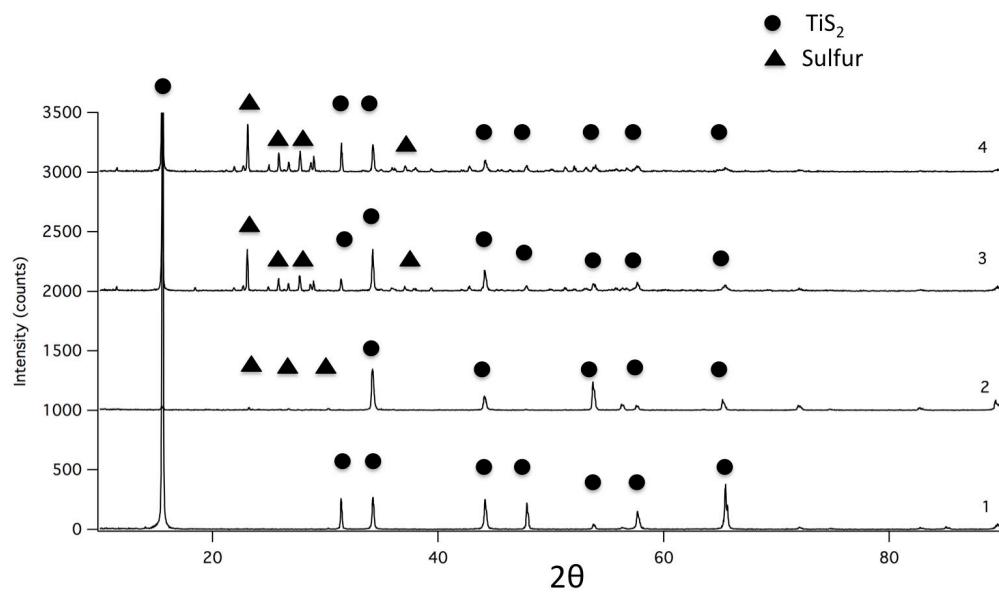


Figure 4.8 XRD analysis of 1. Pure TiS_2 powder. 2. TSF5. 3. TSF10. 4. TSF15.

Electrochemical characterization was performed for the three different foam compositions summarized in **Table 4.1**. Consistent with expectations for our design, hybrid electrodes with high areal energy densities are achieved, even at high current density. **Figure 4.9a** compares the voltage profiles for the TSF5, TSF10 and TSF15 hybrid materials. For TSF5, in which sulfur comprises approximately 5% of the total weight, the voltage profile shows characteristic similar to those noted for pure TiS_2 , in **Figure 4.2**. With the increase of sulfur content, the two-plateau characteristic of the sulfur discharge profile starts to emerge in TSF10. With further increase of sulfur content, an additional plateau appears in TSF15 at the end of the second plateau of sulfur profile, yielding a discharge voltage profile remarkably similar to that reported in **Figure 4.2** for the physical blend of TiS_2 and S_8 . **Figure 4.9c** reports voltage profiles for TSF15 at different current rates. At $2\text{mA}/\text{cm}^2$, the voltage profile shows two strong sulfur reduction plateaus, while with the increase of current density, the plateau shrinks and the sloping behavior seen in TiS_2 begins to dominate. When the current density reaches as high as $10\text{mA}/\text{cm}^2$, the voltage profile still exhibits the two plateaus around 2.3V and 1.9V, indicating sulfur is still active under this very high rate condition. In conventional sulfur/carbon cathodes, where the sulfur loading is typically in the range of $1\sim 2\text{mg}/\text{cm}^2$, the current rarely exceeds $2\sim 3\text{mA}/\text{cm}^2$, and the best capacity that can be obtained is typically $\sim 2\text{mAh}/\text{cm}^2$. **Figure 4.b** compares the cycling performance of TSF5, TSF10 and TSF15, which show that high discharge capacities are achieved and that there is a systematic increase of capacity as the sulfur content in the electrode rises. Thus it is apparent that sulfur is assisting the TiS_2 electrode in achieving high electrode capacity. At the same time, TiS_2 is beneficial to sulfur because it is facilitating high utilization of sulfur in the cathode so that sulfur can contribute substantially to the electrode capacity even at high loading—the sulfur loading in TSF15 is as high as $40\text{mg}/\text{cm}^2$, which we believe is the

highest value among all the previously reported studies (**Figure 4.9e**). With the architecture of TiS_2 foam, which has high conductivity and strong binding with LiPS, a cathode with high sulfur loading can operate at high current density while maintaining a high capacity. In terms of practical application, the gravimetric energy density is also important, especially when we take each component of the electrode into consideration, including conductive additives, binder and current collector. Although values of $\sim 1000\text{mAh/g}$ have been reported in the literature of Li-S battery, these are based on the weight of sulfur alone. When other necessary components are added, the specific capacity drops to $\sim 100\text{mAh/g}$ (calculation is shown in Supporting Information as **Method 4.2**). **Figure 4.9e** compares the gravimetric specific capacity and areal capacity of the TiS_2 foams, which requires neither binders nor additives, with conventional Li-S battery. **Figure 4.9e** clearly demonstrate the significance of our work—extremely high sulfur loading with high areal capacity, and also with values of specific capacity higher than most of the current reported Li-S study. It should be noted here that our cell can be cycled more than 100 cycles while the one in Ref. 25 cannot cycle for more than 20 cycles. Further optimization of the hybrid cathode architecture (the pore size, the thickness etc) and of the electrolyte composition used in electrochemical analysis are expected to widen the difference between the capacities achievable in our TiS_2/S_8 hybrid foams and that possible in sulfur/carbon cathodes at comparable active materials loading.

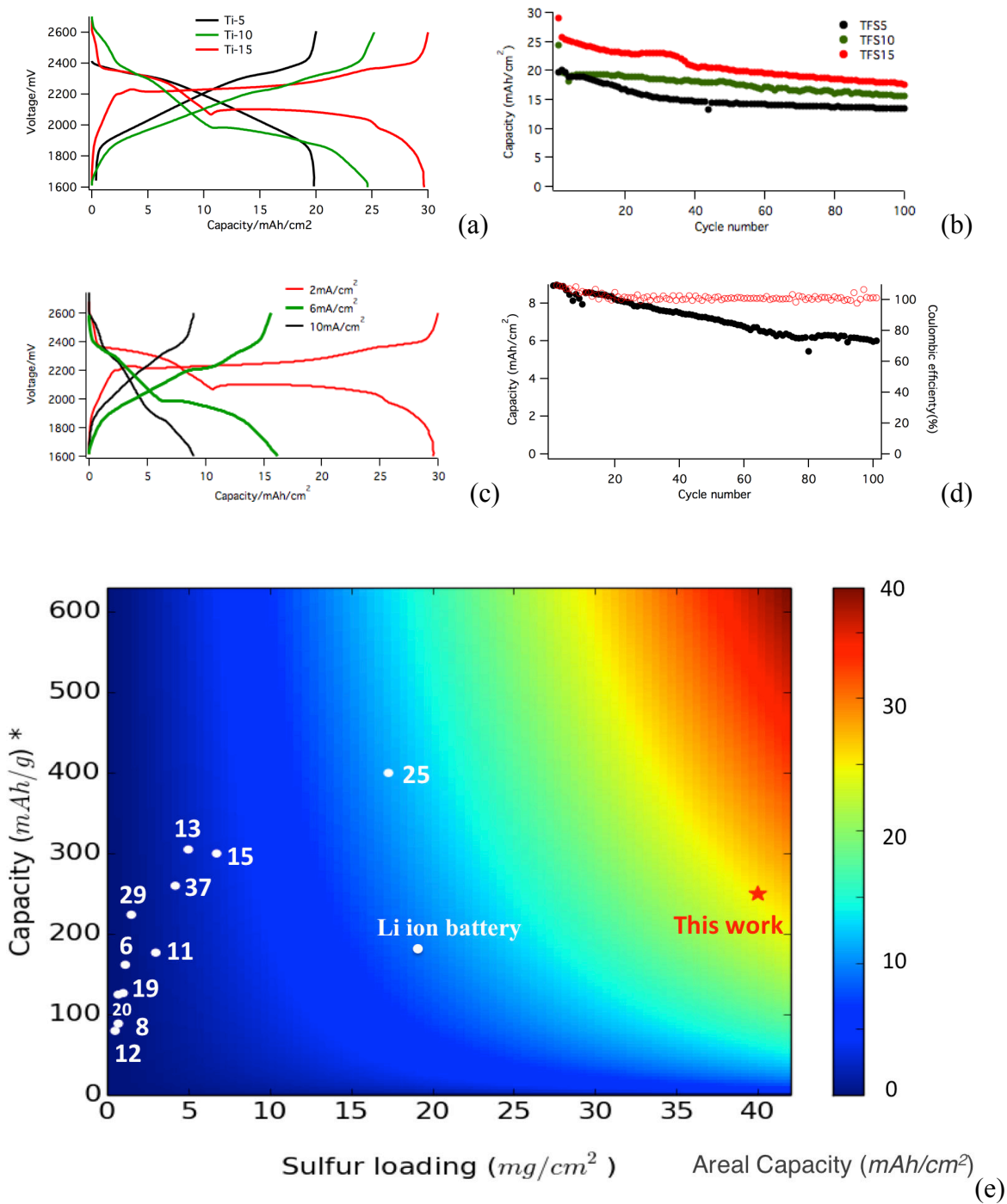


Figure 4.9 (a) Voltage profiles (b) Cycling performance of TFS5, TFS10, and TFS15 cycled at 2mA/cm². (c) Comparison of voltage profile of TFS15 at 2mA/cm², 5mA/cm² and 10mA/cm² respectively. (d) Cycling performance of TFS15 cycled at 10mA/cm². (e) Comparison of sulfur loading, the specific capacity, the areal capacity in this work with those in the references at the 20th cycle. *The specific capacity is calculated based on the weight of the whole electrode, and the calculation is shown in Supporting Information.

The discharged products were characterized by using XRD (**Figure S4.6**). Both TiS_2 and sulfur electrodes were prepared by slurry-coated alumina sheet, explaining the strong alumina peaks in spectrum (a) and spectrum (b). Spectrum (a) corresponds to the sulfur electrode after cycling, which shows that Li_2S is present. Spectrum (b) shows behavior consistent LiTiS_2 pattern, which corresponds to the discharged products of TiS_2 . However, for the XRD spectra of the discharge products of TSF15, there is no characteristic peaks of either Li_2S or LiTiS_2 . And actually it doesn't show obvious peaks, which means that there might be no crystal structure in the product. This might due to the interaction of LiPS and TiS_2 once the Li ion is inserted into the structure, which can disturb the structure of both Li_2S and LiTiS_2 . This is an indication that TiS_2 is interacting with LiPS strongly via chemical bonding.

4.4 Experimental section

4.4.1 Preparation of TiS_2/S blended system

Composite TiS_2/S cathodes were created on aluminum foil (0.004 in thick, Alfa Aesar) using slurries containing 50 wt% sulfur powder, 30 wt% TiS_2 (Sigma Aldrich), 10 wt% Super-P Li from TIMCAL, and 10 wt% poly (vinylidene difluoride) (PVDF, Sigma Aldrich) as binder in an excess of N-methyl-2-pyrrolidone (NMP) after mixing by a ball mill. After drying at 55°C for 12h in vacuum oven. The resulting slurry-coated aluminum was reduced to required dimensions with a punching machine. TiS_2 needs to be stored in argon-filled glovebox (Mbraun Labmaster) due to its sensitivity to the atmosphere and moisture. The 80 wt% sulfur electrode or 80 wt% TiS_2 electrode was prepared in the same way but with 80 wt% sulfur or TiS_2 , 10 wt% Super-P and 10 wt% PVDF.

4.4.2 Preparation of sulfur infused TiS₂ foam

Ti metal foam was obtained from American Elements and was dried before use. The metal foam and sulfur powder were sealed in quartz under vacuum. The sulfur amount was determined by the 2:1 molar ratio of S: Ti, besides, extra sulfur was added in various amounts for different test samples: 5mg/cm³ for “TSF5”, 10mg/cm³ for “TSF10”, 15mg/cm³ for “TSF15” respectively. The sealed quartz with the mixture was heated at furnace (Lindberg-Tube-Furnace-1000-C-1) at 780°C for 6h. The quartz were opened in glove box after quenched to room temperature in air.

4.4.3 Characterization of the hybrid cathode

Inductively coupled plasma atomic emission spectroscopy (ICP-AES) was used to quantify sulfur content in the electrolytes as a function of time. Impedance was measured versus frequency using a Novocontrol N40 broadband dielectric spectroscopy. Morphologies of the electrodes were studied using LEO 1550 FESEM. Crystal structure was characterized using Scintag Theta-Theta X-ray Diffractometer (XRD). Thermogravimetric analysis (TGA) was used to determine the content of sulfur, TiS₂ and Ti metal in the foam. Raman spectra was done by using Renishaw Invia Confocal Raman microscope.

4.4.4 Electrochemical Characterization

2032 coin-type cells were assembled using lithium metal (0.76 mm. thick, Alfa Aesar) as the anode electrode, a microporous polypropylene membrane, Celgard 2500 as separator, and 40uL of electrolyte consisting of 1M lithium bis(trifluoromethanesulfone) imide (LiTFSI) and 0.2M LiNO₃ in DOL (1,3-dioxolane) : DME (1,2-dimethoxyethane) (v:v=1:1) for each cell. In the TFS case, a glass fiber (Whatman Grade GF/D) was used as separator and 100 uL electrolyte was

used. For the cathode, a disk with diameter of 0.5 inch of the material was punched, which was either a carbon-sulfur composite, TiS₂, or a TiS₂/S blend. Cell assembly was carried out in an argon-filled glove-box (MBraun Labmaster 130). The room-temperature cycling characteristics of the cells were evaluated under galvanostatic conditions between 1.6V – 2.6V using Neware CT-3008 battery testers.

4.4.5 Theoretical Section

All density-functional theory calculations are performed using the Vienna *ab initio* simulation package (VASP).^{41, 42} The interactions between valence electrons and ionic cores are described with the projector augmented wave (PAW) method.^{43, 44} A plane wave basis set with a cutoff energy of 500 eV is used to expand the wavefunctions. For the exchange-correlation functional, we employ the Perdew-Burke-Ernzerhof (PBE) approximation.⁴⁵ The interactions between Li₂S and TiS₂ are simulated by a 4×4×1 supercell with a Li-S-Li trimer located above a single-layer TiS₂ nanosheet. A vacuum spacing of the supercell of 18 Å makes the interaction caused by the periodic boundary conditions negligible small. The atomic positions are fully optimized until the forces are smaller than 0.01 eV/Å. The first Brillouin-zone integration is carried out using 16×16×1 and 4×4×1 Γ -centered Monkhorst-Pack k-point meshes for the unit cell and supercell cases, respectively. The 3s²3p⁶4s²3d² states of the Ti atoms, the 3s²3p⁴ states of the S atoms, and the 1s²2s¹ states of the Li atoms are treated as valence states. A correction of effective Hubbard U of 2.1 eV is applied to the Ti d orbitals.⁴⁶ The binding energy E_b between TiS₂ and Li₂S is calculated with

$$E_b = E_{\text{TiS}_2} + E_{\text{Li}_2\text{S}} - E_{\text{TiS}_2+\text{Li}_2\text{S}},$$

where E_{TiS_2} is the total energy of a pristine TiS_2 nanosheet, $E_{\text{Li}_2\text{S}}$ denotes the total energy of the Li_2S trimer, and $E_{\text{TiS}_2+\text{Li}_2\text{S}}$ is the total energy of the combined system. Without using the Hubbard U parameter, we obtain an E_b of 2.98 eV, which is almost identical to the recently reported value (2.99 eV). Therefore, including U into the calculations is important to avoid an overestimate the binding energy.⁴⁷

4.5 Conclusion

In summary, we have shown that a hybrid Lithium-Sulfur battery cathode architecture, wherein the intercalating material TiS_2 known for its high rate and stable cycling features is combined with a high energy, conversion cathode material, sulfur, can work synergistically in a single electrolyte and in the same potential range. We further show that interconnected sulfur/ TiS_2 hybrid foams created by thermal reaction of Ti metal foams and S_8 can be used to create 3D hybrid cathode materials in which sulfur is infused into porous TiS_2 foams. In galvanostatic electrochemical cycling studies the 3D hybrid cathodes demonstrate high areal specific capacity ($9\text{mAh}/\text{cm}^2$) and high retention ratio even at a relatively large areal mass loading of $\sim 40\text{mg}$ sulfur/ cm^2 , approximately 20 times higher than that used in most reports. The exceptional performance of sulfur infused TiS_2 foam appears to originate from four principal sources: i) TiS_2 enhances both the electronic and ionic conductivity of the hybrid system; ii) TiS_2 anchors strongly to sulfur reduction products in the cathode and thereby limits soluble LiPS loss to the electrolyte during extended cycling; iii) Despite their very different electrochemical reactions with Li, TiS_2 and sulfur work truly synergistically: sulfur does not hinder the intercalation of Li in TiS_2 and helps to increase the capacity and TiS_2 enhances the rate capability; iv) the absence of electrochemically inactive components, such as binder and metal current collector, further

increases the conductivity and energy density of the electrode; v) the porous 3D metal foam provides good access of electrolyte to the active materials, and at the same time, provides free space for volume change of sulfur. With further optimization, this structure shows significant potential toward for the practical application. This study also paves the way for exploration of other designs of S_8/TiS_2 and other hybrid cathode configurations that utilize active nanostructures in different topologies, including TiS_2 nanosheets, nanotubes, or nanospheres.

Acknowledgement

The authors acknowledge support of the National Science Foundation Partnerships for Innovation Program (Grant No. IIP-1237622). This research also used computational resources of the Texas Advanced Computing Center under contracts No. TG-DMR050028N and No. TG-DMR140067. Electron microscopy, X-ray diffraction, X-ray photoelectron spectroscopy facilities and optical spectrometers available through the Cornell Center for Materials Research (CCMR) were used for this work (NSF Grant DMR-1120296).

References

1. J. M. Tarascon and M. Armand, *Nature*, 2001, 414, 359-367.
2. Y.-G. Guo, J.-S. Hu and L.-J. Wan, *Adv. Mater.*, 2008, 20, 2878-2887.
3. M. S. WHITTINGHAM, *Science*, 1976, 192, 1126-1127.
4. M. S. Whittingham, *Prog. Solid State Chem.*, 1978, 12, 41-99.
5. M. S. Whittingha and A. J. Jacobson, *J. Electrochem. Soc.*, 1981, 128, 485-486.
6. X. Ji, K. T. Lee and L. F. Nazar, *Nat. Mater.*, 2009, 8, 500-506.
7. Z. Yang, J. Guo, S. K. Das, Y. Yu, Z. Zhou, H. D. Abruña and L. A. Archer, *J. Mater. Chem. A*, 2013, 1, 1433-1440.
8. J.-Q. Huang, Q. Zhang, H.-J. Peng, X.-Y. Liu, W.-Z. Qian and F. Wei, *Energy Environ. Sci.*, 2014, 7, 347-353.
9. L. Ma, K. E. Hendrickson, S. Wei and L. A. Archer, *Nano Today*, 2015, 10, 315-338.
10. L. Ji, M. Rao, H. Zheng, L. Zhang, Y. Li, W. Duan, J. Guo, E. J. Cairns and Y. Zhang, *J. Am. Chem. Soc.*, 2011, 133, 18522-18525.
11. H. Wang, Y. Yang, Y. Liang, J. T. Robinson, Y. Li, A. Jackson, Y. Cui and H. Dai, *Nano Lett.*, 2011, 11, 2644-2647.
12. Z. Wei Seh, W. Li, J. J. Cha, G. Zheng, Y. Yang, M. T. McDowell, P.-C. Hsu and Y. Cui, *Nat. Comm.*, 2013, 4, 1331.
13. T. Xu, J. Song, M. L. Gordin, H. Sohn, Z. Yu, S. Chen and D. Wang, *ACS Appl. Mater. Interfaces*, 2013, 5, 11355-11362.
14. L. Hu, F. La Mantia, H. Wu, X. Xie, J. McDonough, M. Pasta and Y. Cui, *Adv. Energy Mater.*, 2011, 1, 1012-1017.
15. J.-S. Kim, T. H. Hwang, B. G. Kim, J. Min and J. W. Choi, *Adv. Funct. Mater.*, 2014, 24, 5359-5367.
16. J. Gao and H. D. Abruña, *J. Phys. Chem. Lett.*, 2014, 5, 882-885.
17. Z. Li, Y. Jiang, L. Yuan, Z. Yi, C. Wu, Y. Liu, P. Strasser and Y. Huang, *ACS Nano*, 2014, 8, 9295-9303.

18. H. Ye, Y.-X. Yin, S. Xin and Y.-G. Guo, *J. Mater. Chem. A*, 2013, 1, 6602-6608.
19. S. Xin, L. Gu, N.-H. Zhao, Y.-X. Yin, L.-J. Zhou, Y.-G. Guo and L.-J. Wan, *J. Am. Chem. Soc.*, 2012, 134, 18510-18513.
20. J. Schuster, G. He, B. Mandlmeier, T. Yim, K. T. Lee, T. Bein and L. F. Nazar, *Angew. Chem. Int. Ed.*, 2012, 51, 3591-3595.
21. Y. Zhao, W. Wu, J. Li, Z. Xu and L. Guan, *Adv. Mater.*, 2014, 26, 5113-5118.
22. L. Sun, M. Li, Y. Jiang, W. Kong, K. Jiang, J. Wang and S. Fan, *Nano Lett.*, 2014, 14, 4044-4049.
23. X.-Q. Zhang, Q. Sun, W. Dong, D. Li, A.-H. Lu, J.-Q. Mu and W.-C. Li, *J. Mater. Chem. A*, 2013, 1, 9449-9455.
24. L. Ji, M. Rao, S. Aloni, L. Wang, E. J. Cairns and Y. Zhang, *Energy Environ. Sci.*, 2011, 4, 5053.
25. Z. Yuan, H.-J. Peng, J.-Q. Huang, X.-Y. Liu, D.-W. Wang, X.-B. Cheng and Q. Zhang, *Adv. Funct. Mater.*, 2014, 24, 6105-6112.
26. B. Ding, C. Yuan, L. Shen, G. Xu, P. Nie, Q. Lai and X. Zhang, *J. Mater. Chem. A*, 2013, 1, 1096-1101.
27. J. Z. Wang, *J. Power Sources*, 2011, 196, 7030-7034.
28. L. Yin, J. Wang, F. Lin, J. Yang and Y. Nuli, *Energy Environ. Sci.*, 2012, 5, 6966.
29. N. Jayaprakash, J. Shen, S. S. Moganty, A. Corona and L. A. Archer, *Angew. Chem. Int. Ed.*, 2011, 50, 5904-5908.
30. W. Zhou, Y. Yu, H. Chen, F. J. DiSalvo and H. D. Abruña, *J. Am. Chem. Soc.*, 2013, 135, 16736-16743.
31. L. Ma, H. Zhuang, Y. Lu, S. S. Moganty, R. G. Hennig and L. A. Archer, *Adv. Energy Mater.*, 2014, 4, 1400390.
32. Y. J. Choi, B. S. Jung, D. J. Lee, J. H. Jeong, K. W. Kim, H. J. Ahn, K. K. Cho and H. B. Gu, *Phys. Scripta*, 2007, T129, 62-65.
33. R. Demir-Cakan, M. Morcrette, F. Nouar, C. Davoisne, T. Devic, D. Gonbeau, R. Dominko, C. Serre, G. Ferey and J. M. Tarascon, *J. Am. Chem. Soc.*, 2011, 133, 16154-16160.
34. S. Evers, T. Yim and L. F. Nazar, *J. Phy. Chem. C*, 2012, 116, 19653-19658.

35. X. Ji, S. Evers, R. Black and L. F. Nazar, *Nat. Comm.*, 2011, 2, 325.
36. K. E. Hendrickson, L. Ma, G. Cohn, Y. Lu and L. A. Archer, *Adv. Sci.*, 2015, 2, 1500068.
37. J. Song, T. Xu, M. L. Gordin, P. Zhu, D. Lv, Y.-B. Jiang, Y. Chen, Y. Duan and D. Wang, *Adv. Funct. Mater.*, 2014, 24, 1243-1250.
38. N. A. Cañas, S. Wolf, N. Wagner and K. A. Friedrich, *J. Power Sources*, 2013, 226, 313-319.
39. M. Cuisinier, P.-E. Cabelguen, S. Evers, G. He, M. Kolbeck, A. Garsuch, T. Bolin, M. Balasubramanian and L. F. Nazar, *J. Phys. Chem. Lett.*, 2013, 4, 3227-3232.
40. M. A. Lowe, J. Gao and H. D. Abruña, *RSC Adv.*, 2014, 4, 18347.
41. G. Kresse and J. Hafner, *Phys. Rev. B*, 1993, 47, 558-561.
42. G. Kresse and J. Furthmüller, *Phys. Rev. B*, 1996, 54, 11169-11186.
43. P. E. Blöchl, *Phys. Rev. B*, 1994, 50, 17953-17979.
44. G. Kresse and D. Joubert, *Phys. Rev. B*, 1999, 59, 1758-1775.
45. J. P. Perdew, K. Burke and M. Ernzerhof, *Phys. Rev. Lett.*, 1996, 77, 3865-3868.
46. K. Sánchez, P. Palacios and P. Wahnón, *Phys. Rev. B*, 2008, 78, 235121.
47. Z. W. Seh, J. H. Yu, W. Li, P. C. Hsu, H. Wang, Y. Sun, H. Yao, Q. Zhang and Y. Cui, *Nat. Comm.*, 2014, 5, 5017.

Appendix

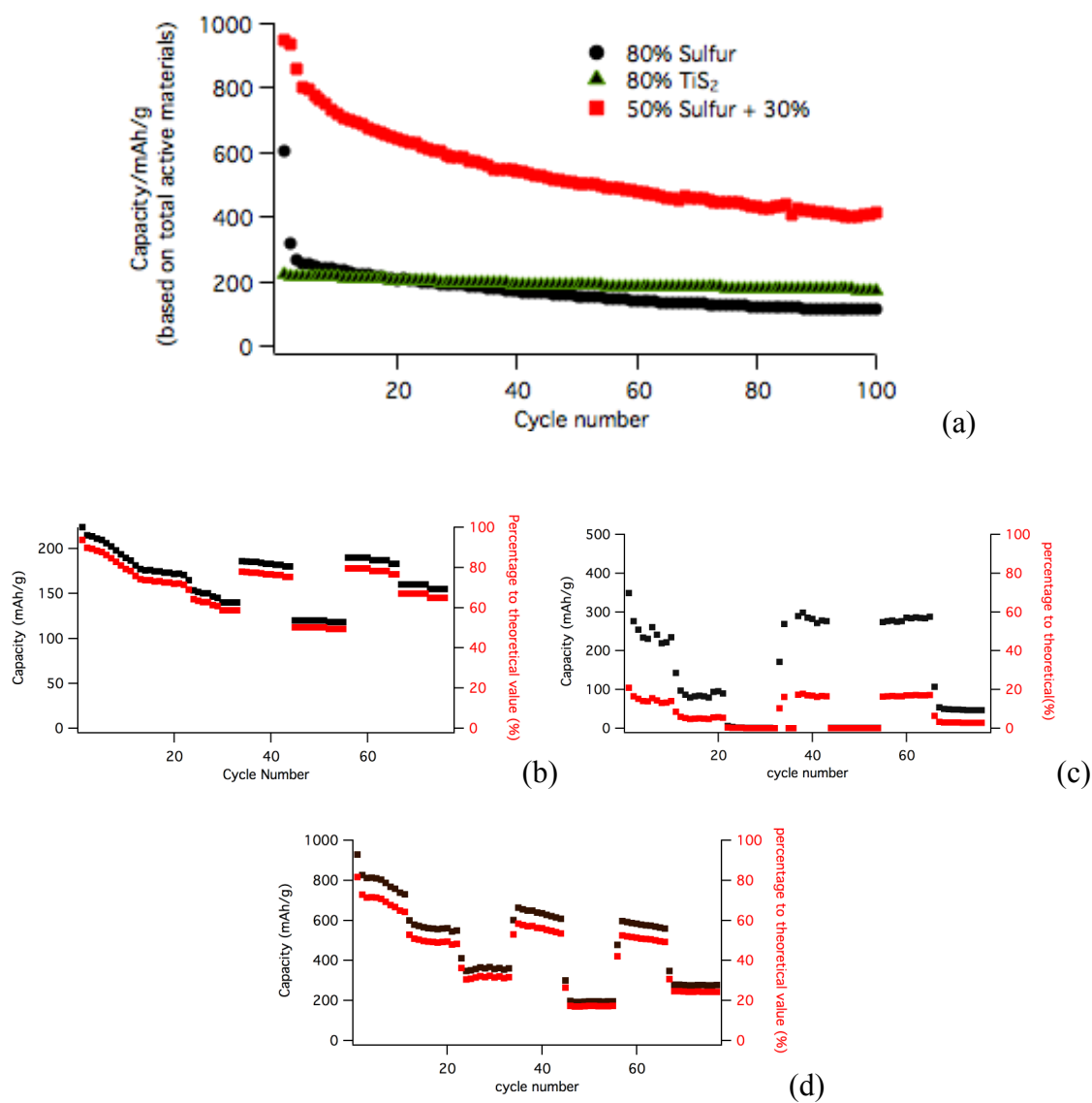


Figure S4.1 (a) Cycling performance of TiS₂, sulfur and TiS₂/S₈ hybrid electrode at 0.1C. Performance of (b) TiS₂ electrode, (c) sulfur electrode (d) TiS₂/S₈ hybrid cycled at various current rates (0.1C, 0.2C, 0.5C, 0.1C, 1C, 0.1C, 0.2C).

Table S4.1 Comparison of the performance of different cathode materials.

Cathode materials	First discharge capacity (mAh/g)*	Capacity after 30 cycles (mAh/g)*	Degradation rate per cycle (%)	Utilization rate(%)+
80% Sulfur cathode	603	189	2.3	36
50% Sulfur + 30%TiS ₂ cathode	950	600	1.2	84

* The capacity is calculated based on the weight of the total active materials.

+ Utilization rate = Experimental Capacity/Theoretical Capacity.

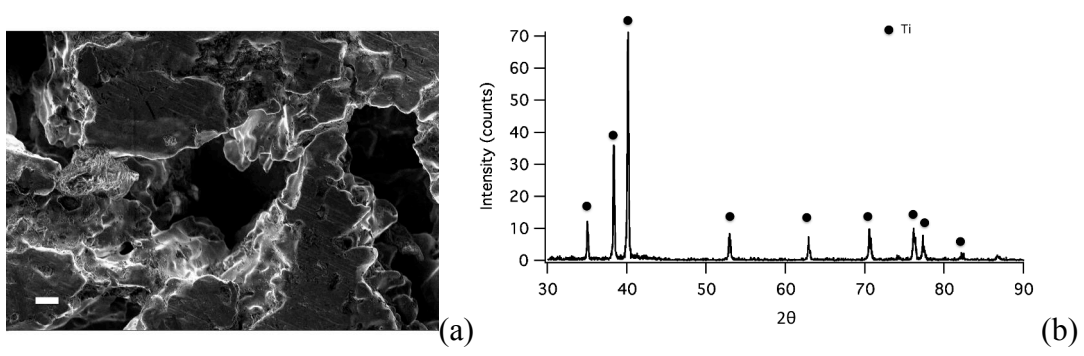


Figure S4.2 (a) SEM of Ti metal foam. Scale bar= 20 μm .(b) XRD analysis of Ti metal foam.

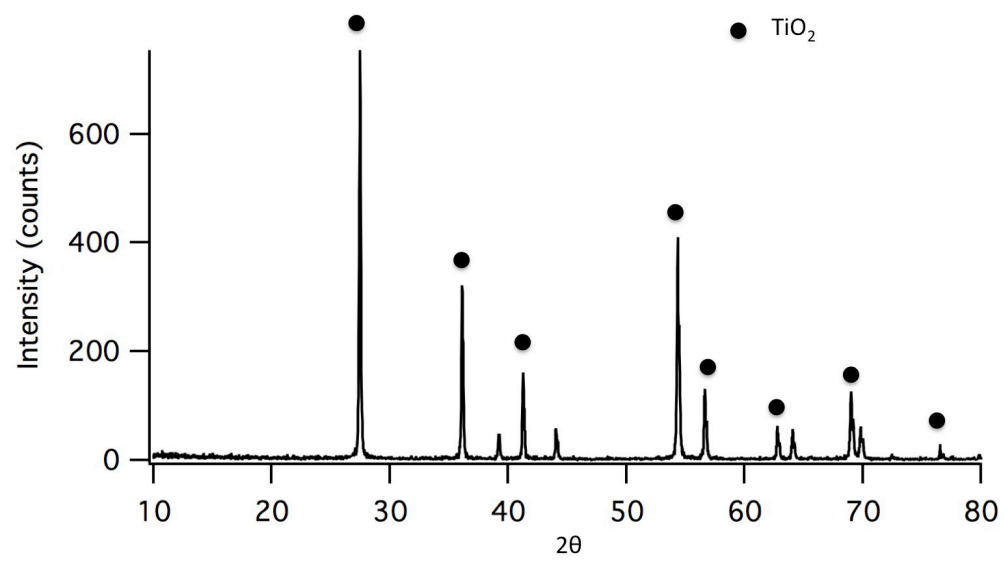


Figure S4.3 XRD analysis of the TGA products.

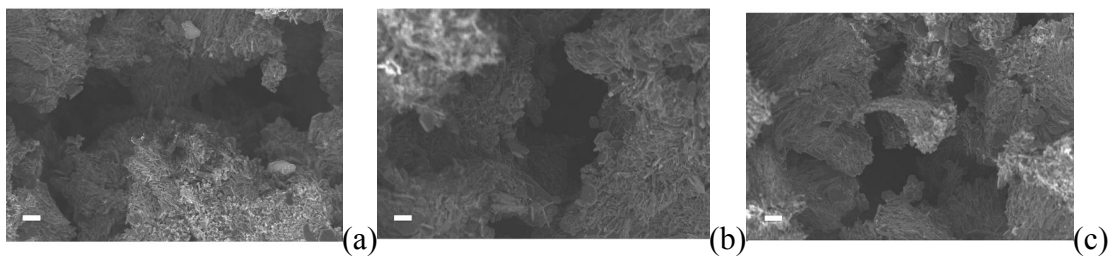


Figure S4.4 SEM images of (a)TSF5; (b)TSF10; (c) TSF15. Scale bar=20 μm .

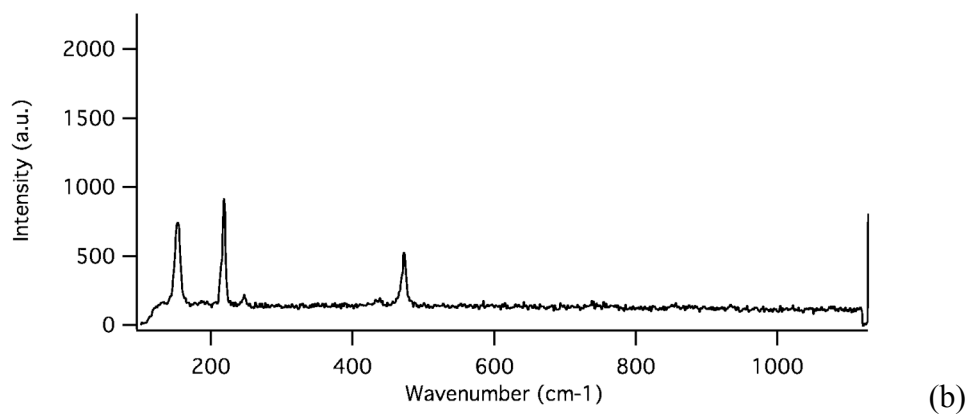
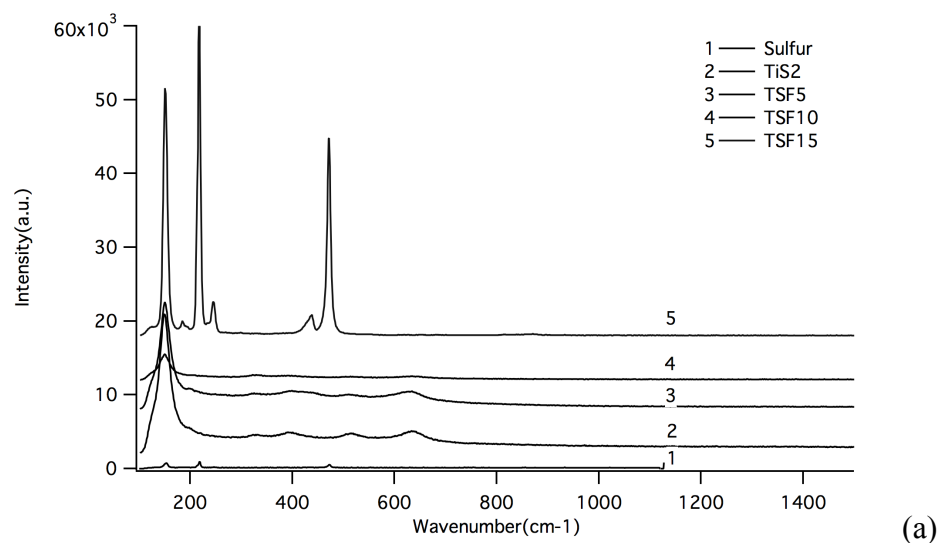


Figure S4.5 (a) Comparison of Raman spectra of 1. Sulfur powder. 2. TiS₂ powder. 3. TSF5. 4. TSF10. 5. TSF15. (b) Zoom-in spectra of sulfur.

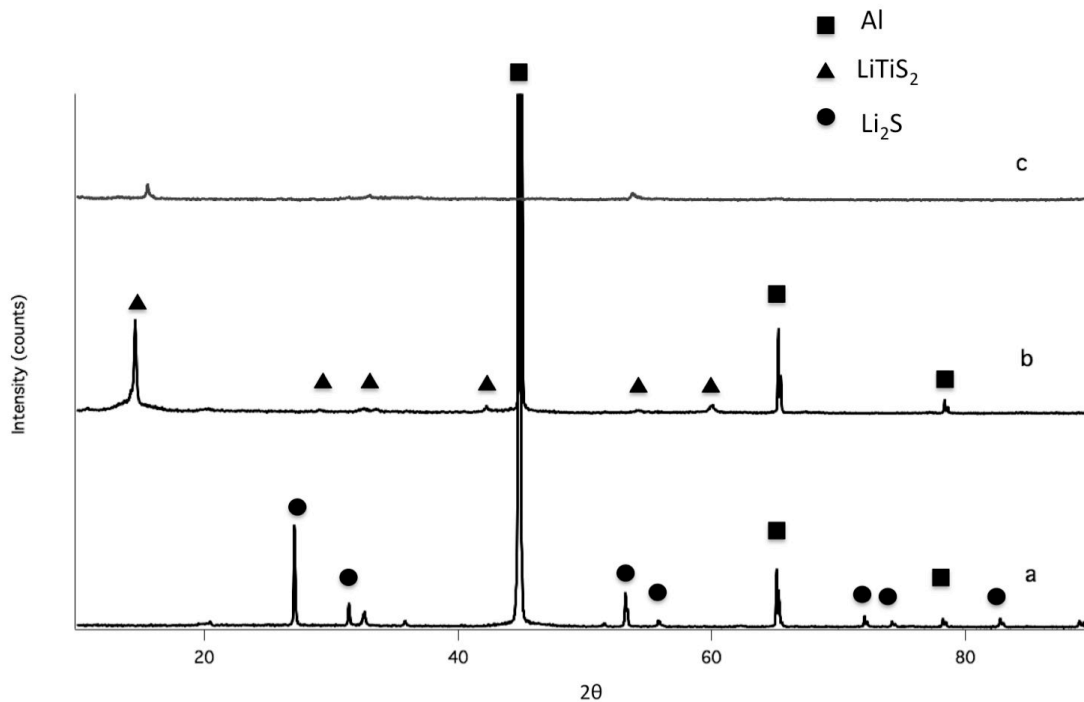
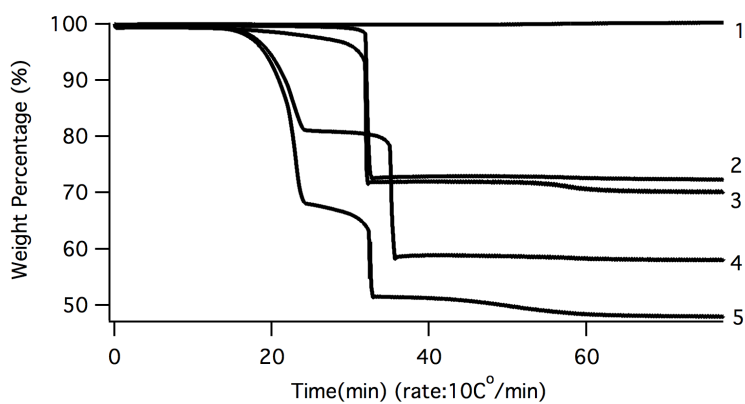


Figure S4.6 XRD analysis of the discharge products of (a) Sulfur electrode. (b) TiS₂ electrode. (c) TSF15.

Method 4.1

Method to determine content of Sulfur, TiS₂ and Ti metal content by using Thermogravimetric analysis (TGA).



1. Ti metal
2. TiS₂
3. TSF5
4. TSF10

5. TSF15

Use curve4 as an example. Set the percentage% of sulfur, TiS_2 and Ti as x, y, z respectively.

$$x+y+z=100$$

$$y+z=80$$

$$y \cdot 79.866(\text{TiO}_2)/111.997(\text{TiS}_2)+z=59$$

$$x=20;$$

$$y=73;$$

$$z=7.$$

Method 4.2

Estimation of the capacity based on the mass of the whole electrode

The areal weight with 4.7 mg/cm^2 of Al current collector is used here to calculate S wt% in total cathode weight. For example, in reference 6, sulfur loading is 1.13 mg/cm^2 , percentage of sulfur in the electrode slurry is 59 wt% and a capacity $\sim 1100 \text{ mAh/g}$ is obtained in 20th cycle.

$$\text{Capacity based on the whole electrode} = \frac{1100 \text{ mAh/g} \cdot 1.13 \text{ mg/cm}^2}{1.13 \text{ mg/cm}^2 / 0.59 + 4.7 \text{ mg/cm}^2} = 181 \text{ mAh/g}$$

CHAPTER 5

Highly conductive, sulfonated UV-crosslinked separators for Li-S battery

5.1 Abstract

Metal (based on Li, Na, Mg, or Al)-sulfur battery are promising candidates for rechargeable electrochemical storage devices capable of high charge storage. However, the success of metal-sulfur battery technology calls for solutions of fundamental problems associated with the inherently complex chemistry of sulfur and polysulfide species in commonly used electrolytes. It is understood that the dissolution and shuttling of polysulfides induces rapid capacity degradation, poor cycling stability and low efficiency of the cells. Herein, we have designed a high-transference number membrane containing sulfonate groups, in which the PEG backbone and the SO_3^{2-} groups facilitate electrolyte wettability and Li^+ ion conduction while the negatively charged membrane will at the same time reject sulfur species (S_n^{2-}) due to the repulsive electrostatic interactions. Such unique characteristics are attractive in modifying both positively and negatively charged ion transport within the cell. The membrane was prepared by a facile UV-crosslinking method, and the property of the membrane is highly tunable to meet specific demands in various battery systems. Here we show one example of its application in Li-S battery, with a remarkable cycling efficiency of above 98% in additive-free electrolyte.

5.2 Introduction

The demand for high-energy batteries is increasing rapidly due to their wide-range application in electronic devices, such as smartphones and laptops, as well as in the emerging field of electric vehicles.^{1, 2} Lithium sulfur batteries have been studied as one of the most promising batteries

because of their high theoretical specific capacity (1675 mAh/g) and energy density (2600 Wh/kg).^{3, 4} The theoretical capacity is about eight times higher than the maximum value for commercial lithium-ion cathodes (200 mAh/g) based on nickel cobalt aluminum (NCA) materials.^{5, 6} It is also more economically efficient because sulfur is an inexpensive (\$0.02 per g) and earth-abundant element, in comparison to lithium-ion battery cathodes with price too high to sustain the commercial viability of electrified transportation.^{7, 8}

However, the success of lithium sulfur battery technology calls for solutions to major obstacles, such as the poor conductivity of sulfur and its discharge products, and the large volume contraction and expansion of sulfur that accompanies its redox reaction with lithium.^{3, 9} In addition, the inherently complex chemistry of lithium polysulfide (LiPS) species commonly used electrolytes causes capacity fading, low efficiency and poor cycleability. Specifically, the higher order LiPS (Li_2S_x , $x > 2$) can dissolved into the liquid electrolyte, and can travel between the electrodes and erode both the cathode and anode, which is termed as the “shuttling” of LiPS.^{10, 11}

Many efforts have been made to immobilize the polysulfide anion in Li-S cell. A variety of carbon materials with special structure were used in cathode,^{5, 10, 12} which act not only as the electrically conductive components but also provide a physical barrier to inhibit the transportation of lithium polysulfides. Additives are also designed to act as polysulfide reservoirs by sequestering LiPS through chemical interaction between LiPS and the cathode surface.¹³⁻¹⁵ A combination of physical barrier and thermal sequestering of LiPS proves to be an efficient strategy for stable performance of sulfur cathode.^{16, 17} However, studies show that there is always a certain amount of LiPS that dissolves into the electrolyte during battery cycling even if the cathode’s binding affinity for LiPS is large.¹⁶ Also the high reactivity lithium metal in liquid

electrolyte calls for a 'clean' electrolyte sans any corrosive species. Thus, it is reasonable to conclude that a way to effectively suppress or even eliminate the polysulfide shuttle effect is desired for high performance Li-S batteries.

Ion selective membranes are attractive candidates for localizing polysulfide diffusion on the cathode side and therefore, preventing the shuttling of LiPS. Nafion ionomer has been used for this purpose in several Li-S studies.¹⁸⁻²¹ Nafion is a copolymer of tetrafluoroethylene and sulfonate terminated perfluoro vinyl ether, and it has shown excellent stability and high proton conductivity.²² When serving as a membrane, the sulfonate-terminated perfluoroalkyl ether pendant groups on Nafion will reject negative ions (S_n^{2-}) due to their unfavourable coulombic interactions.²³ Nafion was firstly studied as a separator or binder for the battery in some Li-ion studies^{19, 24, 25}, where the ionic conductivity and swelling behavior of lithiated Nafion ionomer was investigated. The ionomer swollen with mixed solvents of propylene carbonate (PC) and ethylene carbonate (EC) shows ionic conductivity of $8.18 \times 10^{-5} \text{ S cm}^{-1}$ at 25 °C.¹⁹ Lu et al. applied the nanoporous lithiated Nafion membrane in lithium metal battery and found that the high transference number membrane has the ability for promoting uniform electrodepositing and stopping dendrite proliferation in lithium/lithium symmetric cells. Jin et al. applied lithiated Nafion ionomer film as a functional separator for lithium sulfur cells.¹⁸ The lithium transference number (t_{Li^+}) of the electrolyte was calculated to be a near unity value of 0.986, indicating that only Li^+ could transport through the ionomer electrolyte. Also it is found from cyclic voltammetry that this electrolyte is chemically and electrochemically stable toward lithium and sulfur. In another study where Yu et al. also used lithiated Nafion film but with a advanced cathode structure containing carbon nanofiber current collector filled with dissolved lithium polysulfide.²⁰ It is found that upon saturation with the $LiCF_3SO_3 - DME/DOL$, the ionic

conductivity of the lithiated Nafion membrane is $\sim 1.0 \times 10^{-5} \text{ S cm}^{-1}$. In those studies the introduction of the Nafion membrane is effective in suppressing the shuttling of polysulfides between the cathode and anode.

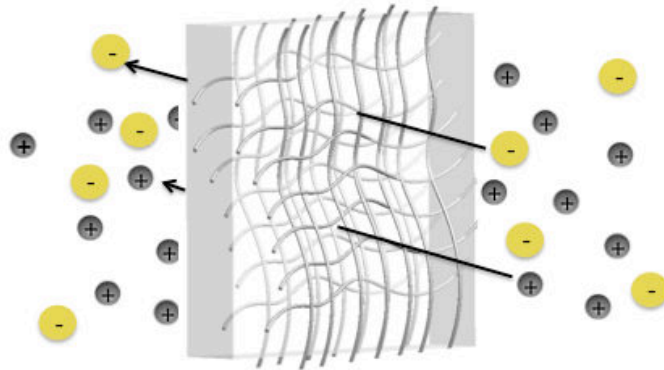
However despite its benefits, it is noticeable that Nafion has not been applied in commercial batteries, or even been as widely considered in battery research as would be expected. We interpret this phenomenon due to two limitations of Nafion: i) the ionic conductivity of Nafion is low in organic electrolytes. The low permeability of electrolyte within the Nafion membrane limits the battery operation to relatively low current rate; ii) the cost of Nafion is high, irrespective of being purchased in the form of solution or ionomer film.

The previous studies of applying Nafion as membrane in Li-S battery have verified the stability of lithium anode and sulfur cathode in the presence of sulfonate groups as well as its effectiveness in preventing the transport of polysulfide species through the separator. Inspired by the advantage of sulfonate groups and the desire to increase the conductivity of the membrane and to decrease the cost, we herein designed a highly conductive and ion-selective membrane for Li-S battery by a facile and low cost UV-crosslinking method. Free radical photopolymerization is a low cost, solvent free and energy saving technique, which is very well established for many applications, and is also conducive to scale up for large-scale manufacturing.

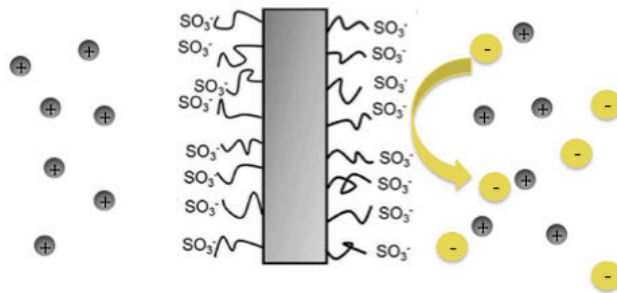
5.3 Results and discussion

Scheme 5.1 compares the interaction between ions in the electrolyte and different membrane systems in Li-S battery. As shown in **Scheme 5.1a**, in the cell where Celgard 2500 (a porous polypropylene polymer film) is used as the separator, both the lithium ion and polysulfides can

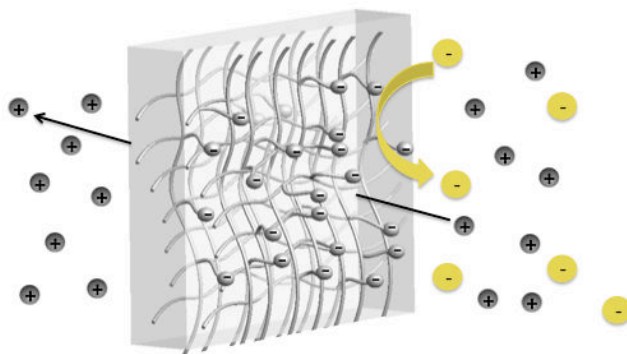
travel between the cathode and anode, resulting in the LiPS shuttling problem. In this case, the separator serves only as an electronic insulator and is not able to influence the ionic transport in the electrolyte. However, when an ion-selective membrane is introduced in the Li-S cell (**Figure 5.1b and 5.1c**), the polysulfide diffusion is localized on the cathode side due to the repulsive Colombic interaction between the polysulfide anion and the sulfonate groups on the membrane. In this way, the polysulfide shuttling is suppressed and the reaction between LiPS and lithium metal is prevented. In the specific case of Nafion, the Li^+ conduction is also limited due to the low permeability of Nafion and the low dielectric constant of the membrane backbone. As is mentioned in the introduction part, our goal is to design the membrane in **Figure 5.1c** in order to maintain the feature of sulfonate group but at the same time to increase the Li^+ conduction through the membrane to facilitate high performance Li-S battery.



(a) Celgard



(b) Nafion



(c) Membrane in this work

Figure 5.1 Different membrane systems interact with ions in the electrolyte.

Specifically, the membrane is made of copolymerization of poly(ethylene glycol) dimethacrylate (PEGDMA) and the vinylsulfonic acid salt (VS) (procedure shown in **Figure 5.2**). PEGDMA provides a cross-linked network and the vinylsulfonic monomers can participate in the free radical polymerization and at the same time functionalize the backbones with sulfonate groups. The PEGDMA and vinylsulfonic acid sodium salt was dissolved in DMSO along with 4% methyl benzoylformate (MBF) photoinitiator. The polymerization reaction starts when the solution is exposed to UV light. PEGDMA is chosen due to its ability to form a cross-linked branched network: each PEGDMA chain can covalently link to up to four other PEGDMA chains through radical polymerization in which the acrylate groups participate in an addition reaction.²⁶ As for the photoinitiator, MBF is used because MBF and its derivatives are one of the most widely used photoinitiators for radical polymerization of vinyl monomers.^{26, 27} Specifically, upon UV excitation MBF undergoes a fast bond cleavage to generate free radicals and initiates the addition reaction of the double bonds on PEGDMA and VS. This polymerization process is fast, efficient and energy saving. After the reaction, the membrane was harvested and washed with water to get rid of excess unreacted polymer and the solvent DMSO. The membrane was then subjected to lithium-ion exchange to replace sodium ions associated with sulfonate groups. The process is carried by treating the membranes with a solution of 2.0 M LiOH in deionized (DI) water at room temperature for 24 h under vigorous stirring, after which the resulting membrane is washed three times with DI water to remove the remaining LiOH.²³ The successful exchange of Na ion to Li ion is verified by EDX shown in **Figure S5.1**, where no Na signal is observed (the existence of lithium cannot be verified by EDX due to the machine limit). The membrane is then dried in an oven at 100 °C and transferred into the glove box for use.

The morphology of the membrane is shown in **Figure 5.3**, where the pure PEGDMA cross-

linked membrane show a transparent and smooth morphology while the membrane turn white and soft when VS is incorporated in the polymerization. The SEM images of the membrane (Figure 1c and 1d) also give information about the change in membrane structure and morphology. The pure PEGDMA membrane has an intercalating structure of the polymer chains/bundles, while when VS is introduced, it seems that the crosslink structure is not so well defined and it tends to be more particulate like compared to pure PEGDMA membrane. The overall appearance of the membrane under SEM is shown in **Figure S5.2**.

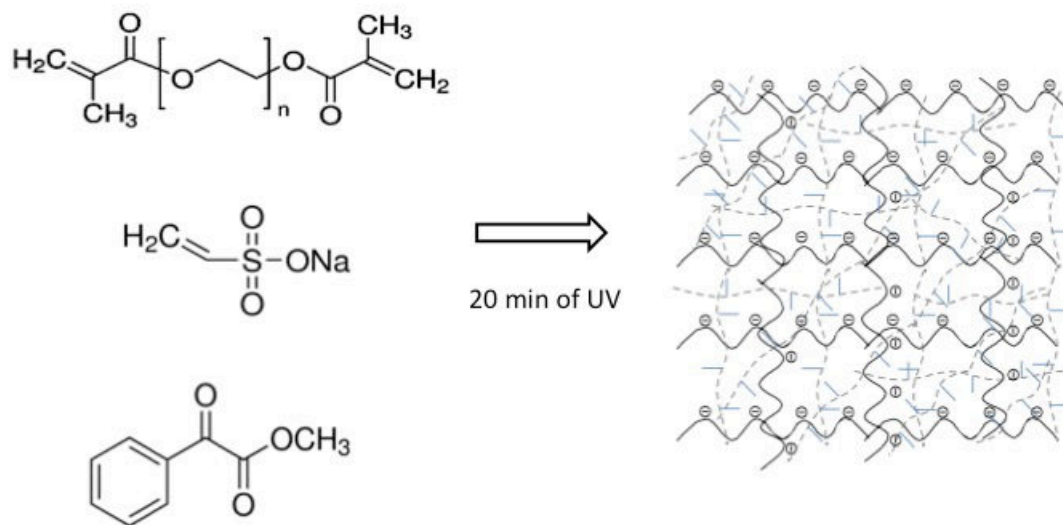


Figure 5.2 Preparation process of sulfonate group containing membrane.

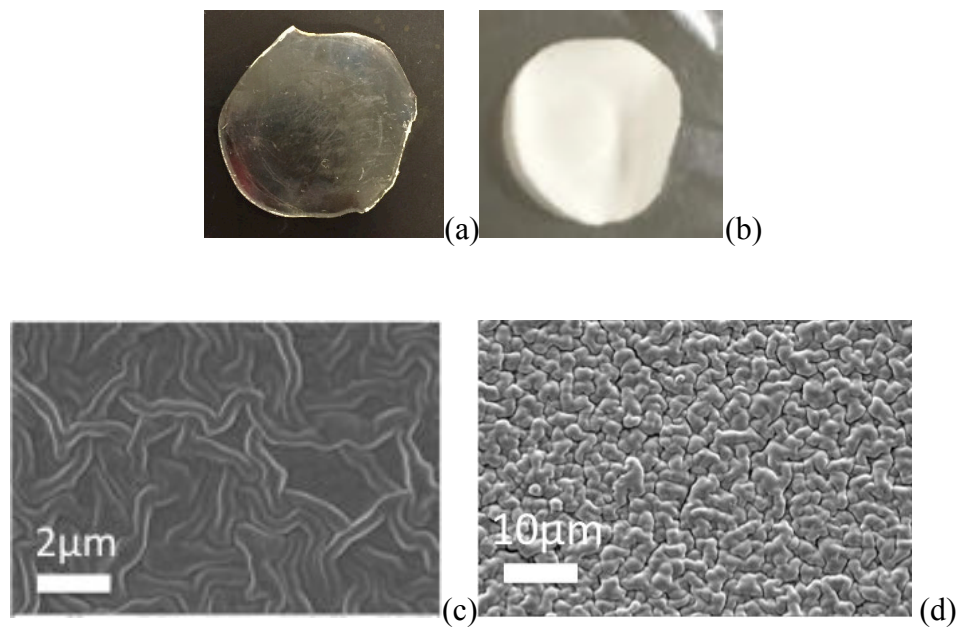


Figure 5.3 Morphology of the membranes. (a) photographic image of the pure PEGDMA membrane; (b) photographic image of the sulfonate group containing membrane; (c) SEM image of the pure PEGDMA membrane; (d) SEM image of the the sulfonate group containing membrane.

The successful crosslinking of PEGDMA and the incorporation of sulfonate groups by VS is verified by both FTIR and EDX. The FTIR spectra of the PEGDMA functionalized polymer and the PEGDMA-VS cross-linked membrane is shown in **Figure S5.3**. The untreated PEGDMA monomer has a C=O peak at 1714 cm^{-1} ; after crosslinking for 20min under UV exposure, the resulting polymer show C=O peak at 1728 cm^{-1} , while the other major characteristic peaks stay the same, which can be explained by the change in the chemical environment in the vicinity of the C=O bond. In PEGDMA monomer, the C=O bonds are conjugated with the adjacent C=C bonds; however when the crosslinking happens, the C=C bonds are converted to C-C bonds by addition polymerization, thus the C=O bonds are no longer conjugated, resulting in the observed shift in agreement with previous studies.^{26, 28} **Figure 5.4** compares the FTIR spectra of the membranes composed of pure PEGDMA cross-linked membrane and the one with VS incorporated.²⁶ The red FTIR spectra which corresponds to the membrane in which VS is incorporated shows an additional peak at 1175 compared to the pure PEGDMA case (black curve), and it corresponds to the S=O stretch in SO_3^{2-} group.²⁹⁻³¹ The successful incorporation of sulfonate group and the complete ion exchange of Na^+ to Li^+ were also verified by EDX on the membrane (**Figure S5.1**). The elements comprising membrane were detected by X-rays, which showed the existence of sulfur and the absence of sodium.

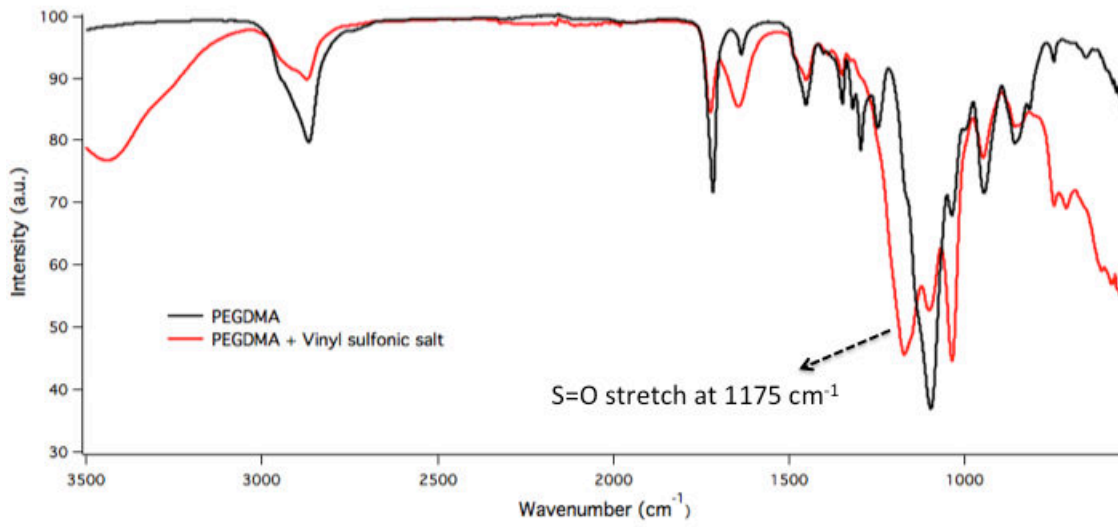


Figure 5.4 Confirmation of the incorporation of sulfonate group by FTIR and EDX.

The content of sulfonate groups within the cross-linked membrane is controlled by the ration of PEGDMA and VS in the reactants. Membranes with three different ratios (PEGDMA: VS = 10:2, 10:4 and 10:6 (w:w)) were prepared and the conductivity, mechanical properties, electrochemical performance as separator in Li-S cell were investigated. The names PV2, PV4, and PV6 are used to represent these three different membranes respectively. FTIR spectra confirm that in all cases the sulfonate groups is successful incorporated. The incorporated SO_3^{2-} groups increase in accordance with the increase of residues upon thermal decomposition of the membranes in TGA (**Figure S5.4**).

We next investigate the conductivity of the membranes as a separator in the battery. The dried membranes are soaked in organic solvents 1,3-dioxolane (DOL) and 1,2-dimethoxyethane (DME) with a volume ration of 1:1, which is a commonly used solvent in Li-S cell. The membrane containing the blank solvents already shows conductivity in the order of 10^{-4} S/cm (**Figure S5.5a**). **Figure 5.5** demonstrates the conductivity of the membranes soaked in DOL/DME solvents containing 1M lithium bis(trifluoromethanesulfone) imide (LiTFSI) as lithium salt. Remarkably the conductivity reach 10^{-3} S/cm at room temperature (1.14×10^{-3} S/cm at 20 °C), which is much higher than that of Nafion at 1.0×10^{-5} S cm^{-1} soaked in LiCF_3SO_3 - DME/DOL as reported recently²⁰ and is also among the highest values for single-ion conductors reported in the literature.³²⁻³⁵ We investigated the conductivity of Nafion soaked in LiTFSI – DME/DOL to have a straightforward comparison of the membrane we prepared (**Figure S5.5b**), it showed a much lower value at 3.05×10^{-5} S cm^{-1} at 20°C. The conductivity also increases with the increase content of sulfonate groups in the membranes. This can be explained by the 2 effects that SO_3^{2-} groups bring into the system: i) the SO_3^{2-} groups helps to increase the permeability of the membrane, resulting in a higher uptake of the electrolyte. ii) the SO_3^{2-} groups result in a

higher dielectric constant of the membrane thus the Li^+ dissociation and conduction is facilitated through the membrane. The higher conductivity compares to Nafion should benefit from the change of the backbone from the nonpolar tetrafluoroethylene to the oxygen rich PEGDMA. The wettability of the membranes is compared via TGA. As is shown in **Figure S5.6**, the membrane before and after being immersed in solvent (DOL/DME with v:v=1:1) was tested in TGA, which shows that PV6 can take up to 40% electrolyte, while Nafion can only adsorb ~10% electrolyte. DSC is also carried out to the membranes (**Figure S5.7**), and it demonstrated that with sulfonate group lower than that of PV6, the membranes have T_g well below room temperature ($\sim -50^\circ\text{C} - -60^\circ\text{C}$) and without melting point detected within the temperature range of cycling. It means that during battery operation at room temperature or higher, the polymer is outside the glassy regime and is non-crystalline, which is very important for lithium ion conduction. For PV6, a T_m is observed at $\sim 10^\circ\text{C}$, which should be attributed to the aggregation and crystallization of the ionic monomer when the sulfonate content is high enough. However, the peak disappeared when the membrane was soaked in the solvent (DOL/DME with v:v=1:1), meaning the crystallinity disappears within the swollen membranes. The XRD spectra (**Figure S5.8**) further indicate the absence of crystallinity of the membranes at room temperature.

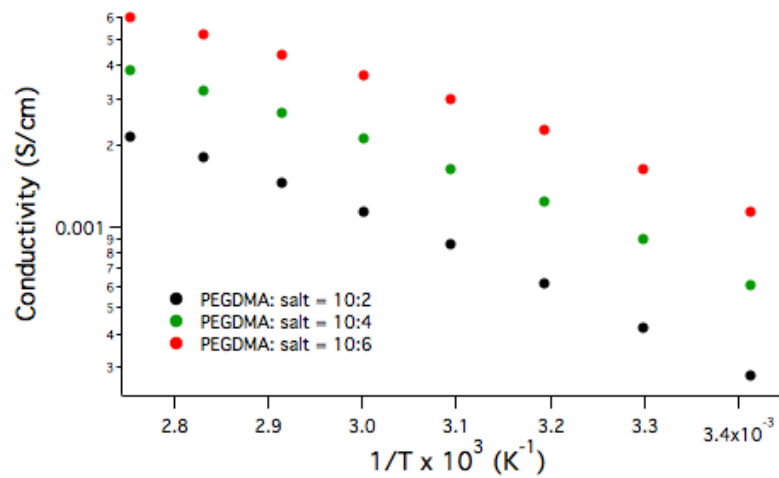


Figure 5.5 Conductivity of the membranes with different contents of sulfonate group.

Another important factor for choosing of sulfonate group is its ability to suppress polysulfide travelling through the membrane. The polysulfide anion permeability is investigated by its ability to diffuse through the membrane in ‘H-shaped’ liquid cells. Half of the cell is filled with 10mL blank DOL/DME solvents and another half is with 0.5M Li₂S₆ in 10mL DOL/DME solvents. These two parts were connected by either a routine Celgard separator or the ion selective membrane prepared by our method. The color change of the electrolyte over time was recorded by camera at intervals of 6h and is shown in **Figure 5.6**. This is one of the most straightforward ways to observe and track the diffusion of LiPS through the membrane due to the reddish color of LiPS in electrolyte. Overtime it is obvious that the LiPS in contact with the Celgard separator diffuse across the separator to the other side of the ‘cell’ and this is reflected in the color change of blank DOL/DME electrolyte from clear to reddish. In comparison, the blank electrolyte in the case of ion-selective membrane stays transparent, indicate that very little LiPS is able to travel through the sulfonate containing membrane.

Besides the direct visualization of the LiPS diffusion, the ability of the ion-selective membrane to suppress polysulfide anion diffusion is also verified by a quantitative parameter, i.e., the lithium transference number within an electrochemical cell. For this purpose, a lithium symmetric cell is assembled with two lithium metal pieces as electrodes and DOL/DME solvents containing 0.5M LiPS as electrolyte. The transference numbers were then determined using a conventional Bruce and Vincent method.³⁶ Specifically,

$$T_+ = \frac{I^s(\Delta V - I^o R_1^o)}{I^o(\Delta V - I^s R_1^s)}$$

Where ΔV is the potential applied across the cell, R_1^o and R_1^s are the initial and steady-state

resistances of the passivating layers, I^o and I^s are the initial and steady-state currents respectively. A small $\Delta V = 10$ mV is applied and the result is shown in **Figure 5.7a and 5.7b**, which shows the impedance and current change before and after polarization of the cell with Celgard separator (**Figure 5.7a**) and PV6 (**Figure 5.7b**). While the impedance increases after polarization in both case, the current drop in the cell with Celgard separator is much more dramatic than that with PV6. Using the equation for t_+ shown above, the transference number of the cell with Celgard is 0.29 while the one with PV6 is as high as 0.98, which is very close to unity, indicating that the ion conduction is mostly via Li^+ while polysulfides are unable to diffuse through the separator due to electrostatic interaction. The result is consistent with the visualization experiment shown in **Figure 5.6**.

Besides the polysulfide anions, we also investigated the effect of the membrane on lithium ion diffusion by cyclic voltammetry (CV). Specifically, the lithium ion diffusion coefficient was evaluated by CV scanning with different scan rates and with the help of Randles-Sevick equation,

$$i_p = 268600n^{1.5}AD^{1.5}C\nu^{0.5},$$

where i_p is the peak current, n is the number of electrons transferred in the redox reaction, A is electrode area, D is the diffusion coefficient, C is the concentration of ions and ν is the CV scan rate. Thus the diffusion coefficient can be calculated from the slope of the line i_p vs. $\nu^{0.5}$. **Figure S5.9a and S5.9b** show the CV curve of Li-S cells with Celgard and PV6 as separator respectively at different scan rates. **Table S5.1** summarizes the diffusion coefficients of lithium ion calculated using the redox peaks by using the method above. The lithium ion diffusion in PV6 is close to that of Celgard, indicating the lithium ion diffusion is not effected by the functional groups on the membrane when they provide ionic shielding for polysulfide ions.

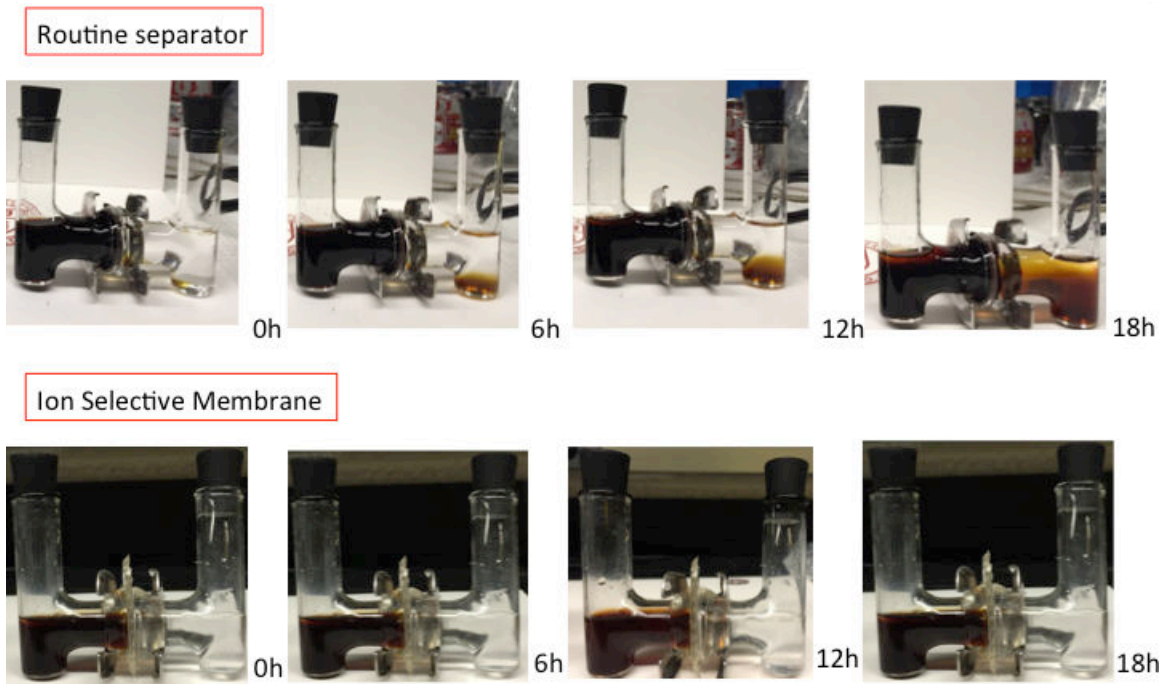


Figure 5.6 Visualization of the LiPS diffusion through different membrane systems.

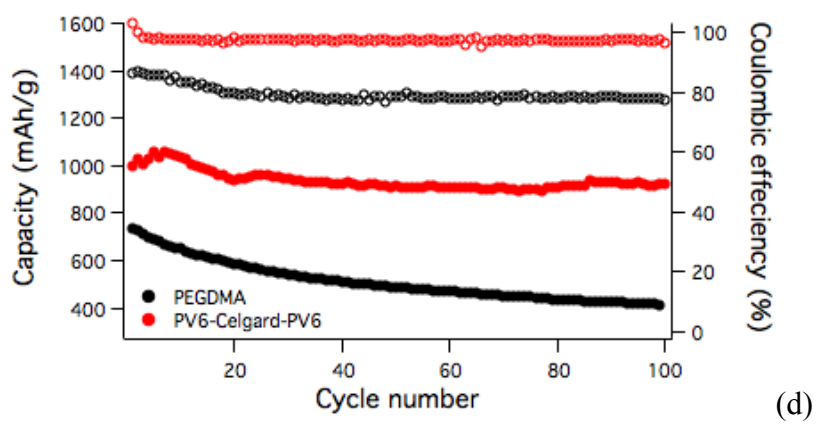
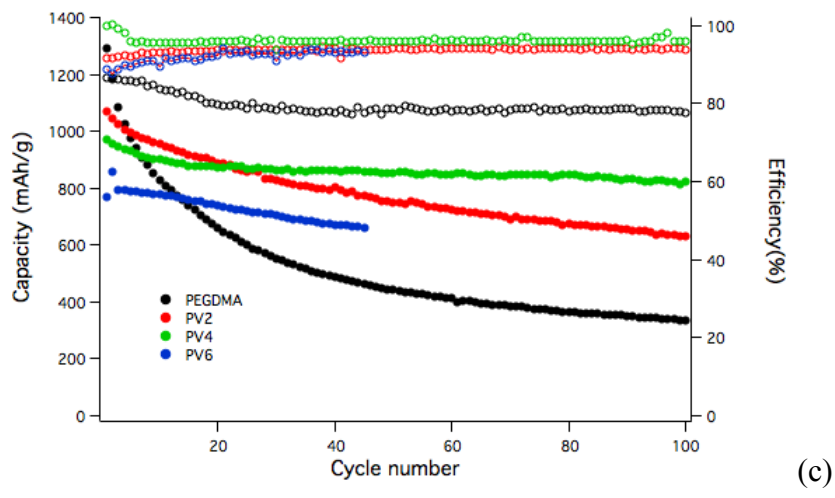
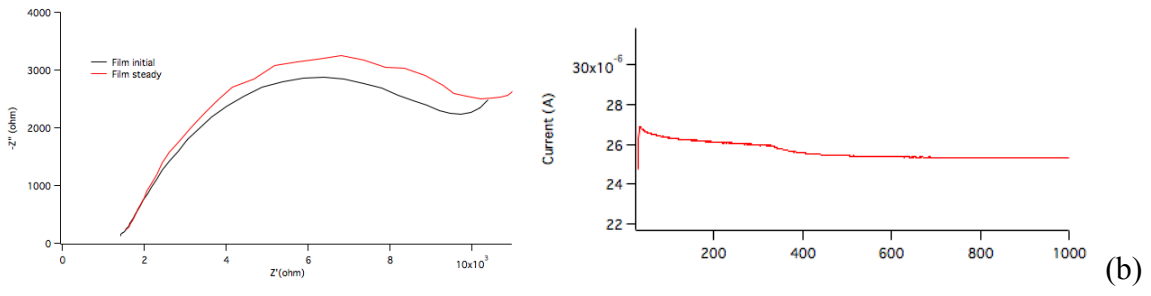
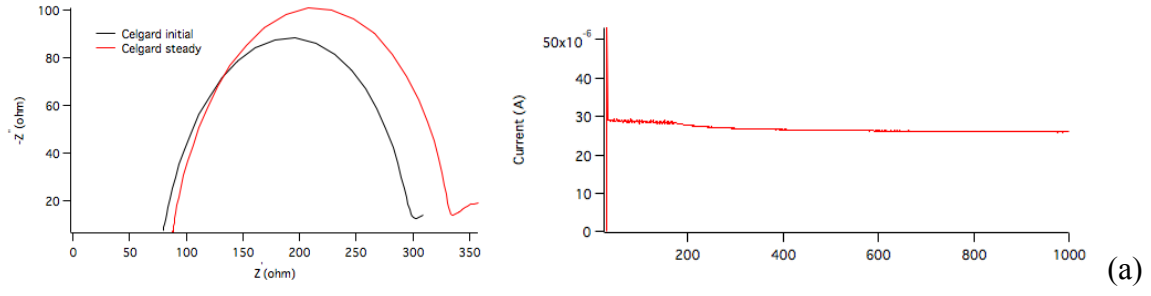


Figure 5.7 Electrochemical characterization and cycling performance: (a) and (b) show impedance and current change before and after polarization for transference number measurement for (a) Celgard (b) PV6 membranes respectively; (c) and (d) show cycling performance of the Li-S cells with the prepared membranes cycled at 0.5C with additive-free electrolyte.

After confirming its ability to facilitate lithium ion conduction and at the same time prevent polysulfide diffusion, the sulfonate containing membrane was used as a separator in Li-S cells and the performance at a current density of 0.5C is shown in **Figure 5.7c**. The sulfur cathode used in the Li-S cell is prepared by the method as is reported previously, where sulfur is loaded upon the polyethylenimine (PEI) attached CNT matrix. [16] The electrolyte utilized here is 1M LiTFSI in DOL/DME (v:v=1:1) without LiNO₃ addition. The black curve corresponds to the cell with pure PEGDMA crosslinked membrane. Severe capacity fading is observed over cycling with less than 400 mAh/g at 100th cycle, and it should be due to the LiPS shuttling or even the trapping of LiPS in the oxygen-rich membrane, which can interact with the LiPS species. In addition, the Coulombic efficiency of the cell is relatively low ~ 78%, indicating there is LiPS shuttling during cycling, resulting in passivation of lithium metal anode and the loss of active materials. However, once the sulfonate group is incorporated in the membrane, the cycling becomes much more stable. Moreover, the Coulombic efficiency reaches 96% - 97% when sulfonate group is present, further confirming its ability to localize LiPS diffusion near the cathode side. It is also noticed that the membrane with the higher sulfonate content doesn't necessarily lead to better performance. The one with the highest sulfonate content leads to cell failure after ~ 50 cycles. The cell was opened and PV6 was found to break over cycling, which should be attributed to the cell failure observed.

The mechanical property of the membranes was tested by DMA (Dynamic Mechanical Analysis), and the results are shown in **Figure S5.10**. Although all those membranes are free standing and can be used as separator in Li-S cell by itself, the failure of the cell at high sulfonate contents indicate that strong mechanical properties are desired. We thus design a sandwich-type membrane in which the core layer is Celgard but with PV6 coated on both sides. This structure

can take advantage of both the high modulus of Celgard and the single ion conductor we designed. As is shown in **Figure S5.11**, the membrane is still freestanding and highly flexible. More importantly, the mechanical property of the membrane is maintained with a modulus ~ 30 MPa, as strong as original Celgard membrane, and the modulus is much higher than the original PV6 membrane. The sandwich membrane was used as a separator in Li-S cell and the same additive-free electrolyte was applied, and the cycling performance is shown in **Figure 5.7d**. It is evident that compared to the one in **Figure 5.7c**, the cycleability is greatly improved when the sandwich design is used. Specifically, the cell can operate without failure for 100 cycles, with a high capacity ~ 1000 mAh/g and a high capacity retention rate of 92%. More importantly, with the presence of large amount of sulfonate groups, the Coulombic efficiency of the cell is above 98% for 100 cycles, which is a significant increase compared to the pure PEGDMA membrane. The result is remarkable because it shows the highest Coulombic efficiency in Li-S cells with an additive-free electrolyte.^{21,37} It is also significant because it shows that our method to prepare the highly conductive single ion conductor can be modified and applied to various energy storage systems.

5.4 Materials and Method

5.4.1 Preparation of the membranes

Poly(ethylene glycol) dimethacrylate (M_n 750) and vinylsulfonic acid sodium salt solution (25 wt.% in H_2O) were purchased from Sigma-Aldrich. DMSO is good solvent for both PEGDMA and VS, thus VS water solution was dried in the vacuum oven at $100^\circ C$ for 24h and then dissolved in Dimethyl sulfoxide (20 wt. % in DMSO). PEGDMA was added into the DMSO solution and stirred to form uniform solution. The mixture with an addition of 4% photoinitiator

methyl benzoylformate (MBF) was exposed to UV light (VMR UV-AC 115V ~60Hz 254/365nm) for 20 mins. After the reaction, the membrane was harvested and washed with water to get rid of unreacted polymer and the solvent DMSO. The ion exchange of Na^+ to Li^+ is carried out in a solution of 2.0M LiOH in deionized (DI) water at room temperature for 24 h under vigorous stirring, after which the resulting membrane is washed three times with DI water to remove the remaining LiOH. The membrane is then dried in over at 100 °C and kept in glove box before use.

5.4.2 Characterization of the membranes

The membranes were characterized using FTIR spectroscopy by using a Bruke Optics Vertex80v infrared spectrometer with air-sensitive samples tested in a vacuum-evacuated chamber. Melting transition behaviors were studied using a DSC Q2000 (TA instruments). Crystal structure was characterized using Scintag Theta-Theta X-ray Diffractometer (XRD). Thermogravimetric analysis (TGA) was used to determine the content of sulfonate groups and the solvent adsorption ability of the membranes. Morphologies of the membranes were studied using LEO 1550 FESEM (Keck SEM). Mechanical properties of the membranes were investigated by dynamic mechanical analysis (DMA) using a TA instrument DMA Q800. Impedance versus frequency was measured using a Novocontrol N40 broadband dielectric spectroscopy. Ionic conductivity as a function of frequency was also measured with a Novocontrol N40 broadband spectrometer fitted with a Quarto temperature control system.

5.4.3 Electrochemical Characterization

2030 coin-type cells were assembled using Lithium metal (0.75 mm. thick, Alfa Aesar) as the anode electrode, the prepared membranes as separator, a cathode with 80% as prepared PEI-

CNT/S composite, 10% Super-P Li carbon black from TIMCAL, and 10% poly(vinylidene difluoride) (PVDF, Sigma Aldrich) as binder in an excess of N-methyl-2-pyrrolidone in NMP, and electrolyte of 20uL 1M lithium bis(trifluoromethanesulfone) imide (LiTFSI) in DOL (1,3-dioxolane) : DME (1,2-dimethoxyethane) (v:v=1:1) for each cell. The sulfur loading per electrode is 1.2 mg/cm². The dried membrane was soaked in the same electrolyte for 24h before assembling in the cell. Cell assembly was carried out in an argon-filled glovebox (MBraun Labmaster). The room-temperature cycling characteristics of the cells were evaluated under galvanostatic conditions using Neware CT-3008 battery testers and electrochemical processes in the cells were studied by cyclic voltammetry using a CHI600D potentiostat.

5.5 Conclusion

In conclusion, we report a facile and efficient way to prepare high transference number membrane with sulfonate groups via UV-crosslinking. The membrane has high lithium ion conductivity and also prevents the polysulfide ion diffusion through, making it a high-performance separator in Li-S cell. The method used to prepare the membranes is highly tunable and applicable in various different battery systems. We demonstrate here a sandwich-type membrane combined with Celgard, and we believe a variety of designs can be made, such as the ceramic-polymer composite, which are currently being investigated in our lab.

References

1. M. Armand and J. M. Tarascon, *Nature*, 2008, 451, 652-657.
2. J. M. Tarascon and M. Armand, *Nature*, 2001, 414, 359-367.
3. L. Ma, K. E. Hendrickson, S. Wei and L. A. Archer, *Nano Today*, 2015, 10, 315-338.
4. X. Ji, K. T. Lee and L. F. Nazar, *Nat. Mater.*, 2009, 8, 500-506.
5. X. Ji and L. F. Nazar, *J. Mater. Chem.*, 2010, 20, 9821-9826.
6. M. S. WHITTINGHAM, *Science*, 1976, 192, 1126-1127.
7. G. Cohn, L. Ma and L. A. Archer, *J. Power Sources*, 2015, 283, 416-422.
8. K. E. Hendrickson, L. Ma, G. Cohn, Y. Lu and L. A. Archer, *Adv. Sci.*, 2015, 2, 1500068.
9. A. Manthiram, Y. Fu, S.-H. Chung, C. Zu and Y.-S. Su, *Chem. Rev.*, 2014, 114, 11751-11787.
10. N. Jayaprakash, J. Shen, S. S. Moganty, A. Corona and L. A. Archer, *Angew. Chem.*, 2011, 50, 5904-5908.
11. Y. Yang, G. Zheng and Y. Cui, *Chem. Soc. Rev.*, 2013, 42, 3018-3032.
12. H. Wang, Y. Yang, Y. Liang, J. T. Robinson, Y. Li, A. Jackson, Y. Cui and H. Dai, *Nano Lett.*, 2011, 11, 2644-2647.
13. J. Guo, Z. Yang, Y. Yu, H. D. Abruna and L. A. Archer, *J. Am. Chem. Soc.*, 2013, 135, 763-767.
14. L. Ma, S. Wei, H. L. Zhuang, K. E. Hendrickson, R. G. Hennig and L. A. Archer, *J. Mater. Chem. A*, 2015, 3, 19857-19866.
15. L. Ma, H. Zhuang, Y. Lu, S. S. Moganty, R. G. Hennig and L. A. Archer, *Adv. Energy Mater.*, 2014, 4, 1400390
16. L. Ma, H. Zhuang, S. Wei, K. Hendrickson, M. S. Kim, G. Cohn, R. G. Hennig and L. A. Archer, *ACS Nano*, 2016, 10, 1050-1059.
17. G. Zheng, Q. Zhang, J. J. Cha, Y. Yang, W. Li, Z. W. Seh and Y. Cui, *Nano Lett.*, 2013, 13, 1265-1270.
18. Z. Jin, K. Xie, X. Hong, Z. Hu and X. Liu, *J. Power Sources*, 2012, 218, 163-167.

19. H. Y. Liang, X. P. Qiu, S. C. Zhang, W. T. Zhu and L. Q. Chen, *J. Appl. Electrochem.*, 34, 1211-1214.
20. X. Yu, J. Joseph and A. Manthiram, *J. Mater. Chem. A*, 2015, 3, 15683-15691.
21. J.-Q. Huang, Q. Zhang, H.-J. Peng, X.-Y. Liu, W.-Z. Qian and F. Wei, *Energy Environ. Sci.*, 2014, 7, 347-353.
22. Y. Wang, K. S. Chen, J. Mishler, S. C. Cho and X. C. Adroher, *Appl. Energy*, 2011, 88, 981-1007.
23. Y. Lu, M. Tikekar, R. Mohanty, K. Hendrickson, L. Ma and L. A. Archer, *Adv. Energy Mater.*, 2015, 5, 1402073
24. M. Wang, F. Zhao and S. Dong, *J. Phys. Chem. B*, 2004, 108, 1365-1370.
25. R. R. Garsuch, D.-B. Le, A. Garsuch, J. Li, S. Wang, A. Farooq and J. R. Dahn, *J. Electrochem. Soc.*, 2008, 155, A721-A724.
26. B. Sania, 2012.
27. N.-S. Choi, Y. M. Lee, W. Seol, J. A. Lee and J.-K. Park, *Solid State Ion.*, 2004, 172, 19-24.
28. K. Y. Suh, J. Seong, A. Khademhosseini, P. E. Laibinis and R. Langer, *Biomaterials*, 2004, 25, 557-563.
29. C. R. Martins, G. Ruggeri and M.-A. De Paoli, *J. Braz. Chem. Soc.*, 2003, 14, 797-802.
30. A. C. T. Cursino, A. S. Mangrich, J. E. F. d. C. Gardolinski, N. Mattoso and F. Wypych, *J. Braz. Chem. Soc.*, 2011, 22, 1183-1191.
31. Z. P. Xu and P. S. Braterman, *J. Mater. Chem.*, 2003, 13, 268-273.
32. N. Matsumi, K. Sugai, M. Miyake and H. Ohno, *Macromolecules*, 2006, 39, 6924-6927.
33. M. Watanabe, Y. Suzuki and A. Nishimoto, *Electrochim. Acta*, 2000, 45, 1187-1192.
34. R. P. Doyle, X. Chen, M. Macrae, A. Srungavarapu, L. J. Smith, M. Gopinadhan, C. O. Osuji and S. Granados-Focil, *Macromolecules*, 2014, 47, 3401-3408.
35. R. Rohan, Y. Sun, W. Cai, K. Pareek, Y. Zhang, G. Xu and H. Cheng, *J. Mater. Chem. A*, 2014, 2, 2960-2967.
36. J. Evans, C. A. Vincent and P. G. Bruce, *Polymer*, 1987, 28, 2324-2328.

37. J.-Q. Huang, T.-Z. Zhuang, Q. Zhang, H.-J. Peng, C.-M. Chen and F. Wei, *ACS Nano*, 2015, 9, 3002-3011.

Appendix

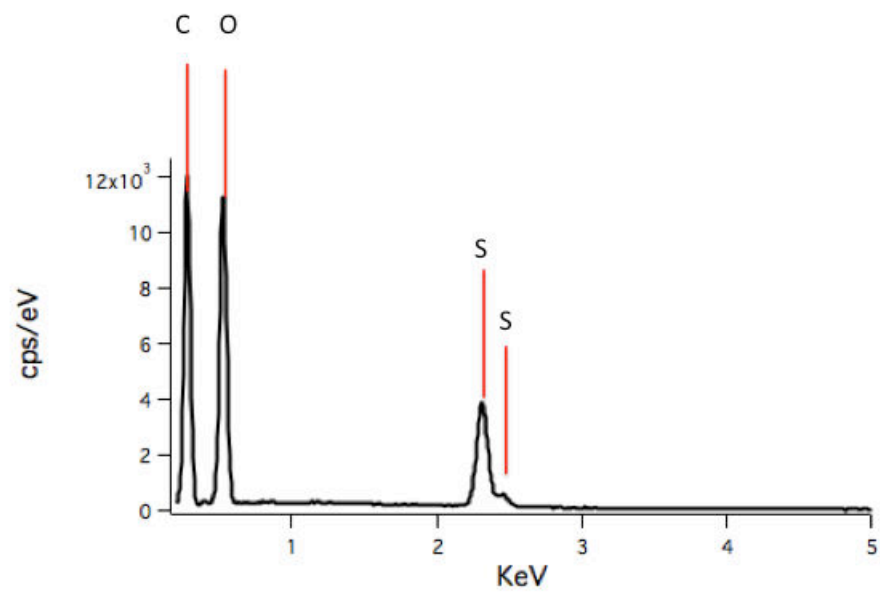


Figure S5.1 EDX of the membrane (PEGDMA:VS=10:2)

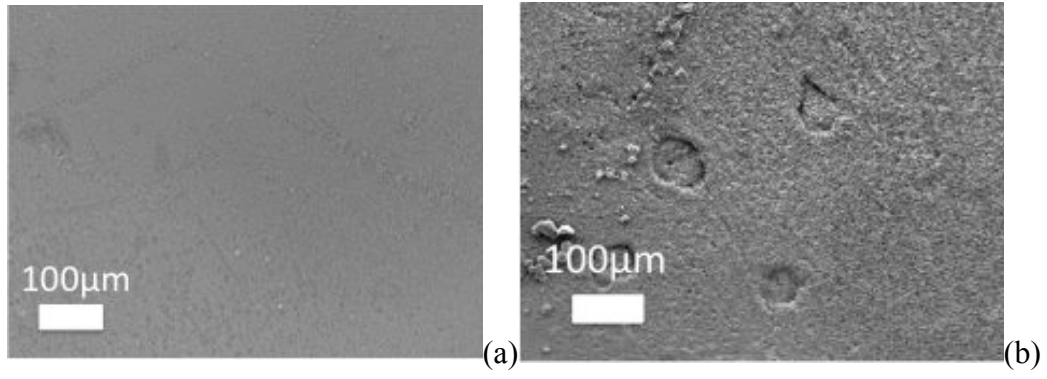


Figure S5.2 Zoom out SEM images of the membranes (a) PEGDMA membrane; (b) membrane with sulfonate groups.

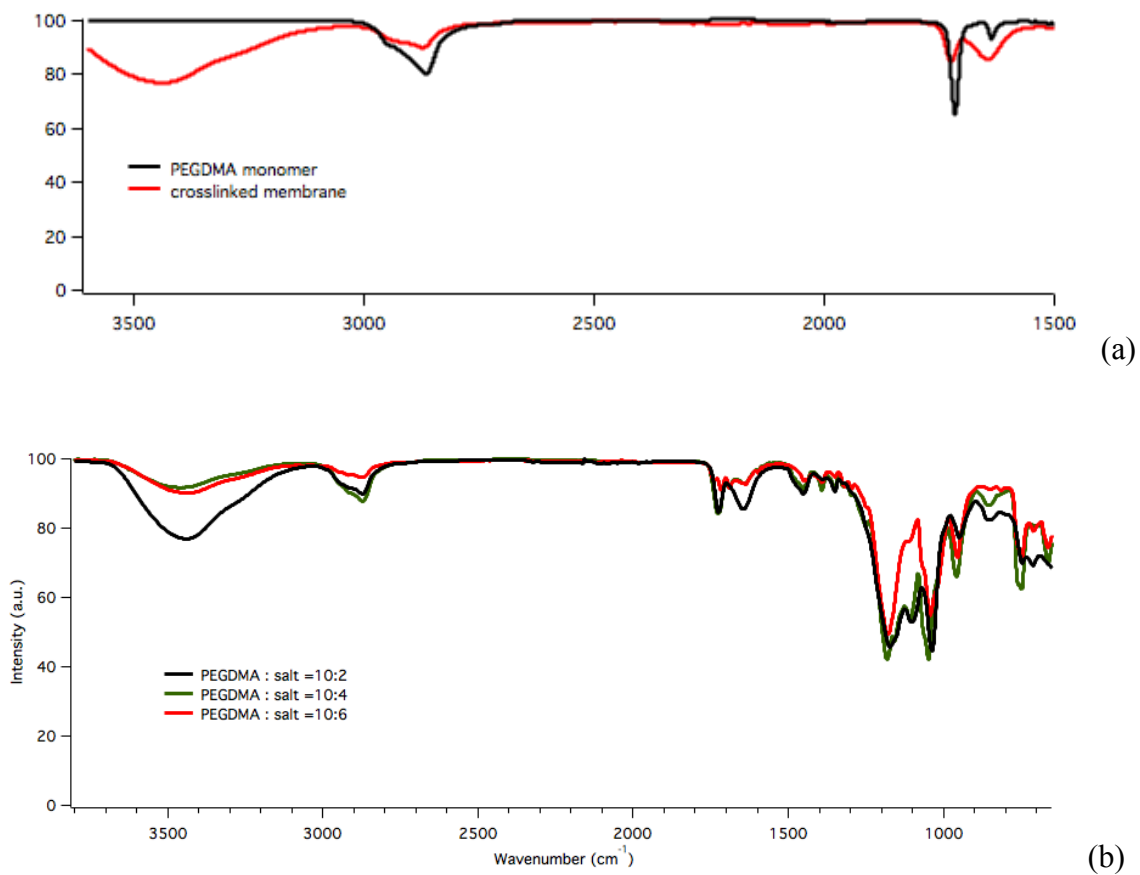


Figure S5.3 FTIR of the crosslinked membrane. (a) Zoom in FTIR of the PEGDMA monomer and the sulfonate containing cross-linked membrane. (b) FTIR of the cross-linked membrane with different content of sulfonate groups.

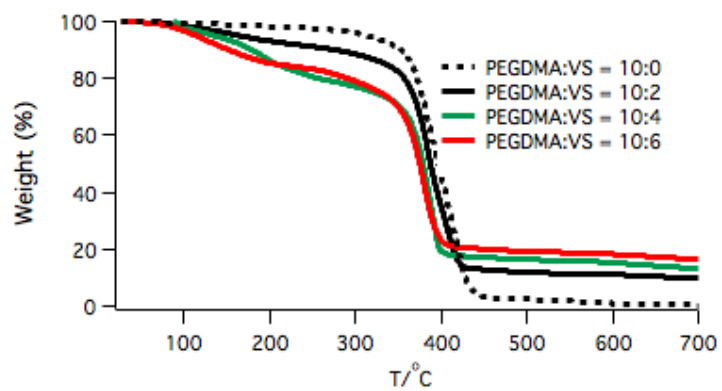


Figure S5.4 TGA of cross-linked membrane with different content of sulfonate groups.

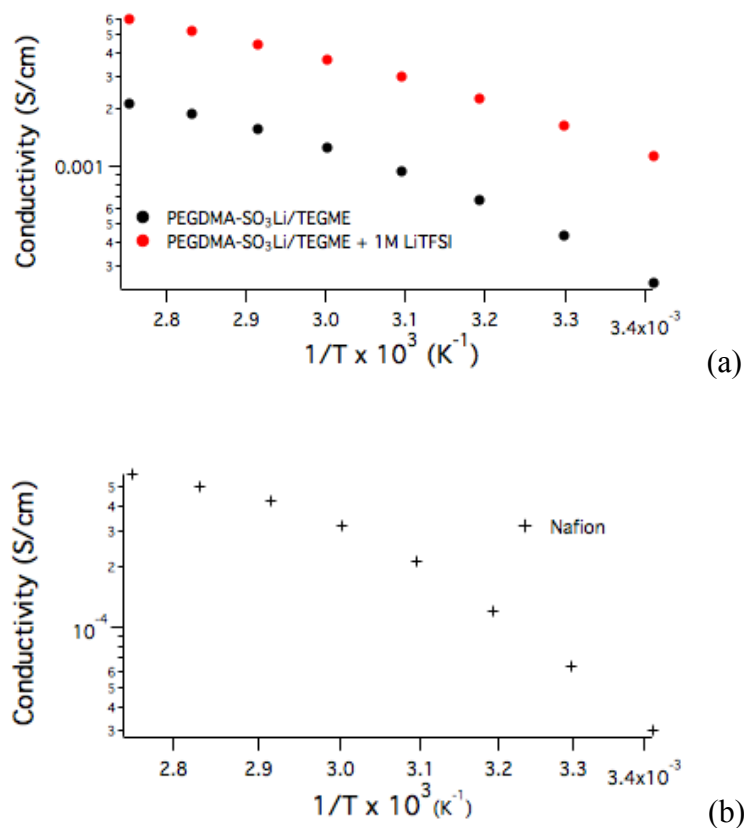


Figure S5.5 (a) Conductivity of the cross-linked membrane (PEGDMA:VS=10:6) soaked in blank DOL/DME electrolyte (black) and in LiTFSI containing electrolyte (red); (b) conductivity of Nafion soaked in the same electrolyte.

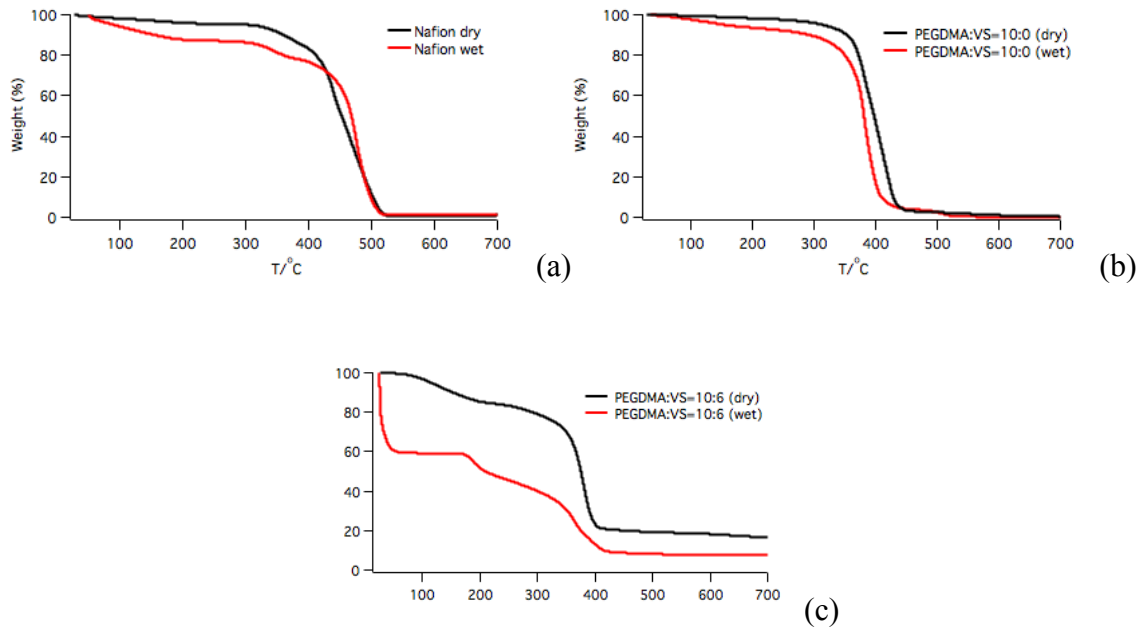
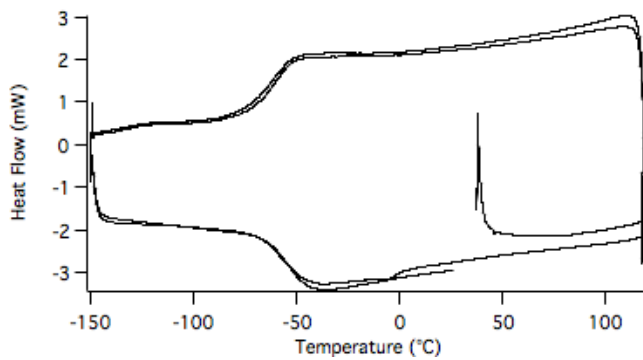
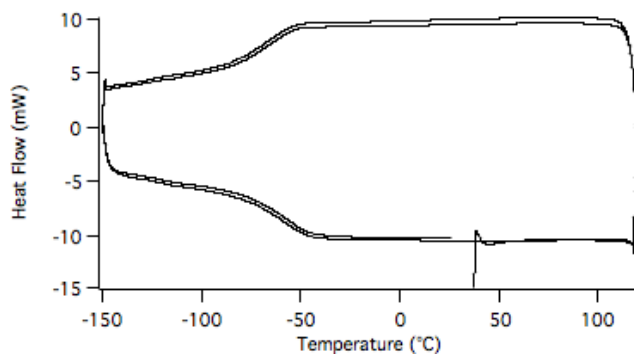


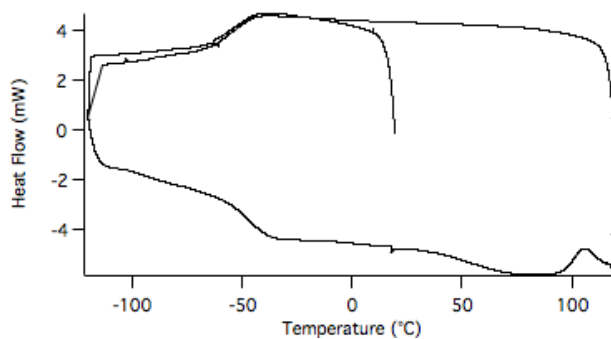
Figure S5.6 TGA of membrane soaked in blank DOL/DME electrolyte (a) Nafion (b) PEGDMA:VS = 10 : 0 (c) PEGDMA:VS = 10 : 4



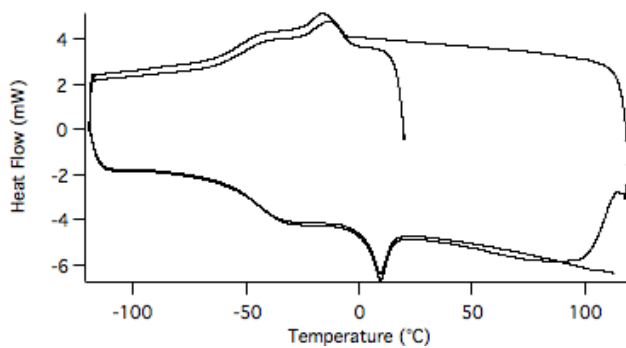
PEGMDA:VS=10:0



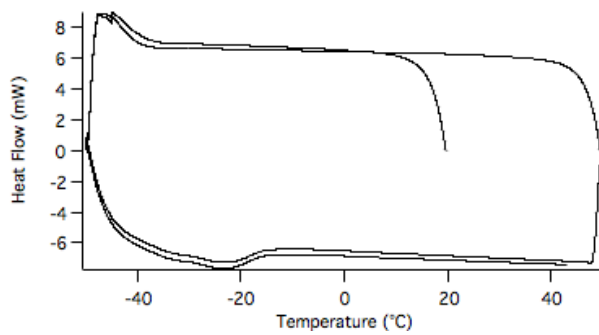
PEGMDA:VS=10:2



PEGMDA:VS=10:4



PEGMDA:VS=10:6



PEGMDA:VS=10:6 with solvent

Figure S5.7 DSC of the membranes. A heating and cooling rate of 10°C/min is used.

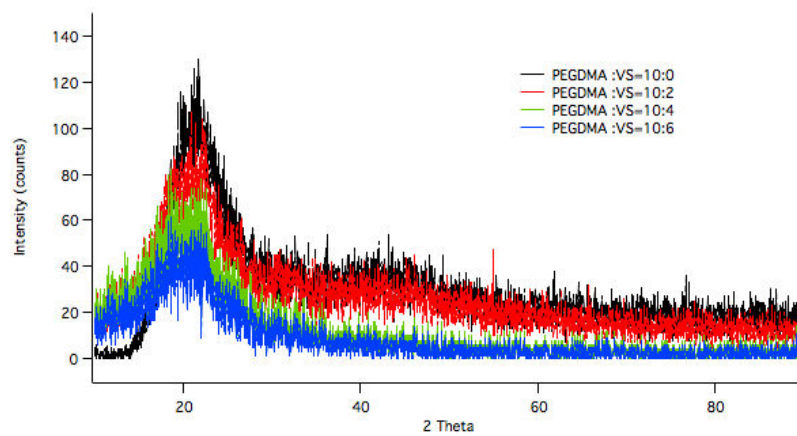


Figure S5.8 XRD of the membranes at room temperature.

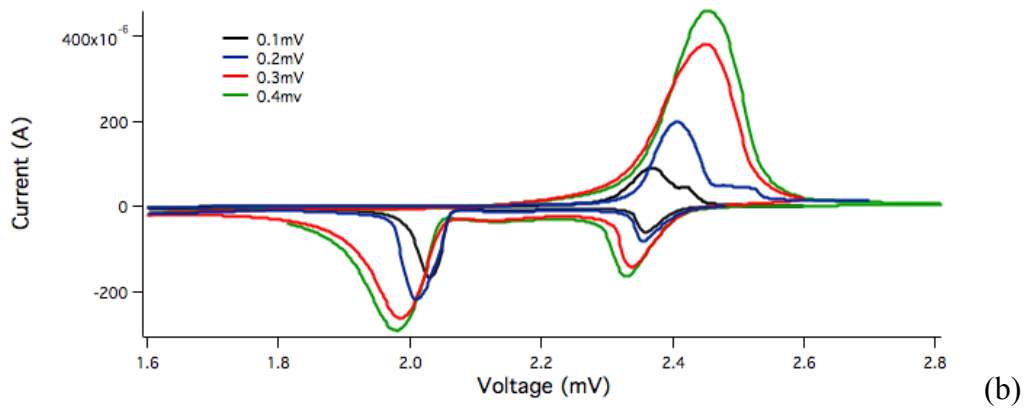
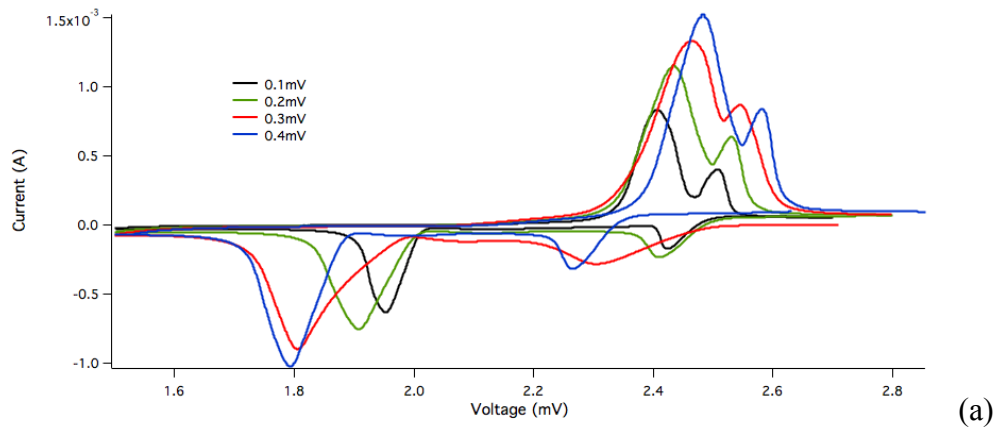


Figure S5.9 CV of the Li-S cells at different scan rate with (a) Celgard; (b) PV6.

Table S5.1 Diffusion coefficient of lithium ion of the redox peaks in Li-S cells.

D_{Li} (cm ² /S)	Celgard	PV6
1 st reduction peak (>2.2V)	1.71874E-08	1.70542E-08
2 nd reduction peak (<2.0V)	2.28979E-08	1.22987E-08
Oxidization peak	3.36873E-07	2.17528E-07

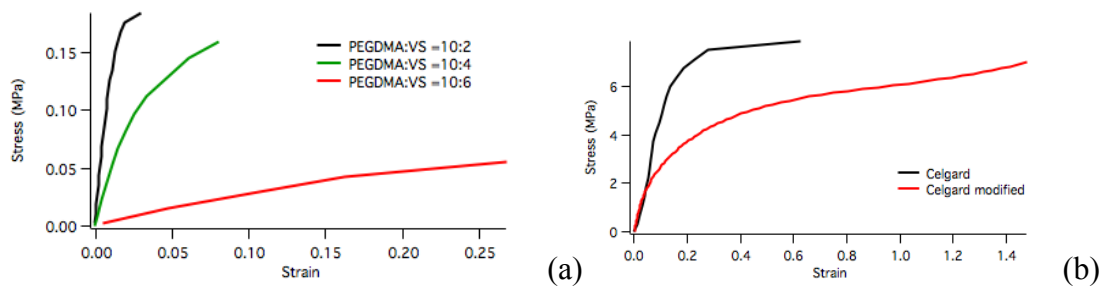


Figure S5.10 Mechanical properties of the membrane. (a) membranes with different sulfonate content; (b) sandwich-typed membrane.

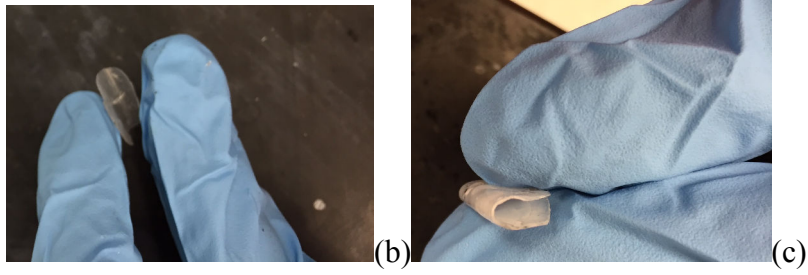


Figure S5.11 Images of the PV6-Celgard-PV6 sandwich membrane.

CHAPTER 6

Stable artificial solid electrolyte interfaces for lithium batteries

6.1 Abstract

A rechargeable lithium metal battery (LMB), which uses metallic lithium at the anode, is among the most promising technologies for next generation electrochemical energy storage devices due to its high energy density, particularly when Li is paired with energetic conversion cathodes such as sulfur, oxygen/air, and oxygen-carbon dioxide mixtures. Practical LMBs in any of these designs remain elusive due to multiple stubborn problems, including parasitic reactions of Li metal with liquid electrolytes, unstable/dendritic electrodeposition at the anode during cell recharge, and chemical reaction of dissolved cathode conversion products with the Li anode. The solid electrolyte interface (SEI) formed between lithium metal and liquid electrolytes plays a critical role in all of these processes. We report on the chemistry and interfacial properties of artificial SEI films created by in-situ reaction of a strong Lewis Acid AlI_3 , Li metal, and aprotic liquid electrolytes. We find that these SEI films impart exceptional interfacial stability to a Li metal anode. We further show that the improvements come from at least three processes: (i) in-situ formation of an Li-Al alloy; (ii) formation of a LiI salt layer at the interface; and (iii) creation of a stable oligomer thin film on the Li anode.

6.2 Introduction

Rechargeable batteries able to reliably store large amounts of electrochemical energy are needed to meet increasing demands for long-lasting, portable electrical energy storage technology for electronic devices, electric vehicles, and autonomous robotics.^{1,2} Lithium-ion batteries (LIBs) are

currently the technology of choice for meeting these needs, however, with current LIBs reaching the theoretical capacity limits set by the chemistry of their cathode and anode materials, a new generation of rechargeable batteries is urgently needed. The lithium metal anode has been described as the “Holy Grail” of energy storage systems due to its extremely high theoretical specific capacity (3860 mAh/g), low gravimetric density (0.59g/cm^3), lowest negative redox potential vs. standard hydrogen electrode (-3.040V),^{1,3} and the large variety of high-capacity unlithiated materials it enables as legitimate choices for the battery cathode. Thus, by replacing the carbonaceous host material used as the anode in an LIB with metallic lithium, rechargeable lithium metal batteries (LMBs) with impressive theoretical specific energies become possible.^{4,5} Among these cathode materials, sulfur with a theoretical capacity of 1675 mAh/g has attracted sustained scientific interest for a variety of reasons, including its low cost, low toxicity, high natural abundance, and the fact that it undergoes spontaneous electrochemical reactions with lithium that do not require catalysts.^{2,6,7}

Unfortunately, uncontrollable dendritic lithium growth and limited Coulombic efficiency during Li deposition/stripping inherent in all batteries that utilize metallic lithium as anode have prevented broader practical applications. The formation and subsequent growth of lithium dendrites induced by inhomogeneous distribution of current density on the lithium metal anode may pierce the polymer separator, resulting in short circuit and subsequent thermal runaway of the cell.^{3,5,8} In addition, lithium metal is very reactive and over many cycles of charge and discharge will react with liquid electrolyte in contact with the metal to form fresh solid electrolyte interfaces (SEI), which ultimately consume the electrolyte causing low cycling efficiency as the internal resistance of the cell diverges.^{9,10} The already complicated chemistry at the interface of a lithium metal anode and liquid electrolyte is made even more complex when

lithium metal is paired with sulfur in a lithium-sulfur (Li-S) battery, which makes these batteries an important platform for fundamental studies of how each of the degradation processes interact to cause premature failure of LMBs.

In Li-S batteries, the unique chemistry and transport behavior of soluble lithium polysulfides (LiPS) generated during discharge, lead to multiple chemical pathways in the SEI that consume Li, deplete the active anode material, and may also cause the interfacial resistance at the Li metal anode to become more inhomogeneous, which promotes rough dendritic Li deposition during cell recharge.^{2,11} The products created by reduction of sulfur by lithium have been studied extensively and are now thought to include Li_2S_n species with n value ranging from 1 to 8.^{2,6,12} Whereas the low order Li_2S_n ($n \leq 2$) are insoluble in most aprotic liquid electrolyte solvents, high order lithium polysulfides Li_2S_n ($n > 2$) dissolve, causing low utilization of active materials and parasitic reaction with the Li anode.^{12,13} Soluble lithium polysulfides (LiPS) capable of diffusing throughout the separator also react with the Li metal anode to form insoluble and insulating sulfides on the surface of the anode, increasing the interfacial resistance at the anode and lowering both the efficiency and rate capability.¹⁴ To solve the LiPS dissolution problem, several studies have considered novel cathode designs, including use of nanostructured carbons and metal oxides as sorbents in the cathode to provide physical trapping for LiPS,^{13,15,16} specially designed additives to sequester LiPS via chemical interactions,^{11,17} and polymer coatings of the cathode to provide additional transport and kinetic barriers for LiPS dissolution.^{18,19} In a departure from this approach, a recent study by Ma et al.²⁰ showed that carbon nanotubes grafted with covalently attached polyethyleneimine (PEI) chains take advantage of kinetic and thermodynamic processes to provide exceptionally high resistance to dissolution of LiPS in liquid electrolytes. Even in that case, however, the authors reported that

over sufficiently long times, some amount of LiPS dissolves in the electrolyte. It means that the problem of LiPS dissolution in a Li-S cell cannot be solved through clever engineering of the cathode alone because the preferred electrolytes (eg. Dioxalane (DOL), 1,2-dimethoxyethane (DME), Tetraglyme) have sufficiently high solubility for LiPS that there will always exist a chemical potential gradient between the cathode and electrolyte solvent at equilibrium, which favors dissolution and loss of LiPS to the electrolyte.

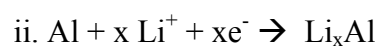
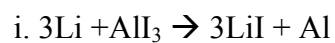
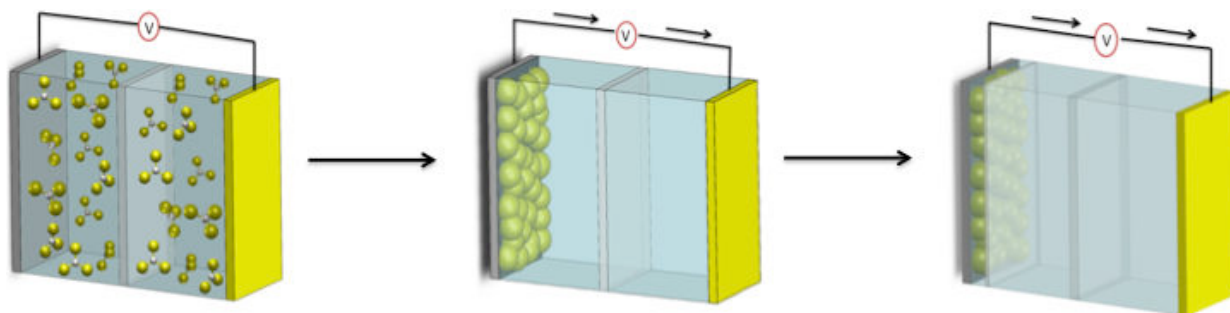
Normally the three open problems with the Li-S cell — unstable dendritic deposition of Li at the anode during recharge; dissolution, shuttling of LiPS formed at the cathode; and uncontrolled reaction of dissolved LiPS with the anode to form resistive insoluble passivating sulfide layers are addressed independently with novel materials designs suitable for either electrode. A strategy that simultaneously sequesters sulfur in a Li-S battery cathode, protects the anode from reaction with dissolved LiPS, and at the same time eliminates dendritic deposition of Li at the nucleation step is a long sought after strategy for enabling Li-S cells able to live up to the potential of this battery technology. Herein, we report that introduction of the Lewis acid AlI_3 in DOL-DME electrolytes engenders multiple synergistic processes that enable Li-S cells with unprecedented stability and cycling efficiency.

Our interest in AlI_3 originates from two fundamental attributes of the material: i) The I^- ion has long been understood to play a special role in adsorption phenomenon in electrochemistry.^{21,22} I^- belongs to the Class IB adsorbents, which are known to have remarkable surface affinity and to exhibit stronger interactions with metallic substrates than those in class IA ions or adsorbents that bond by means of simple electrostatic interactions. It is believed that these features of Class IB adsorbents originate from donation of electrons from the adsorbing anions to available

orbitals on the electrode surface. As a result, Class IB anions can be adsorbed on either positively charged or negatively charged surfaces with equal facility. Thus, dissociation of AlI_3 salt additives in an electrolyte in an electrochemical cell is expected to result in an I^- rich SEI layer at both electrodes. At a Li anode, it is hypothesized that the I^- bonds with Li to form a conformal LiI salt layer localized at the electrode surface. Such a LiI coating has been argued on the basis of recent Joint Density Functional (JDFT) calculations to be as effective as LiF surface coatings in lowering the activation barrier for Li^+ transport across the electrolyte-electrode interface,^{23,24} allowing it to conduct Li ions while at the same time preventing direct contact and reaction between a lithium metal anode and electrolyte solvents. ii). AlI_3 can enhance Li cycling performance by in-situ formation of a Li-Al metal alloy layer at the anode.²⁵ Such alloys have been reported to provide efficient barriers to Li dendrite formation, resulting in the enhancement of Li cyclability.²⁶⁻²⁸ In the search for understanding, we also discover that Al^{3+} , as a strong Lewis acid, is an efficient initiator for polymerization of DOL.²⁹ Because of the surface affinity of I^- , the polymerization reaction initiated by Al^{3+} occurs at interfaces to produce a thin ion-conducting polymer film on the surface of lithium metal, which we believe stabilizes the lithium metal against side reactions with the electrolyte.

Figure 6.1 summarizes our understanding of the specific chemical processes by which AlI_3 performs the proposed set of functions in a Li-S cell. As a proof-of concept, we first fabricated the artificial protective film on Li metal by using an electrochemical approach. The protected lithium metal was used in an additive-free (i.e. no LiNO_3) electrolyte to evaluate the effectiveness of the surface modification in overcoming the range of challenges with Li-S cells discussed in the introduction. The protective SEI layer on Li metal anode used in the demonstration was formed by cycling a symmetric lithium metal cell in a DOL/DME-1M

LiTFSI electrolyte with AlI_3 as an additive. The chemical composition of the artificial SEI and its effectiveness in resolving the aforementioned difficulties are presented throughout the remainder of the paper. It is understood that in a practical Li-S battery the LiNO_3 additive can be re-introduced in whatever quantities desired to achieve a specific performance; here we eliminate consideration of this additive because the goals of the study are more fundamental.



iii.

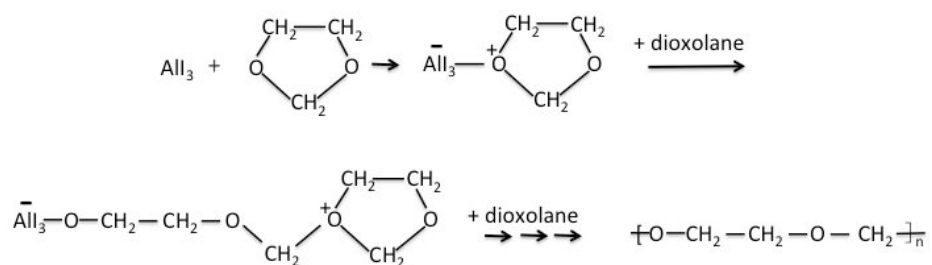


Figure 6.1 Proposed formation mechanism for a multi-functional artificial solid electrolyte interfaces (SEI) at a Li anode produced by AlCl_3 .

Our results show that while a wide range of conditions can be used for the pretreatment reaction, the surface reactions are self-limiting and the beneficial attributes of the artificial SEI formed can only to a modest extent be manipulated via the reaction conditions. In a preferred approach, Li metal is first discharged, and then charged at constant current to a 2% depth of discharge in the electrolyte containing AlI_3 . This pretreatment allows the electrochemical cleaning of lithium metal and also the complete formation of a stable SEI layer. At moderate current density (e.g. 2 mA/cm^2) the process facilitates removal of the oxide film on the lithium surface, initializing the chemical reaction between pure Li and Al^{3+} .³⁰ Progress of the pretreatment reactions can be followed electrochemically by measuring the voltage profile (see Supplemental Information, **Figure S6.1**) and by imaging the lithium metal surface before and after treatment are shown in **Figure S6.2**.

6.3 Results and discussion

To evaluate the effectiveness of AlI_3 as a Li surface protection agent, lithium metal foil pretreated using the approach described above was used as electrodes in both symmetric (Li/Li) and full (Li-S) cells to investigate the effectiveness of the SEI layer in stabilizing the lithium metal against parasitic reactions with dissolved LiPS and dendrite formation during cell recharge. Lithium metal is known to react spontaneously with LiPS. Once contacted, by an electrolyte containing dissolved LiPS species, lithium metal will be oxidized by LiPS to form solid Li_2S_8 , which will deposit onto the lithium metal surface as an undesirable insulating layer. At the same time, the reduction of the dissolved LiPS leads to a distinct color change in the electrolyte as the order n of the LiPS is reduced. To evaluate the effectiveness of our surface coating strategy, lithium foil with and without surface treatment was immersed in a solution of 0.05M Li_2S_8

dissolved in tetraglyme, a good solvent for Li_2S_8 , and changes in the appearance of the electrolyte and lithium metal recorded. The results reported in the upper row of **Figure 6.2a** are for the pristine (untreated) Li foil, whereas those in the second row are typical results obtained using the AlI_3 treatment approach described above. For the pristine lithium, there is an obvious change of color of the electrolyte, indicating LiPS is reacting with lithium metal. The dark reddish color, which corresponds to high order LiPS, is observed to become markedly lighter over time. In contrast, the color of the electrolyte on the second row stays relatively dark, indicating LiPS is very stable in this case. After 12h, the electrolyte was taken out and characterized with UV-vis spectroscopy, and the results are shown in **Figure 6.2b**. The black curve corresponds to the initial Li_2S_8 solution in tetraglyme, which shows spectra consistent with literature results for basically long chain LiPS (Li_2S_8).^{31,32} In the case of pristine lithium, the UV-vis signatures for short chain LiPS are clearly evident indicating the reduction of LiPS by reaction with lithium metal. And, consistent with the pictures shown in **Figure 6.2a**, the UV-vis spectrum of the electrolyte in contact with the pretreated Li foil is essentially identical to that of the freshly prepared electrolyte. The lithium metal immersed in the LiPS electrolyte for 12h was removed and characterized by X-ray diffraction (XRD); results are shown in **Figure 6.2c**. It is obvious that the pristine lithium reacts with LiPS and forms Li_2S on the metal surface. However, for the pretreated lithium metal, XRD peaks for pure Li metal remain even after 12-hour exposure to LiPS and no obvious Li_2S crystal structure is detected. Both the visualization of the color change of electrolyte, and the post-mortem analysis by UV-vis spectroscopy and XRD therefore confirm the stability of lithium metal against LiPS is improved substantially when it is pretreated with AlI_3 .

The stability of the treated Li metal in the presence of LiPS was also investigated by

Electrochemical Impedance Spectroscopy (EIS) experiments. Symmetric Li/Li cells either using pristine Li (control) or AlI_3 treated Li were employed in these experiments and the electrolyte is deliberately reinforced with 0.1M Li_2S_8 (**Figure 6.2d**), and the impedance is characterized as a function of time, which provides an indication of the lithium corrosion level by reacting with LiPS in the electrolyte. Both the real (resistance) and imaginary (capacitance) parts of the impedance are seen to increase more for the control cells. In particular the real part of the impedance of the control cells is seen to increase rapidly, reaching a value of around 250% of the initial value after 72 hours. In contrast, cells containing protected lithium are noticeably less reactive when in contact with LiPS rich electrolyte—only 45% increase is observed for the impedance over 72h. Following these measurements, the Li electrodes were harvested and the surface morphology of lithium metal observed using scanning electron microscopy (SEM). For the unprotected lithium metal, the lithium surface is seen to be very rough, indicating the severe erosion of lithium metal by LiPS; however the pretreated lithium has much less roughness (**Figure S6.3**).

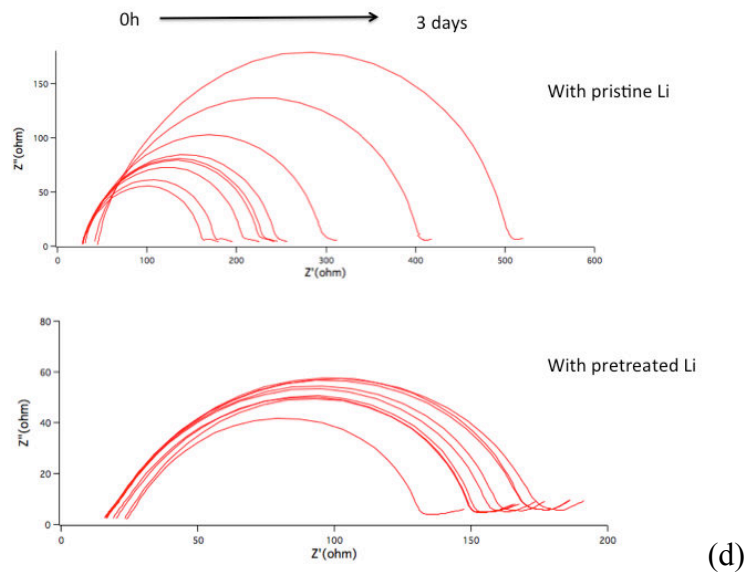
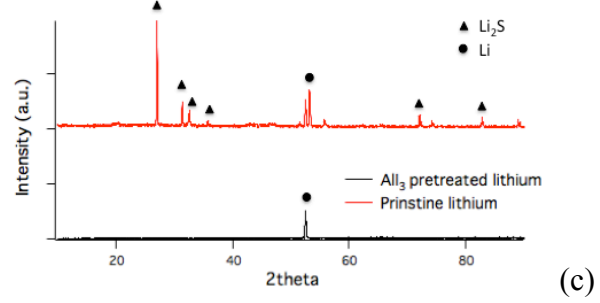
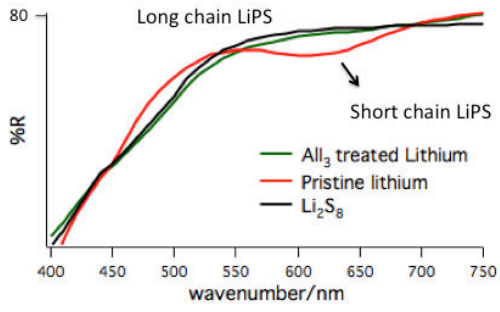
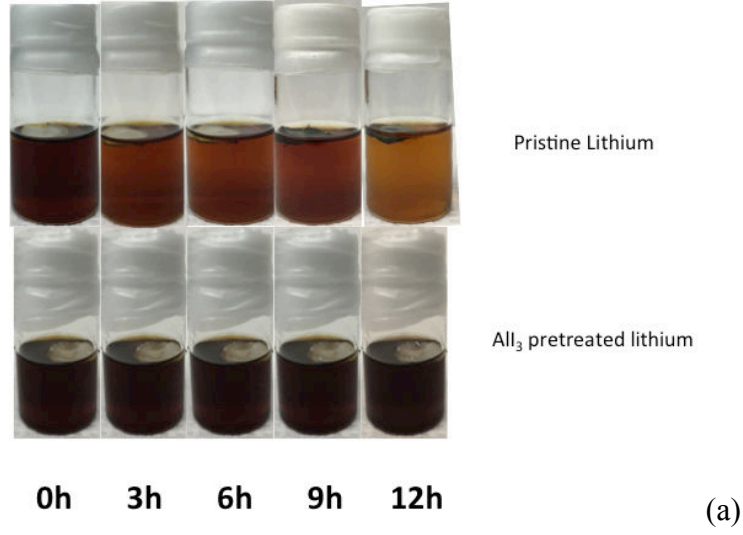


Figure 6.2 Chemical stability of AlI_3 -DOL-treated lithium metal in a LiPS-rich electrolyte. **a**, Optical images recorded at a 3-hour interval of a LiPS-rich liquid electrolyte exposed to Li metal without (upper row) and with (lower row) pretreatment by AlI_3 -DOL. **b**, Uv-vis spectra of a LiPS-rich electrolyte after exposure to lithium metal for 12 hours. **c**, XRD of the pristine lithium metal (red) and AlI_3 -DOL-treated lithium metal foil (black) after immersion in a LiPS-rich electrolyte for 12 hours. **d**, Nyquist plot for a lithium symmetric cell containing a LiPS rich electrolyte recorded in 8 hour increments.

A remarkable and synergetic benefit of the AlI_3 surface treatment revealed by the proposed reaction mechanism in **Figure 6.1** is that both the LiI layer and Li-Al alloys formed at the interface should stabilize Li metal against dendrite formation during cell cycling. To investigate these effects, symmetric (Li/Li) cells containing pristine and AlI_3 -treated Li foil were assembled. A standard polypropylene membrane (CelgardTM) was used as the separator and 1M LiTFSI in DOL/DME (v:v=1:1) was applied as electrolyte. To evaluate the stability of the cells to failure by dendrite-induced short circuiting, galvanostatic polarization measurements were performed in which lithium is continuously stripped from one electrode and plated on the other at a fixed current density; cell failure in this experiment occurs when the measured voltage is observed to drop discontinuously (see supporting **Figure S6.4**) as the internal short lowers the cell resistance.³³ **Figure 6.3a** reports the cell lifetimes at various current densities. It is seen that the, lifetime or short-circuit time t_c is greatly improved when lithium metal is protected with SEI layer involving AlI_3 . The improvement is more obvious when higher current is applied and the resultant t_{sc} values at $3\text{mA}/\text{cm}^2$ are the highest reported in the literature for this experiment.^{3,33} It should also be noted that the electrolyte used in these experiments contains no additives, which means that the SEI layer is quite stable by itself over lithiation over a long period.

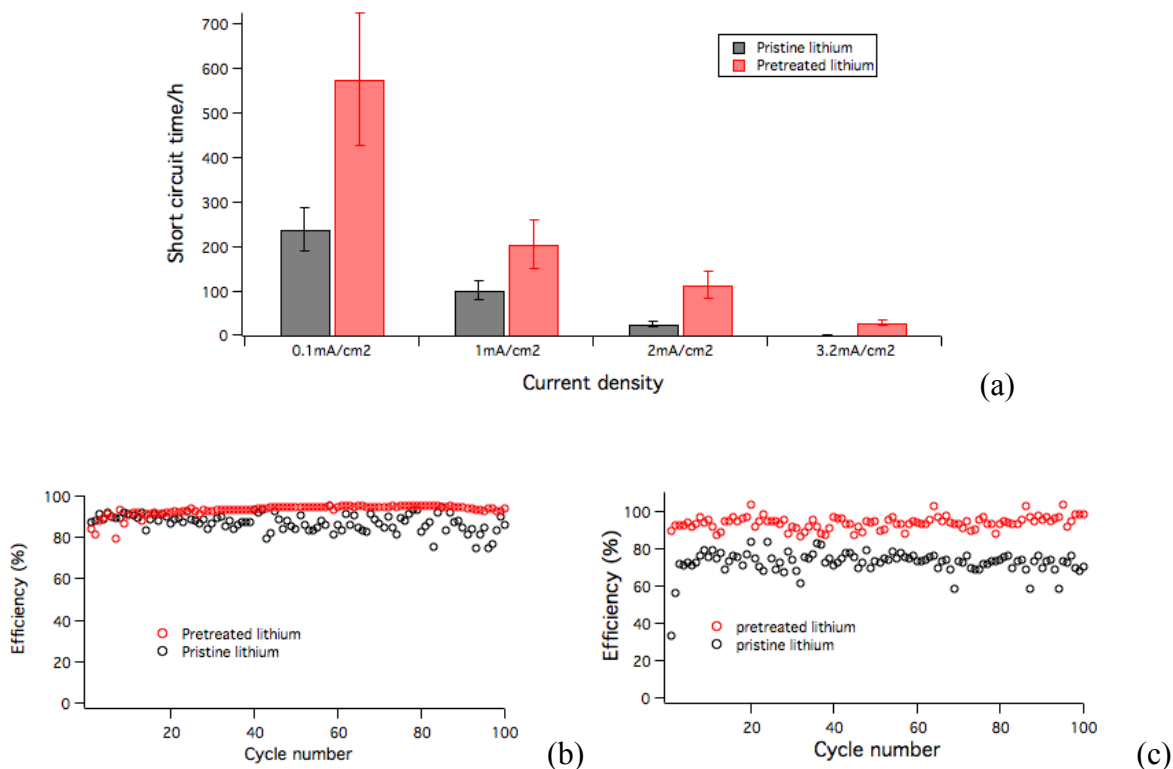


Figure 6.3 Lithium dendrite resistance and Coulombic efficiency of AlI_3 -DOL-treated lithium metal. a, Short circuit time for symmetric Li/Li cells deduced from galvanostatic polarization measurements at different current densities. The dark grey column represents the control case in which pristine lithium is used; the light grey column shows the short circuit time for cells based on AlI_3 -DOL-treated lithium metal. b and c, Lithium deposition efficiency in Li/electrolyte/stainless steel cells comprised of pristine lithium and AlI_3 -DOL-treated lithium metal electrodes, respectively. In these experiments, the cell is discharged for 30 min at a constant current density then recharged to 0.5V at the same current density. b, Current density = 0.2 mA/cm². c, Current density = 2 mA/cm².

The Coulombic efficiency (CE) provides a simple measure of the effectiveness of the Li surface protection offered by the AlI_3 treatment. CE was examined using a Li/electrolyte/stainless steel cell design, which allows the lithium loss on cycling to be accurately determined as the amount of lithium stripped divided by the amount of lithium plated on the stainless steel foil. A fixed amount of lithium is stripping from the lithium metal by a constant discharge current and deposited on to stainless steel, followed by a charge process where all the lithium is coming back to lithium electrode from stainless steel.³⁴ **Figure 6.3b and 6.3c** shows the Coulombic efficiency versus cycle number for cells with 1M LiTFSI in DOL/DME (v:v=1:1) at current densities of 0.2 mA/cm^2 and 2 mA/cm^2 (**Figure 6.3b and 6.3c** respectively). The black curve is the control case, in which pristine lithium is used, and the red curve represents the pretreated lithium. In **Figure 6.3b**, when pretreated lithium metal is used, the CE is stable at $\sim 95\%$, while there is fluctuation in the cell with pristine lithium. There is still loss of efficiency with the protection of AlI_3 and that might be due to the exposed lithium on stainless steel reacting with the electrolyte. The improvement is still observed when the current density is increased to 2 mA/cm^2 (**Figure 6.3c**), where the efficiency is increased from $\sim 70\%$ to $\sim 92\%$ when lithium metal is pretreated with AlI_3 . **Figure S6.5** reports the CE for electrolytes in which LiPS is directly added to promote parasitic reactions with the freshly deposited Li metal. The addition of LiPS to the electrolyte is observed to dramatically decrease the stability of the control cell, resulting in the large fluctuation of the efficiency when pristine lithium is used. However, consistent with what we found in **Figure 6.2**, the pretreated lithium metal shows improved stability against LiPS and the cycling is much more stable with an improved efficiency to $\sim 91\%$ over 100 cycles.

The results reported in **Figures 6.2 and 6.3** therefore demonstrate the effectiveness of AlI_3 as an additive in the formation of stable SEI layer on Li metal. The results also show that treatment of

Li metal with AlI_3 greatly improves its stability against LiPS erosion, enhances its resistance to failure by lithium dendrite formation and improves the Coulombic efficiency of the cell. Before illustrating the benefits of these synergistic effects in a Li-S cell, we consider how AlI_3 performs these functions in detail.

Figure S6.6 shows the impedance for symmetric cells before and after treatment with AlI_3 . The solid lines correspond to the cells before cycling. The cells containing AlI_3 in the electrolyte already show lower impedance compared with the control case. We infer that there may already be a SEI layer formed before electrochemical treatment so that the conductive LiI layer leads to lower impedance. After a single cycle, the impedance of AlI_3 is observed to shrink substantially. This may be due to formation of a more complete SEI layer after the cleaning of lithium surface and the strong adsorption of I^- anion on the electrodes. In contrast, for the control case, the impedance doesn't change too much before and after the treatment. It might be because after cleaning the lithium surface, it immediately reacts with the electrolyte solvents and again forms lithium oxidation products, such as lithium hydroxide or other lithium oxides, which has similar interfacial chemistry and transport properties with the pristine surface and results in similar impedance.

The pretreated lithium metal was harvested, washed thoroughly with DOL/DME, and its surface chemistry characterized by means of XPS. **Figure 6.4a** shows a strong I 3d signal, which has well separated spin-orbit components with an energy separation of 11.5 eV. The deconvolution of I 3d 5/2 shows both Li-I and Al-I peaks, which is consistent with our hypothesis of strong I^- ion adsorption. Also, Li 1s peak (**Figure 6.4b**) can be deconvoluted into Li-I, Li-Al alloy and Li-OH peaks.^{35,36} We suspect that the hydroxides may be formed during the sample transfer or the

reaction between lithium and the solvents. Again this is consistent with our hypothesis that there is formation of Li-I and Li-Al alloy during the discharge and charge process, which can help to stabilize lithium metal. Al signals are also detected in the XPS spectra. Deconvolution of Al 2s peak (**Figure 6.4c**) shows both the metal Al (120eV)²⁹ and Al ion (~118eV) peaks,³⁷ confirming the existence of Al metal and Al ion on the surface, providing clue for Li/Al alloy formation and Al³⁺ adsorption on the electrode surface.

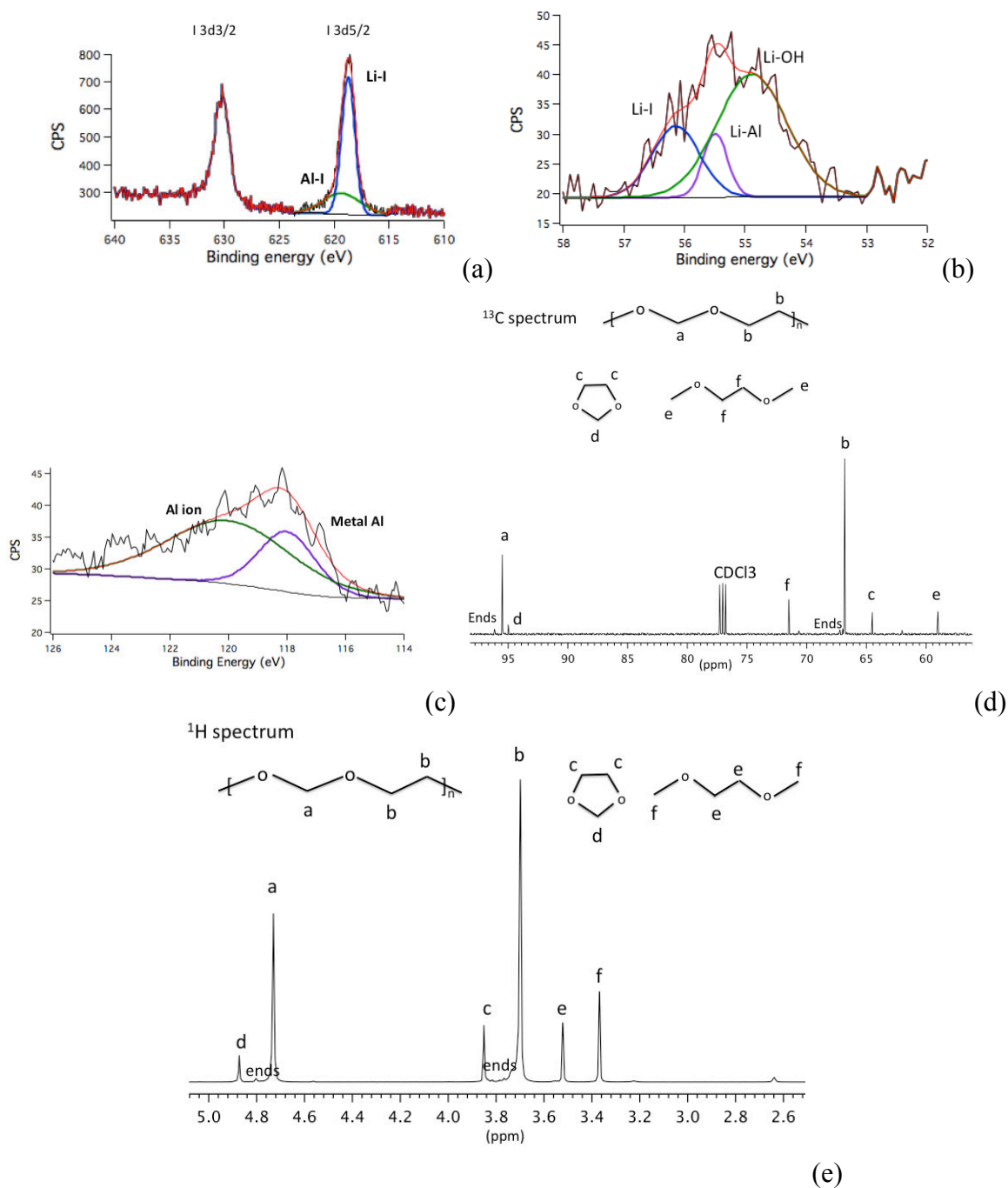


Figure 6.4 Characterization of the AlI_3 -DOL-treated lithium metal by XPS and NMR. a, b and c, High resolution XPS spectra for AlI_3 -DOL-treated lithium metal. a, I 3d spectra; b, Li 1s spectra; c, Al 2s spectra. d and e, NMR of the polymeric gel. d, ^{13}C NMR spectrum. e, ^1H NMR spectrum.

Following galvanostatic polarization, post-mortem characterization of the lithium metal electrode was carried out using XPS and SEM analysis. It is significant that the signatures of Al and I are still apparent from the XPS spectra (**Figure S6.7b and S6.7c**) of the pretreated material after polarization. It indicates that the SEI layer formed by the reaction of Li and AlI_3 is stable even after cells short are circuited in a polarization experiment. What's perhaps even more interesting is that even after the cell shorts, the film-like appearance of the Li metal coating remains largely intact (**Figure S6.8a**). The film structure seems to be punctured through by the lithium dendrite growth. The film was also observed to form spontaneously as an upper (lower-density phase) in an AlI_3 containing electrolyte (**Figure S6.8b**) after the electrolyte was rested for a period of about 2 weeks in an Ar-filled glove box. The gel-like membrane was separated from the liquid electrolyte and washed with DOL/DME to get rid of any interred salts and characterized by Gel Permeation Chromatography (GPC). Analysis of the results reported in **Figure S6.9a** using polystyrene standards shows that the material is a polymer with number averaged molecular weight, $M_n \approx 2200$ g/mol, weight-averaged molecular weight $M_w \approx 3380$ g/mol, and polydispersity index $\text{PDI} = M_w / M_n = 1.5$.

In order to investigate the chemistry and structure of the polymer, mass spectra and NMR measurements were performed. **Figure S6.9b** shows that a series of species/fragments with a mass difference of 74 is observed. This mass increment is exactly the molecular weight of DOL, meaning that the film formed in the AlI_3 -containing electrolytes is polyDOL. NMR analysis (**Figure 6.4d and 6.4e**) confirm that the gel is composed of polymerized DOL with a structure of $n\text{-}[-\text{O}-\text{CH}_2-\text{O}-\text{CH}_2-\text{CH}_2-]_n$. Both the ^{13}C and ^1H spectra match pretty well with the proposed structure. They also show peaks for DOL and DME small molecules due to the solvent residue in the gel, which disappear when the gel is tested with diffusion ordered $^1\text{HNMR}$ (**Figure S6.10**),

where the polymer signal remain as slow diffusers. Thus the information provided by GPC, mass spectra and NMR spectra reveal that the gel is the product of DOL polymerization. Our finding while important is not surprising since the ring opening of DOL is already known to be initiated by Lewis acid acting as initiator and was one of the reasons we chose to work with AlI_3 as a strong Lewis acid able to attack the nucleophile center on the O atom and initiate the polymerization of DOL.³⁸⁻⁴⁰ **Figure 6.5** reports the electrochemical characteristics of Li-S cells based on the AlI_3 -treated Li metal anodes at a current rate of 0.5C. The cathode used in these experiments was prepared by the methods reported earlier, where sulfur is infused into amine-functionalized CNT.²⁰ The green plot in **Figure 6.5a** corresponds to the control case, where pristine lithium metal is used, and the black curve represents pretreated lithium metal is used as anode. The capacity is very similar between the two cases while the efficiency is increased from 83%~92 %. What is more interesting is that when additional AlI_3 is introduced to the electrolyte, both the capacity and efficiency rise, with the CE exceeding 97% by the 100th cycle. We suspect that this benefit of utilizing additional AlI_3 in the Li-S electrolyte stems from the ability of AlI_3 to repair any defects in the surface coating formed during the pretreatment or by reaction with LiPS in the cycled electrolyte. The need for such repair is evident in **Figure 6.2d**, where the impedance of the symmetric cell using AlI_3 -treated lithium also increases to some extent, suggesting the formation of a certain amount of Li_2S on lithium surface. The voltage profile in **Figure 6.5b** shows that during cycling the overpotential in both the discharge and charge process is greatly suppressed when AlI_3 is incorporated. **Figure S6.11** shows the cyclic voltammetry of the Li-S battery applying the pretreated lithium as the anode. The peaks show typical characteristics of sulfur reduction and oxidization, and the stable position of the peaks indicates stable electrochemical reaction of sulfur.

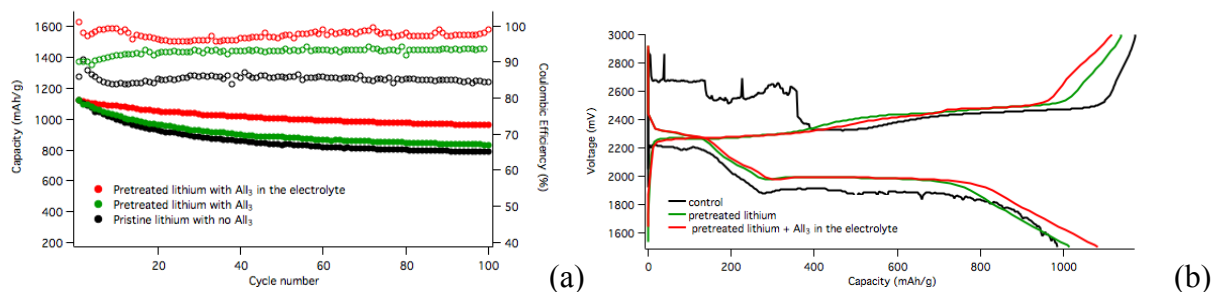


Figure 6.5 Electrochemical measurements employing Li-S cells containing AlI_3 -DOL-treated lithium metal as anode and at a current rate of 0.5C. These cells do not contain LiNO_3 electrolyte additives typically used in Li-S battery studies. a, Comparison of cycling performance of Li-S cells based on AlI_3 -DOL-treated and untreated Li metal anodes. The black filled symbols denote the specific capacity of cells based on pristine lithium metal anodes with additive free electrolyte; the green filled symbols are specific capacities of cells based on AlI_3 -DOL-treated Li anodes with additive-free electrolyte; the red filled symbols denote specific capacities of cells based on AlI_3 -DOL-treated Li anodes and DOL/DME-based electrolytes containing AlI_3 as additive. The open symbols are the respective Coulombic efficiency. b, The corresponding voltage profiles for Li-S cells in each of the configurations reported in Figure 6.5a.

6.4 Materials and Method

6.4.1 Pre-treatment of lithium metal with AlI_3

A symmetric cell (Li/electrolyte/Li) was assembled and used to create tethered polymer coatings on Li. 40 μL 1M LiTFSI and 600ppm AlI_3 dissolved in DOL/DME (v:v=1:1) was used as electrolyte. The electrolyte solvents were dried over 3Å molecular sieves; the salts were dried at 100 °C under vacuum. All electrolyte components were stored in an argon-filled glovebox prior to use and the electrolyte was prepared by mixing these components with a Teflon-coated stir bar in the glovebox. The moisture content of electrolytes produced in this manner was quantified by Karl-Fisher titration (Mettler ToledoTM C20 KF titrator) and found to be <20 ppm. The symmetric cell was discharged at a current density of 2 mA/cm², at a depth of 2% DOD, followed by a charge process at the same current density. The cell was opened in an Ar-filled glove box and the anode retrieved for surface characterization and electrochemical analysis. Whereas coated anode samples for electrochemical analysis were directly transferred to sealed electrochemical cells in the same Ar-filled glovebox, those used for our surface characterization experiments had to be removed from the glovebox.

6.4.2 Characterization

The LiPS species in the electrolyte was analyzed using a Shimadzu UV-Vis Spectrometer. The crystalline structure was characterized using Scintag Theta-Theta X-ray Diffractometer (XRD). Morphologies of the electrodes were studied using LEO 1550 FESEM (Keck SEM) and FEI Tecnai G2 T12 Spirit TEM (120 kV). Impedance spectra were recorded as a function of frequency using a Novocontrol N40 broadband dielectric spectrometer. X-ray photoelectron spectroscopy (XPS) was used for elemental analysis and to obtain chemical information of films

formed on the Li electrode. Gel permeation chromatography (GPC) was utilized to characterize the molecular weight of the polymer coating on the lithium anode. The polymer was dissolved in tetrahydrofuran (THF) to form a solution with concentration 1mg/ml and a Waters Ambient-Temperature GPC operated at 40°C with an elution rate of 1.0mL/min was employed to recover the elutogram for the solution. Polystyrene standards with molecular weight in the range 10^3 D to 10^6 D (PSS USA; Amherst, MA) were used as reference to estimate the molecular weight of the polymer from the elutogram. The polymer composition was investigated using Direct Analysis in Real Time (DART) ambient ionization mass spectrometer, and its structure analyzed using an INOVA 400 NMR facility.

6.4.3 Electrochemical Characterization

The sulfur cathode composite CNT-PEI/S is prepared as described in a previous study²⁰, and the sulfur content in the composite is 60%. 2030 coin-type cells were assembled using Lithium metal (0.76 mm. thick, Alfa Aesar) as the anode electrode, a microporous material, Celgard 2500, membranes as separator, a cathode with 80% as prepared CNT-PEI/S composite, 10% Super-P Li carbon black from TIMCAL, and 10% poly (vinylidene difluoride) (PVDF, Sigma Aldrich) as binder in an excess of N-methyl-2-pyrrolidone in NMP, and electrolyte of 40uL 1M lithium bis(trifluoromethanesulfone) imide (LiTFSI) for each cell. The sulfur loading per electrode is $1.2\text{mg}/\text{cm}^2$. Cell assembly was carried out in an argon-filled glove-box (MBraun Labmaster). The room-temperature cycling characteristics of the cells wear evaluated under galcanostatic conditions using Neware CT-3008 battery testers and electrochemical processes in the celsls were studied by cyclic voltammetry using a CHI600D potentiostat.

6.5 Conclusion

In conclusion, an electrochemical strategy in which AlI_3 is used to initiate polymerization of a DOL/DME-based electrolyte to form a stable artificial SEI coating to protect the lithium metal anode. The procedure leads to the formation of a surface coating on Li that includes LiI, Li-Al and a thin polymer film. The polymer film is shown by means of mass spectrometry, gel permeation chromatography, and NMR to be an oligomer of weight average molecular weight of 3380 g/mol that results from polymerization of DOL initiated by Al^{3+} . When the pretreated lithium metal is used as the electrode in symmetric Li/Li cells or as anode in Li-S cells, the stability of the electrode is shown to be greatly improved by multiple synergistic processes. These processes include the effect of LiI and Li-Al in stabilizing electrodeposition of Li against dendrite formation and protection of the Li anode in the Li-S cell from reaction with soluble LiPS and therefore reducing shuttling and anode surface passivation. The promising electrochemical results and scientific understanding made possible by the study, underscore the promise of AlI_3 and other strong Lewis acids as initiators for the formation of stable, self-limited polymer films that provide artificial SEI coatings to stabilize performance of electrochemical cells based on high-capacity conversion cathodes and metallic anodes.

Acknowledgements

The authors acknowledge support from the National Science Foundation Partnerships for Innovation Program (Grant No. IIP-1237622) and Division of Materials Research Award No. DMR 1609125. Electron microscopy, X-ray diffraction, X-ray photoelectron spectroscopy facilities and optical spectrometers available through the Cornell Center for Materials Research (CCMR) were used for this work (NSF Grant DMR-1120296).

References

1. J. M. Tarascon and M. Armand, *Nature*, 2001, 414, 359-367.
2. L. Ma, K. E. Hendrickson, S. Wei and L. A. Archer, *Nano Today*, 2015, 10, 315-338.
3. Y. Lu, Z. Tu and L. A. Archer, *Nat. Mater.*, 2014, 13, 961-969.
4. Y. Lu, M. Tikekar, R. Mohanty, K. Hendrickson, L. Ma and L. A. Archer, *Adv. Energy Mater.*, 2015, 5, 1402073.
5. M. Armand and J. M. Tarascon, *Nature*, 2008, 451, 652-657.
6. J. Guo, Z. Yang, Y. Yu, H. D. Abruna and L. A. Archer, *J. Am. Chem. Soc.*, 2013, 135, 763-767.
7. G. Cohn, L. Ma and L. A. Archer, *J. Power Sources*, 2015, 283, 416-422.
8. W. Xu, J. Wang, F. Ding, X. Chen, E. Nasybulin, Y. Zhang and J.-G. Zhang, *Energy Environ. Sci.*, 2014, 7, 513-537.
9. J. N. Chazalviel, *Phys. Rev. A*, 1990, 42, 7355-7367.
10. R. Bouchet, S. Maria, R. Meziane, A. Aboulaich, L. Lienafa, J.-P. Bonnet, T. N. T. Phan, D. Bertin, D. Gigmes, D. Devaux, R. Denoyel and M. Armand, *Nat. Mater.*, 2013, 12, 452-457.
11. L. Ma, H. Zhuang, Y. Lu, S. S. Moganty, R. G. Hennig and L. A. Archer, *Adv. Energy Mat.*, 2014, 4, 1400390.
12. A. Manthiram, Y. Fu, S.-H. Chung, C. Zu and Y.-S. Su, *Chem. Rev.*, 2014, 114, 11751-11787.
13. N. Jayaprakash, J. Shen, S. S. Moganty, A. Corona and L. A. Archer, *Angew. Chem. Int. Ed.*, 2011, 50, 5904-5908.
14. K. E. Hendrickson, L. Ma, G. Cohn, Y. Lu and L. A. Archer, *Advanced Science*, 2015, 2, 1500068.
15. H. Wang, Y. Yang, Y. Liang, J. T. Robinson, Y. Li, A. Jackson, Y. Cui and H. Dai, *Nano Lett.*, 2011, 11, 2644-2647.
16. X. Ji, K. T. Lee and L. F. Nazar, *Nat. Mater.*, 2009, 8, 500-506.
17. L. Ma, S. Wei, H. L. Zhuang, K. E. Hendrickson, R. G. Hennig and L. A. Archer, *J.*

- Mater. Chem. A, 2015, 3, 19857-19866.
18. G. Zheng, Q. Zhang, J. J. Cha, Y. Yang, W. Li, Z. W. Seh and Y. Cui, *Nano Lett.*, 2013, 13, 1265-1270.
 19. W. Zhou, H. Chen, Y. Yu, D. Wang, Z. Cui, F. J. DiSalvo and H. D. Abruña, *ACS Nano*, 2013, 7, 8801-8808.
 20. L. Ma, H. Zhuang, S. Wei, K. E. Hendrickson, M. S. Kim, G. Cohn, R. G. Hennig and L. A. Archer, *ACS Nano*, 2015.
 21. F. C. Anson, *Acc. Chem. Res.*, 1975, 8, 400-407.
 22. M. Ishikawa, H. Kawasaki, N. Yoshimoto and M. Morita, *J. Power Sources*, 2005, 146, 199-203.
 23. D. Gunceler, K. Schwarz, R. Sundararaman, K. Letchworth-Weaver and T. Arias, *Nonlinear Solvation Models: Dendrite suppression on lithium surfaces*, 2012.
 24. G. Deniz, L.-W. Kendra, S. Ravishankar, A. S. Kathleen and T. A. Arias, *Modelling and Simulation in Materials Science and Engineering*, 2013, 21, 074005.
 25. A. N. Dey, *J. Electrochem. Soc.*, 1971, 118, 1547-1549.
 26. D. Fauteux and R. Koksabang, *J. Appl. Electrochem.*, 1992, 23, 10.
 27. A. S. Baranski and W. R. Fawcett, *J. Electrochem. Soc.*, 1982, 129, 901-907.
 28. P. Zlatilova, I. Balkanov and Y. Geronov, *J. Power Sources*, 1988, 24, 71-79.
 29. Carsten Dohmeier, Dagmar Loos and H. Schnockel, *Angew. Chem.*, 1996, 35, 129-149.
 30. D. Aurbach, I. Weissman, H. Yamin and E. Elster, *J. Electrochem. Soc.*, 1998, 145, 1421-1426.
 31. M. U. Patel, R. Demir-Cakan, M. Morcrette, J. M. Tarascon, M. Gaberscek and R. Dominko, *ChemSusChem*, 2013, 6, 1177-1181.
 32. W. T. Xu, H. J. Peng, J. Q. Huang, C. Z. Zhao, X. B. Cheng and Q. Zhang, *ChemSusChem*, 2015, 8, 2892-2901.
 33. R. Khurana, J. L. Schaefer, L. A. Archer and G. W. Coates, *J. Am. Chem. Soc.*, 2014, 136, 7395-7402.
 34. W. Li, H. Yao, K. Yan, G. Zheng, Z. Liang, Y.-M. Chiang and Y. Cui, *Nat. Comm.*, 2015, 6.

35. Jojiro Nigoro, Hideki Okuda, Manabu Fujiwara, Katsumi Handa, Kazuo Kojima and S. Ikeda.
36. K. Xie, L. Duan, D. Zhang, J. Qiao, G. Dong, L. Wang and Y. Qiu, *J. Phys. D: Appl. Phys.*, 2010, 43, 252001.
37. J. S. Feliu, A. Samaniego, E. Bermudez, A. El-Hadad, I. Llorente and J. Galván, *Materials*, 2014, 7, 2534-2560.
38. D. Aurbach, *J. Power Sources*, 2000, 89, 206-218.
39. Y. Gofer, Y. Einely and D. Aurbach, *Electrochem. Acta*, 1992, 37, 1897-1899.
40. Doron Aurbach, Orit Youngman, Yosef Gofer and A. Meitav, *Electrochem. Acta*, 1990, 35, 625-638.

Appendix

Supporting information

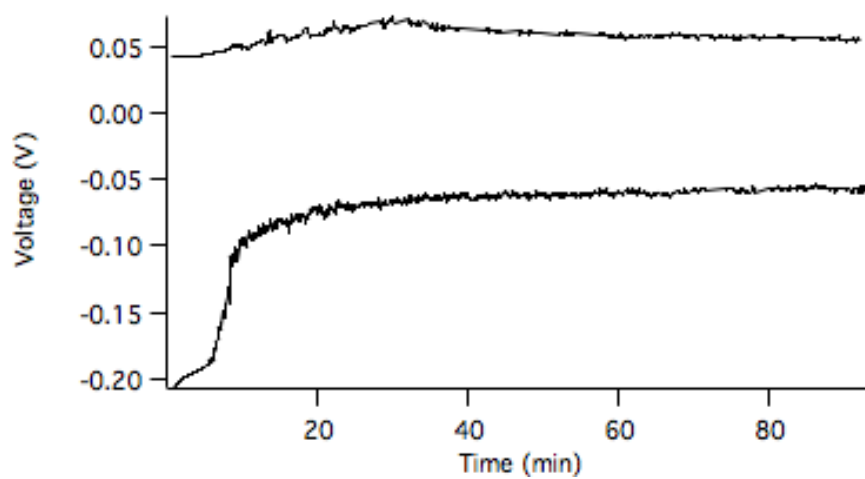


Figure S6.1 Voltage profile of the treatment of the lithium metal. The lithium metal is firstly discharged, then charged, both at a current density of $2\text{mA}/\text{cm}^2$ in AlI_3 containing DOL/DME electrolyte.

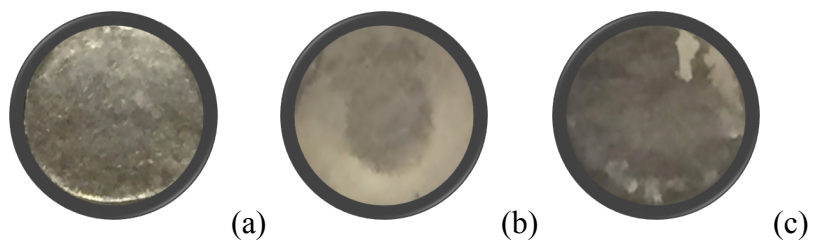


Figure S6.2 Photographic images of lithium metal under different treatment. a, pristine lithium. b, lithium metal pretreated in electrolyte without AlI_3 . c, lithium metal pretreated in electrolyte with AlI_3 .

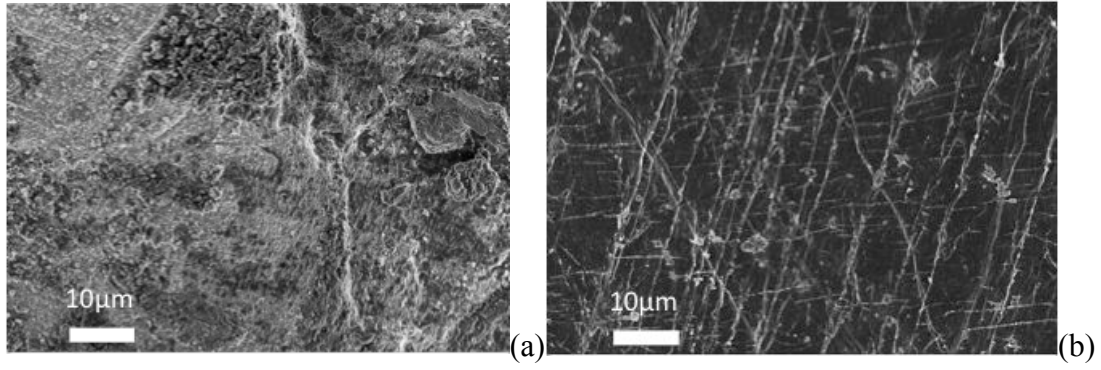


Figure S6.3 SEM images of lithium metal in contact with LiPS rich electrolyte after 3 days in symmetric cell with lithium metal of different treatment. a, pristine lithium metal. b, lithium metal pretreated with AlI_3 .

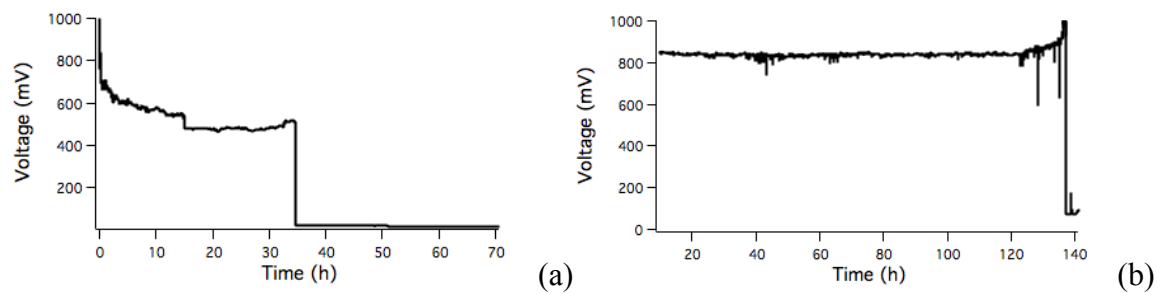


Figure S6.4 Potential profile for symmetric polarization at $2\text{mA}/\text{cm}^2$. a, with pristine lithium as electrodes. b, with pretreated lithium as electrodes.

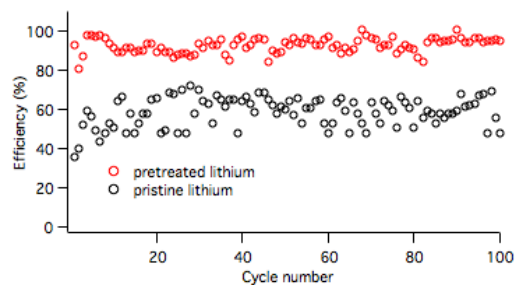


Figure S6.5 Lithium deposition efficiency of the Li/electrolyte/stainless steel cell with pristine lithium and pretreated lithium respectively in LiPS rich electrolyte. The cell is discharge for 30 min at a constant current density of 2 mA/cm^2 , then charge back to 0.5V at the same current density.

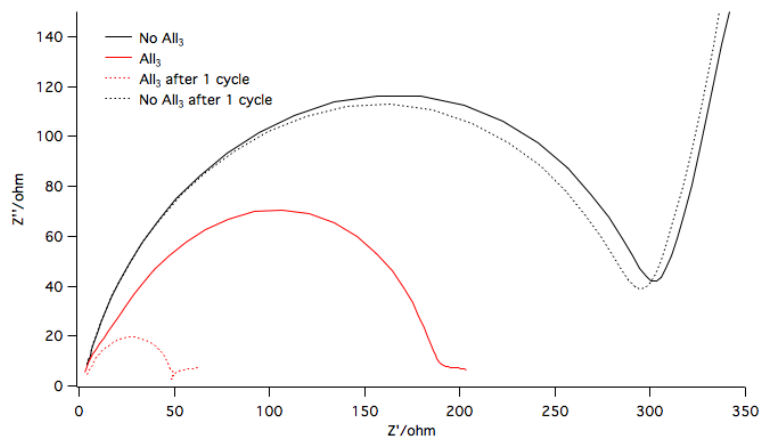


Figure S6.6 Impedance of the cell before and after treatment with AlI₃.

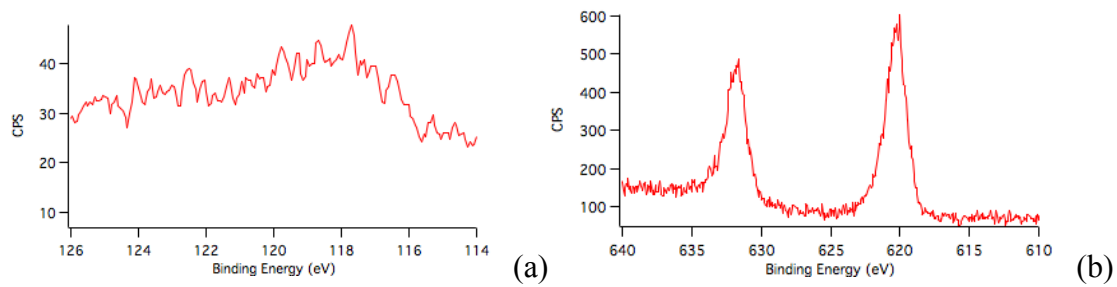
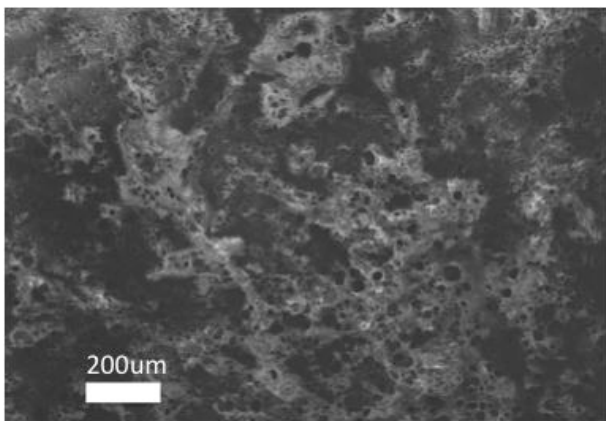
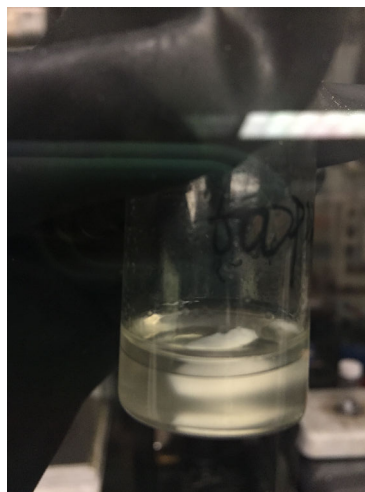


Figure S6.7 XPS of pretreated lithium metal after polarization test. a, Al 2s signal. b, I 3d signal.



(a)



(b)

Figure S6.8 Clues for the additional protection polymer film on lithium metal surface. a, SEM image of lithium metal after short circuit in the polarization test. b, DOL/DME electrolyte containing AlI_3 after resting for 2 weeks.

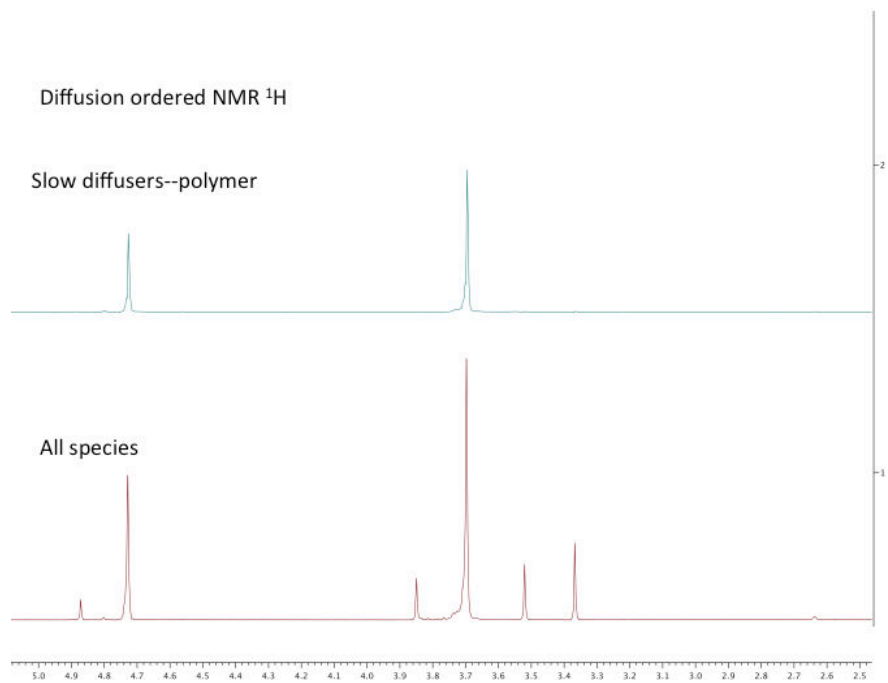


Figure S6.9 Diffusion ordered ^1H NMR of the gel.

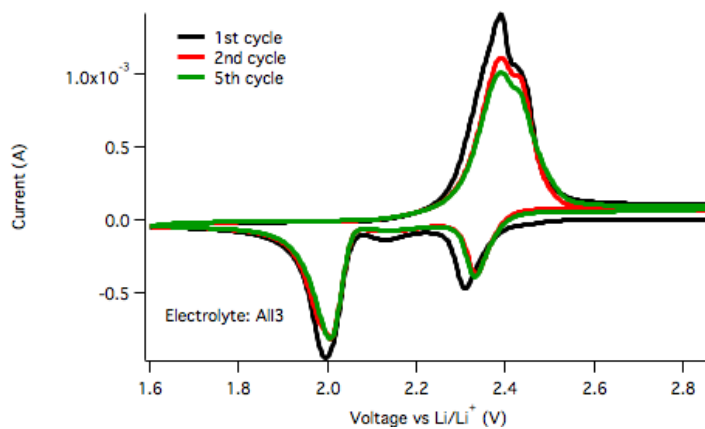


Figure S6.10 Cyclic Voltammetry of the Li-S battery applying the pretreated lithium as the anode.